Catchment coevolution and the geomorphic origins of variable source area hydrology

David Litwin[1], Gregory E. Tucker[2], Katherine R. Barnhart[3], and Ciaran J Harman[1]

[1]Johns Hopkins University
[2]University of Colorado Boulder
[3]U.S. Geological Survey

February 16, 2024

Abstract

Features of landscape morphology—including slope, curvature, and drainage dissection—are important controls on runoff generation in upland landscapes. Over long timescales, runoff plays an essential role in shaping these same features through surface erosion. This feedback between erosion and runoff generation suggests that modeling long-term landscape evolution together with dynamic runoff generation could provide insight into hydrological function. Here we examine the emergence of variable source area runoff generation in a new coupled hydro-geomorphic model that accounts for water balance partitioning between surface flow, subsurface flow, and evapotranspiration as landscapes evolve over millions of years. We derive a minimal set of dimensionless numbers that provide insight into how hydrologic and geomorphic parameters together affect landscapes. We find an inverse relationship between the dimensionless local relief and the fraction of the landscape that produces saturation excess overland flow, in agreement with the synthesis described in the "Dunne Diagram.' Furthermore, we find an inverse, nonlinear relationship between the Hillslope number, which describes topographic relief relative to aquifer thickness, and the proportion of the landscape that variably saturated. Certain parameter combinations produce features with wide valley bottom wetlands and nondendritic, diamond-shaped drainage networks, which cannot be produced by simple landscape evolution models alone. With these results, we demonstrate the power of coupled hydrogeomorphic models for generating new insights into hydrological processes, and also suggest that subsurface hydrology may be integral for modeling aspects of long-term landscape evolution.

Catchment coevolution and the geomorphic origins of variable source area hydrology

David G. Litwin[1], Gregory E. Tucker[2,3], Katherine R. Barnhart[4], Ciaran J. Harman[1,5]

[1]Department of Environmental Health and Engineering, Johns Hopkins University, Baltimore, MD, USA
[2]Cooperative Institute for Research in Environmental Sciences (CIRES), University of Colorado, Boulder, CO, USA
[3]Department of Geological Sciences, University of Colorado, Boulder, CO, USA
[4]U.S. Geological Survey, Geologic Hazards Science Center, Golden, CO, USA
[5]Department of Earth and Planetary Science, Johns Hopkins University, Baltimore, MD, USA

Key Points:

- A landscape evolution model with runoff from shallow groundwater was used to explore how hydrological function coevolves with topography.
- Landscapes evolve toward equilibrium where unchanneled uplands supply just enough water for persistence of lowland saturated areas.
- We found local relief decreases log-linearly with the fraction of runoff generated by saturation excess, in agreement with field studies.

Corresponding author: Ciaran J. Harman, charman1@jhu.edu

Abstract

Features of landscape morphology—including slope, curvature, and drainage dissection—are important controls on runoff generation in upland landscapes. Over long timescales, runoff plays an essential role in shaping these same features through surface erosion. This feedback between erosion and runoff generation suggests that modeling long-term landscape evolution together with dynamic runoff generation could provide insight into hydrological function. Here we examine the emergence of variable source area runoff generation in a new coupled hydro-geomorphic model that accounts for water balance partitioning between surface flow, subsurface flow, and evapotranspiration as landscapes evolve over millions of years. We derive a minimal set of dimensionless numbers that provide insight into how hydrologic and geomorphic parameters together affect landscapes. We find an inverse relationship between the dimensionless local relief and the fraction of the landscape that produces saturation excess overland flow, in agreement with the synthesis described in the "Dunne Diagram." Furthermore, we find an inverse, nonlinear relationship between the Hillslope number, which describes topographic relief relative to aquifer thickness, and the proportion of the landscape that variably saturated. Certain parameter combinations produce features wide valley bottom wetlands and nondendritic, diamond-shaped drainage networks, which cannot be produced by simple landscape evolution models alone. With these results, we demonstrate the power of coupled hydrogeomorphic models for generating new insights into hydrological processes, and also suggest that subsurface hydrology may be integral for modeling aspects of long-term landscape evolution.

Plain Language Summary

The topography of landscapes affects how much and where precipitation becomes runoff, while runoff itself plays a role in shaping topography over long times through erosion. Some landscapes may exist exist in an equilibrium state, where the landscape is ideally shaped to carry the amount of runoff produced. Understanding this equilibrium may provide insights into why landscapes have different hydrological styles; for example, some landscapes contribute runoff to streams primarily through the ground, whereas others develop saturated areas during storms that generate surface runoff when rain falls on them. Here we use a new model to simulate dynamic runoff as we expect it to occur in humid temperate environments while also using this runoff to evolve topography. The results show that landscapes that already have a tendency to produce variably saturated areas because they are poor at storing water or transmitting it laterally through the ground also evolve to have lower relief, which helps variably saturated areas to persist. The results highlight the role that landscape history plays in the hydrological processes observed today and can be used to better understand the role of subsurface hydrological processes in long-term landscape evolution.

1 Introduction

1.1 Motivation

Landscape geomorphology is inextricably connected to runoff generation. Topographic slope is often a strong predictor of hydraulic gradient (Haitjema & Mitchell-Bruker, 2005), whereas topographic curvature affects how water is concentrated or dispersed as it moves downslope (Lapides et al., 2020; Prancevic & Kirchner, 2019; Troch et al., 2003), all of which affects the likelihood of surface runoff. Subsurface porosity and permeability further affect these quantities, as they affect how effectively the subsurface can infiltrate water and transmit it laterally toward streams (Horton, 1933; O'Loughlin, 1981). At the same time, runoff can alter geomorphic properties of landscapes because it drives erosion and ultimately the incision of river channels, which then affect the morphology of adjacent hillslopes (Callahan et al., 2019; Dietrich et al., 2003; Roering et al., 2001).

Landscape evolution models (LEMs) have been essential tools for understanding topographic change over long timescales (e.g., reviews by Bishop, 2007; Chen et al., 2014; Pelletier, 2013; Tucker & Hancock, 2010; Valters, 2016; Willgoose, 2005) and thus are expected to be useful for understanding relationships between topography and runoff. However, landscape evolution simulations usually simplify hydrology to an extent that feedbacks between landscape evolution and subsurface flow dynamics cannot be examined. Recent studies have made progress in representing hydrologic processes more explicitly in LEMs, and show that drainage density scales linearly (Luijendijk, 2022) or nonlinearly (Litwin et al., 2021) with transmissivity when runoff is generated by saturation excess overland flow. Although these studies broke new ground by revealing how runoff generation affects topography, it is still unclear how this coevolution affects hydrological function. Understanding how landscape history affects current hydrological function has the potential to transform how we understand Earth's critical zone, and how we make hydrological predictions (Harman & Troch, 2014; Singha & Navarre-Sitchler, 2022; Troch et al., 2015).

Hydrological function describes the quantity, timing, and location of the storage and release of water from watersheds. Relationships between various stores and fluxes are used to describe a watershed's hydrological functioning. One of the most fundamental is the catchment water balance, which describes the long-term partitioning of water into storage, evapotranspiration, runoff, and deep recharge. On shorter timescales, storage-discharge relationships have been essential for understanding rainfall-runoff response and catchment recession (McMillan, 2020). The relationship between saturated area or active stream network length and discharge has illuminated geologic and topographic and climatic controls on runoff generation (Jensen et al., 2017; Latron & Gallart, 2007; Prancevic & Kirchner, 2019; Warix et al., 2021). Although these attributes of hydrological function are important in their own right (e.g., habitat extent and connectivity provided by the flowing stream network (Campbell Grant et al., 2007)), when taken together and compared across many sites, mappings can be developed that relate hydrological function to catchment attributes. These can improve hydrological predictions where historical datasets are short or not available (Wagener et al., 2007). Understanding how hydrological function coevolves with catchment attributes may provide a deeper understanding of these mappings, including why they exist at all.

1.2 Runoff generation and saturated areas

Dunne (1978) provided a succinct framework for understanding the relationship between climate, landscape morphology, and runoff generation mechanisms. In humid climates with minimal anthropogenic disturbance, thick soils in steep landscapes produce primarily subsurface variable source areas (Hewlett & Hibbert, 1967), where a saturated wedge may form in the subsurface near the toe of the hillslope and expand up the hillslope in response to recharge. In contrast, humid environments with shallow soils and more gentle topography tend to produce saturation excess overland flow (Dunne & Black, 1970), where subsurface lateral flow capacity is exceeded, producing saturated areas where groundwater may exfiltrate and become surface runoff along with precipitation on saturated areas. These relationships between topographic properties and runoff generation mechanisms were recently re-examined by Wu et al. (2021), who used a larger dataset than Dunne (1978) and identified characteristic features of different runoff generation mechanisms in rainfall-runoff relationships. While the inclusion of more diverse environmental settings required further subdivision of runoff generation mechanisms and controls, the fundamental relationships identified by Dunne (1978) still emerged.

However, research so far has not provided sufficient explanation for why certain combinations of topographic properties and runoff generation mechanisms appear (Li et al., 2014). This question is not particularly new. As distributed hydrological modeling of runoff generation became possible, Freeze (1980) noted:

> The simulations carried out in this study have placed the author in some awe of the delicate hydrologic balance on a hillslope. If one fixes the mean hydraulic conductivity of a hillslope, then there is only a very narrow range of topographic slopes that can lead to runoff generated by the Dunne mechanism. If one fixes the topographic slope of a hillslope, then there is only a very narrow range of hydraulic conductivities that will lead to a water table that is high enough to allow the Dunne mechanism to be operative in a given climatic regime. The fact that the Dunne mechanism is so common in nature in spite of these theoretical limitations on its occurrence infers a very close relationship between climate, hydraulic conductivity, and the development of geomorphic landforms.

What Freeze (1980) observed in simulations indicates that some sort of catchment coevolution (Troch et al., 2015) might be needed to explain a tendency toward saturation excess variable source area runoff generation (the "Dunne mechanism"). The literature exploring the evolution of climate–morphology–runoff generation relationships is minimal. Here our goal is to provide a broad picture of what kinds of landscapes and hydrological behavior emerge as we allow climatic, hydrologic, and geologic properties to vary, assuming that runoff generation is driven by saturation excess from shallow groundwater flow and subsurface stormflow. We provide a synthesis of some of our results in the context of relationships identified in field data, including those of Dunne (1978), which indicate that at least certain features of that relationship are emergent products of catchment coevolution.

1.3 Climate stochasticity in landscape evolution models

Precipitation variability has long been recognized as an important factor in landscape evolution. Ijjász-Vásquez et al. (1992) considered steady-state subsurface flow and an exponential distribution of rainfall depths, and showed that the statistical distribution of resulting erosion rates effectively smoothed hillslope-valley transitions. Tucker and Bras (1998) found similar smoothing of hillslope-valley transitions with a comparable model that used a steady state partitioning of flow between surface and subsurface for storm events drawn from exponential distributions of depth, duration, and interstorm duration. Similar approaches with stochastic precipitation but steady-state hydrological models are still widely in use (e.g., Barnhart et al., 2018). However, these models are limited in that antecedent conditions are not considered; the runoff and sediment transport rate during each event is independent from previous events.

Other studies have taken different approaches to capture some of the effects of memory and event sequence on runoff and erosion. Lague et al. (2005) examined the effects of discharge variability on channel long profile evolution by using a power law distribution of runoff rates, forgoing an explicit model of the processes that convert rainfall to runoff. Deal et al. (2018) further advanced understanding of how runoff distributions affect channel long profiles using the stochastic hydrological model developed by Botter et al. (2007) to generate runoff from a coupled, spatially lumped soil moisture and linear reservoir groundwater model. This approach accounts for the important effects of antecedent water storage and evapotranspiration on runoff generation, which ultimately affects fluvial erosion (Rossi et al., 2016). Because of these features, the model developed by Deal et al. (2018) shows promise for understanding how climate translates into erosion events and long-term evolution. However, models of channel long profile evolution cannot quantify spatially distributed hydrological features of interest, such as variably saturated areas. Moreover, it remains unclear exactly how the hydrological parameters (e.g., the reservoir coefficient, or reservoir size) needed for the model developed by Deal et al. (2018) are best linked to the evolving channel profile or surrounding hillslopes.

Although a few previous studies have used LEMs that resolve spatially distributed hydrological features, none have investigated the hydrological function that emerges at geomorphic dynamic equilibrium. Huang and Niemann (2006) used a coupled groundwater-LEM to examine how topographic evolution changed runoff generation at a well studied site, but evolved the landscape for far less time than needed to achieve dynamic equilibrium. Huang and Niemann (2008) investigated long-term evolution with a coupled groundwater-LEM, but examined the sensitivity of modeled topography to hydrologic parameters by prescribing changes onto the slope-area relationship rather than directly simulating the evolution to dynamic equilibrium, which makes evaluating the role of coevolution between runoff generation and topography challenging. Lastly, Zhang et al. (2016) presented a highly detailed coupled hydrological and landscape evolution model, but the model has only been used as a proof of concept.

1.4 Approach

Here, we focus on the coevolution of topography and runoff generated by groundwater return flow and precipitation on saturated areas. To do this, we use the streampower-diffusion LEM called DupuitLEM that was developed by Litwin et al. (2021), in which runoff produces the shear stress for detachment limited erosion, and topography sets the boundary conditions for the groundwater system. To capture time-varying runoff generation, we include stochastic storm generation and a simplified representation of vadose zone dynamics. We evolve the coupled model toward geomorphic dynamic equilibrium where the denudation rate is approximately equal to the uplift rate. At this point the hydrological function of the landscape is in some sense in equilibrium with topography–what exactly this equilibrium is and how it emerges are central to our results and discussion.

Hydrologic function of emergent landscapes likely depends on geomorphic, hydraulic, and climatic parameters in the model. However, this parameter space is large, and combinations of parameters do not necessarily result in unique model outputs. Dimensional analysis of the model allows us to approach both of these problems. We use a nondimensionalization approach to produce a minimal set of dimensionless groups that both uniquely determine model output and provide insight into the competing processes that affect evolved morphology and hydrologic function. We begin with the nondimensionalization developed by Litwin et al. (2021), and expand it to include the effects of the vadose zone and time-varying climatic forcing.

Still, this dimensionless parameter space is too large for a comprehensive investigation of all possibilities. Without a full investigation of the parameter space, we can still answer key questions about how hydrological function coevolves with topography. We do this by focusing on how dimensionless groups that express climate and subsurface hydraulics affect (1) topography and drainage dissection, (2) water balance and flux partitioning, (3) spatial patterns of hydrologic fluxes and saturation, and (4) temporal relationships between saturated area, discharge, and storage. Based on the results, we present a perceptual model of the emergence and persistence of variable source area hydrology and show that the relationships between geomorphology and runoff generation in humid landscapes that were identified by (Dunne, 1978) can be obtained through coevolution. Finally we discuss the potential for using landscape history to understand present hydrological function.

2 Model Description

2.1 Topographic evolution

The LEM used here considers the evolution of topographic elevation $z(x,y,t)$ by water erosion $E_f(x,y,t)$, erosion resulting from the divergence of hillslope regolith transport $E_h(x,y,t)$, and uplift or baselevel change U.

$$\frac{\partial z}{\partial t} = -E_f - E_h + U \tag{1}$$

Litwin et al. (2021) derived the water erosion term from excess shear stress, arriving at a form that is similar to the detachment-limited streampower law, but using the area per contour width a instead of upslope area A. Bonetti et al. (2018) define $a(x,y)$ as the scalar field satisfying $-\nabla \cdot \left(a \frac{\nabla z}{|\nabla z|} \right) = 1$, which is an elegant analytical definition of the concept usually defined as $a = A/v_0$ in the limit of small contour width v_0. The erosion law also scales linearly with the dimensionless discharge $Q^* = Q/(pA)$, where Q is the volumetric discharge and p is the mean precipitation rate, which we derived from the hydrological model as discussed below. The rate of water erosion is:

$$E_f = K\sqrt{v_0}Q^*\sqrt{a}|\nabla z| - E_0 \tag{2}$$

where K is the streampower erosion coefficient, and E_0 is a threshold below which no water erosion occurs. Although erosion thresholds can have important effects on morphology (e.g., Tucker, 2004), here we only present results for $E_0 = 0$, as we found the threshold to have little effect on the hydrological behavior of interest in this study.

The term E_h describes gravity-driven movement of sediment via processes such as frost heave, animal burrowing, and tree throw. A simple formulation for E_h begins by assuming that the sediment flux is proportional to the local slope gradient, $q_h \sim \nabla z$, and the resulting elevation change is the divergence of this flux, $E_h \sim \nabla^2 z$. This is the linear hillslope diffusion law, which was used in Litwin et al. (2021). This assumption produces unrealistically steep toe slopes ($|\nabla z| > 1$) as hillslopes become long. Landscapes with high relief and long hillslopes generally have a form better described by nonlinear sediment flux laws, where flux increases super-linearly with slope. Near ridges and when relief is low, the law produces near-parabolic topography (like the linear diffusion law), but as the slope gradient increases it produces increasingly planar hillslopes. This replicates a shift from short-range transport to longer-distance transport processes such as dry ravel and shallow mass failures (e.g., Doane et al., 2018; Gabet, 2003; Roering et al., 1999; Tucker & Bradley, 2010). Data compiled by Godard and Tucker (2021) showed that most documented field case studies of hillslope morphology, transport efficiency, and erosion rate fall within the nonlinear transport regime. We chose the hillslope transport model described by Ganti et al. (2012), which is a Taylor expansion of the critical slope model

$$q_h = \frac{D\nabla z}{1 - (|\nabla z|/S_c)^2} \tag{3}$$

used by Andrews and Bucknam (1987) and Roering et al. (1999), but is more computationally tractable for landscape evolution simulations. The rate of elevation change due to hillslope erosion is

$$E_h = \nabla \cdot q_h = D\nabla \cdot \left(\nabla z \left(1 + \left(\frac{|\nabla z|}{S_c} \right)^2 \right) \right) \tag{4}$$

where D is the transport coefficient and S_c is a critical slope. This expression represents the first two terms of the Taylor expansion, which Ganti et al. (2012) showed to be a close approximation of the original partial differential equation.

Combining the water- and gravity-driven erosion terms with a constant rate of base-level change U, we arrive at the governing equations of the LEM:

$$\frac{\partial z}{\partial t} = -K\sqrt{v_0}\langle Q^* \rangle \sqrt{a}|\nabla z| + D\nabla \cdot \left(\nabla z \left(1 + (|\nabla z|/S_c)^2\right)\right) + U \tag{5}$$

$$-\nabla \cdot \left(a \frac{\nabla z}{|\nabla z|}\right) = 1 \tag{6}$$

where the angled brackets $\langle \cdot \rangle$ indicate the time-averaged value of the quantity.

2.2 Subsurface model

As in Litwin et al. (2021), we consider only a homogeneous, surface-parallel layer of permeable material with thickness b above impermeable bedrock. We will refer to this as the 'permeable thickness' as we do not distinguish between mobile regolith and weathered or fractured bedrock. Although deeper groundwater flow can be important for runoff generation, here the permeable thickness sets the lower boundary for groundwater circulation. We will sometimes refer to 'regolith' when discussing hillslope sediment transport, although ultimately the geomorphic model is agnostic to the composition of the subsurface. That is, we assume there is always enough regolith to meet the slope-based hillslope flux law. Lastly, the term 'soil' is used when referencing or drawing comparison with field studies that use this term, in which case the analogous term in our model is permeable thickness.

How exactly the subsurface of real landscapes evolves to keep pace with surface evolution is an active subject of research that so far has no consensus (Riebe et al., 2017). Surface-parallel permeability structure is sometimes (but not always) observed in the field St. Clair et al. (2015), and also emerges at geomorphic steady state with the widely used exponential production model (e.g., Rosenbloom & Anderson, 1994; Tucker & Slingerland, 1997). Fixing the permeable thickness rather than tracking its evolution does have limitations, as discussed in Section 6.4, but ultimately we decided to keep the subsurface representation simple to focus on the dynamics of topographic and hydrologic evolution.

2.3 Hydroclimatological model

Given the long timescales of landscape evolution relative to runoff generation, it was necessary to make compromises between process representation and computational efficiency. Our goal was to develop a minimally complex model that captured the emergence of catchment and hillslope scale hydrological function (sensu Wagener et al., 2007) including water balance partitioning, and the presence of surface and subsurface variable source areas. We therefore aimed to construct a model that incorporated the following elements:

- rainfall, and therefore recharge, varies in time,
- rainfall is partitioned between quickflow and storage,
- storage is partitioned between ET and baseflow,
- ET is limited by energy in humid climates, and by water availability in dry climates.

To address the first element, we generated stochastic storm depth d_s, duration t_r, and interstorm duration t_b using exponential distributions, following Eagleson (1978), and many papers in the hydrology (e.g., Botter et al., 2007; Rodriguez-Iturbe et al., 1999)) and landscape evolution literature (e.g., Barnhart et al., 2018; Tucker & Bras, 2000)). Previously we introduced the mean precipitation rate, p, which is related to the above parameters as $p = \langle d_s \rangle / (\langle t_r \rangle + \langle t_b \rangle)$. The distributions for storm depth, duration, and interstorm duration are:

$$f(d_s) = \frac{1}{\langle d_s \rangle} \exp\left(-\frac{d_s}{\langle d_s \rangle} \right) \tag{7}$$
$$f(t_r) = \frac{1}{\langle t_r \rangle} \exp\left(-\frac{t_r}{\langle t_r \rangle} \right) \tag{8}$$
$$f(t_b) = \frac{1}{\langle t_b \rangle} \exp\left(-\frac{t_b}{\langle t_b \rangle} \right). \tag{9}$$
$$\tag{10}$$

To address elements 2 and 3, we needed to account for storage in the unsaturated zone as well as the saturated zone. A thorough treatment of coupled saturated-unsaturated zone dynamics would be computationally prohibitive for landscape evolution simulations. We opted instead for a one-way coupling between a simple unsaturated zone model and the Dupuit-Forcheimer groundwater model, which is capable of capturing important features.

Schenk (2008) presented a simple model (called here the Schenk model) for vadose zone dynamics in a 1-dimensional profile that serves our purpose well. The model is based on the assumption that plants extract water from the shallowest depth where water is available, and use all available water at that depth before extracting water from deeper in the profile. Conversely, precipitation fills available storage at the ground surface first, and displaces water already present deeper into the profile. Schenk (2008) showed that the distribution of depths from which water is extracted in this model mimics the plant rooting depth distributions in a wide range of climates. This is useful to our study because the depths of root water uptake emerge as a result of the climate and subsurface hydraulic properties selected rather than requiring an additional parameter.

We took a spatially-integrated approach to the unsaturated zone state, modeling unsaturated zone storage with the Schenk model, from which we derived spatially distributed estimates of groundwater recharge based on the water table depth. The Schenk model can be written in cumulative form using the coordinate d, depth below the ground surface. The model tracks the volume (per unit area) of storage S_d above depth d, which evolves in time according to:

$$S_d(d, t + \Delta t) - S_d(d, t) = \min\left(dn_a - S_d(d, t), i(t)\Delta t\right) - \min\left(S_d(d, t), pet(t)\Delta t\right) \tag{11}$$

where t is the current time, Δt is the timestep, n_a is the plant-available water content (equal to the field capacity minus the water content below which plants will prefer to use water from deeper depths), $i(t)$ is the storm intensity (equal to $d_s/\Delta t$ during storms, and zero otherwise), and $pet(t)$ is the potential evapotranspiration (ET) rate (equal to a constant rate pet during interstorms and zero otherwise). Equation (11) states that the change in vadose water stored above depth d over the time interval Δt is the lesser of the available vadose storage above d and the depth of rainfall during the interval, minus the lesser of the water in vadose storage above d and the evapotranspiration during the interval. We assumed that the recharge R_d received by a water table at depth d is the amount of water that has infiltrated below d in the vadose profile:

$$R_d(d, t) = i(t)\Delta t - \min\left(dn_a - S_d(d, t), i(t)\Delta t\right) \tag{12}$$

from which we arrive at the recharge rate:

$$r(x, y, t) = \frac{R_d(b - h(x, y, t), t)}{\Delta t} \tag{13}$$

where the depth to the water table is $b - h(x, y, t)$, the permeable thickness minus the aquifer thickness. We have set the maximum profile depth equal to the permeable thickness b, such that $d \leq b$, which ensured continuity between saturated and unsaturated flow models. Note that the recharge rate in Equation (13) is equal to the precipitation rate i when the water table is at the surface ($b-h=0$). The groundwater model discussed in Section 2.4 then determines how this recharge will be partitioned between overland flow and saturated subsurface flow. A full sample calculation of the Schenk model is shown in Supplemental Figure S2.

The Schenk model was run such that each timestep was either an entire storm or an entire interstorm period. Any recharge generated was assumed to arrive at the groundwater table at a steady rate over the storm period. During interstorm periods, the recharge rate is assumed to be zero (even if the water table has risen farther into the unsaturated zone), and the actual evapotranspiration will always equal the potential evapotranspiration rate when water in vadose storage is available. We calculate total actual evapotranspiration by subtracting the total recharge from the total precipitation, assuming all precipitation that did not become recharge to the saturated zone was transpired. We explored the possibility of allowing for root water uptake from the saturated zone; however, we found that conservation of mass would only be possible if the unsaturated zone state was tracked uniquely at each location where we track water table elevation, defeating the purpose of choosing this model for its computational efficiency. In tests we found saturated zone root water uptake would be a relatively small component of the water balance in much of the parameter space (although we cannot rule out its importance in some edge cases). We leave further exploration of this for future work.

2.4 Groundwater flow and runoff generation

Runoff is generated by exfiltrating subsurface lateral flow and from precipitation (i.e., recharge from the unsaturated zone model) on saturated areas. We use a quasi 3-dimensional shallow unconfined aquifer model based on the Dupuit-Forcheimer approximations (Childs, 1971) for groundwater flow above a sloping impermeable boundary. We solve for the (saturated) aquifer thickness $h(x,y,t)$ based upon the lateral groundwater flux $q(x,y,t)$, local runoff production $q_s(x,y,t)$, and recharge $r(x,y,t)$. Surface water discharge $Q(x,y,t)$ is calculated by instantaneously routing q_s over the area upslope from a given location. The governing equations for the hydrological model are:

$$\frac{\partial h}{\partial t} = \frac{1}{n_e}\Big(r - \nabla \cdot q - q_s\Big) \tag{14}$$

$$q = -h\cos\theta k_s\big(\nabla z + \nabla h\big)\cos\theta \tag{15}$$

$$q_s = \mathcal{G}\Big(\frac{h}{b}\Big)\mathcal{R}\Big(r - \nabla \cdot q\Big) \tag{16}$$

$$Q = \int_A q_s dA \tag{17}$$

where n_e is the drainable porosity, which we assume to have a constant value, k_s is the saturated hydraulic conductivity, and $\theta(x,y,t)$ is the slope of the aquifer base. The regularization function $\mathcal{G}(\cdot)$ is equal to zero when the argument is less than 1, and approaches 1 as the argument approaches 1. In this case the argument h/b represents the portion of the total permeable thickness b that is occupied by the aquifer with thickness h. The ramp function $\mathcal{R}(\cdot)$ is zero when the argument is less than zero and is equal to the argument when it is greater than zero. Thus, Equation (16) says that runoff will occur when the ground is saturated to near the surface and the recharge exceeds the divergence of the groundwater flux.

In our analysis, we further divide discharge into a fast-responding component (quickflow), and a slow-responding component (baseflow). Discharge during interstorm periods is defined as entirely baseflow, whereas baseflow during storm events is estimated by linear interpolation between the pre-storm-event discharge and the post-storm-event discharge. This approach works for our model because all runoff generated during storm events is instantaneously routed to the outlet (Equation 17), leaving only the slowly varying exfiltration to leave as runoff during interstorm periods; see Figure S3 for an example. Quickflow, which is nonzero only during storm events, is then some combination of exfiltration and precipitation on saturated areas. Although the regularization functions in Equation (16) make it difficult to isolate their respective contributions, precipitation on saturated areas is usually the dominant contribution to quickflow as the model lacks mechanisms that would rapidly increase exfiltration during storm events.

3 Model implementation

3.1 Modeling platform

The governing equations were solved on a 125×125 square raster grid. The grid cell size is best considered within the framework of the nondimensionalization we use, which will be discussed in Section 4. The top, right, and left boundaries are zero-flux boundaries, while the bottom boundary is a fixed value (Dirichlet) boundary, where the land surface and water table elevation are coincident. The initial condition is a near flat, roughened surface with zero elevation above baselevel. The domain can be considered in a moving reference frame, where the bottom boundary is an adjacent lateral stream (albeit with zero slope) incising at a rate U. The vadose profile was discretized such that each depth increment is equal in size and has a maximum unsaturated storage $\leq$ 1% of the mean storm depth.

The model is implemented as a Python package called DupuitLEM that is built on process components from the Earth surface modeling platform Landlab (Barnhart et al., 2020; Hobley et al., 2017). The LEM is solved using existing process components in a loosely coupled scheme, where diffusion is solved with a forward Euler finite volume method and the streampower erosion module is solved with an implicit method based on Braun and Willett (2013). The groundwater model (Litwin et al., 2020) is solved with an approach that combines explicit calculation of lateral groundwater flow and an analytical solution for groundwater rise and exfiltration based on the regularization presented by Marçais et al. (2017).

3.2 Upscaling discharge to geomorphic time

In any computationally feasible model of landscape evolution that incorporates hydrological processes, some scaling is needed between the timescales of the two models. We simply cannot simulate hydrological processes for millions of years. This temporal scaling has two primary approaches: online updating and offline updating. An online updating approach matches one hydrological time step to one geomorphic time step, and simply scales the effect of each event to represent some longer duration of time. An offline updating approach simulates hydrology on a fixed landscape over some duration from which meaningful average quantities can be derived. The average quantities, including discharge, are then used to evolve the landscape over some longer duration. Although both approaches have benefits and drawbacks, here we used an offline updating approach, as it allows for greater continuity of hydrological state. In an online updating approach, the model may erode substantial regolith and the water within the regolith in each time step, making it difficult to have a meaningful water balance. Here we ran the hydrological model for 25 storms before using the results to evolve the landscape forward in time. The scaling factor between hydrologic and geomorphic time varies by the simulation from 250 to 64000, depending on the duration of the mean storm-interstorm period.

In this paper we consider time-varying precipitation and recharge, and as a result Q^* will also vary substantially on hydrological timescales. As stated previously, $\langle Q^* \rangle$ is the temporal average of Q^* used to obtain an effective value that can be applied on landscape evolution timescales. Because Equation (5) is linear in $\langle Q^* \rangle$, this can simply be the time-weighted mean discharge. This would not be the case when an incision threshold is present, or when the exponents in the incision model are changed.

4 Scaling analysis

Dimensional analysis is a powerful tool for examining the behavior of models, allowing us to identify groups of parameters that affect the solutions to the governing equations in related ways. Litwin et al. (2021) nondimensionalized a simpler version of the model presented here with linear hillslope diffusion and uniform recharge directly to the water table. The nondimensionalization applied the concept of symmetry groups (Barenblatt, 1996), minimal sets of parameters that, when scaled by a constant factor, leave the governing equations unchanged. We nondimensionalized the governing equations systematically by carefully choosing the constant factors and introducing definitions of equivalent dimensionless variables.

The approach used characteristic scales derived from the model parameters to isolate dimensions of the model. These are listed in Table 1. We applied the same symmetry group approach presented in Litwin et al. (2021) to the continuum equations of the model used here to determine the following dimensionless governing equations:

$$\frac{\partial z'}{\partial t'} = -Q^* \sqrt{a'} |\nabla' z'| + \nabla' \cdot \left(\nabla' z' \left(1 + \left(\frac{\nabla' z'}{S_c/\alpha} \right)^2 \right) \right) + 1 \tag{18}$$

$$-\nabla' \cdot \left(a' \frac{\nabla' z'}{|\nabla' z'|} \right) = 1 \tag{19}$$

$$\delta \frac{\partial h'}{\partial t} = r' - \nabla' \cdot q' - q'_s \tag{20}$$

$$q' = -h' \cos^2 \left(\arctan |\alpha \nabla' z'| \right) \left(\nabla' h'/\beta + \nabla' z' \right) \tag{21}$$

$$q'_s = \mathcal{G} \left(\frac{h'}{\gamma} \right) \mathcal{R} \left(r' - \nabla' \cdot q' \right) \tag{22}$$

$$Q^* = \frac{1}{A'} \int_{A'} q'_s dA' \tag{23}$$

where prime indicates a dimensionless equivalent (defined in Section 8). Five dimensionless groups, plus the critical gradient S_c, remain as parameters. These are listed in Table 2.

Symbol	Name	Definition
h_g	Characteristic geomorphic height scale	$\left(\frac{DU^3}{v_0^2 K^4}\right)^{1/3}$
ℓ_g	Characteristic geomorphic length scale	$\left(\frac{D^2}{v_0 K^2}\right)^{1/3}$
t_g	Characteristic geomorphic time scale	$\left(\frac{D}{v_0^2 K^4}\right)^{1/3}$
h_a	Characteristic aquifer thickness	$\frac{p\ell_g}{k_s h_g/\ell_g}$
t_d	Characteristic drainage timescale	$\frac{\ell_g n_e}{k_s h_g/\ell_g}$
l	Domain length	–

Table 1. Characteristic scales that were derived to isolate the dimensions (length, height, and time) of the model.

Symbol	Name	Characteristic Scale Definition	Parameter Definition
α	Characteristic gradient	$\frac{h_g}{\ell_g}$	$\frac{U}{v_0^{1/3} D^{1/3} K^{2/3}}$
β	Aquifer relief scale	$\frac{h_g}{h_a} = \frac{k_s h_g^2}{p \ell_g^2}$	$\frac{k_s U^2}{p\, v_0^{2/3} D^{2/3} K^{4/3}}$
γ	Drainage capacity	$\frac{b}{h_a} = \frac{b k_s h_g / \ell_g}{p \ell_g}$	$\frac{b k_s U}{pD}$
δ	Timescale factor	$\frac{t_d}{t_g}$	$\frac{n_e\, v_0^{2/3} D^{2/3} K^{4/3}}{k_s U}$
λ	Domain scale factor	$\frac{l}{\ell_g}$	$\frac{l v_0^{1/3} K^{2/3}}{D^{2/3}}$

Table 2. The dimensionless groups (plus S_c) that appear in the dimensionless equations (18–23).

Of the dimensionless groups, we expect β and γ to be the most important controls on emergent hydrological behavior, as they affect critical aspects of hydrological function. The aquifer relief scale β describes the geomorphic height scale relative to aquifer thickness, which was called the hillslope number in Litwin et al. (2021) because its form is analogous to Brutsaert (2005, their Eq. 10.139) used to understand shallow groundwater dynamics. However, we found that it was harder to interpret β as a hillslope number in this study due to the combination of evolving landscape form, time-variable recharge and evapotranspiration. We will return to the discussion of the hillslope number and the role of β in Section 6.6. The drainage capacity γ describes the permeable thickness relative to characteristic aquifer thickness, or equivalently the ratio of a characteristic Darcy flux to precipitation on a hillslope with length ℓ_g. The characteristic gradient α is the ratio of geomorphic height and length scales, which we will keep fixed in this paper, but was explored in Litwin et al. (2021). The timescale factor δ is the ratio of hydrologic to geomorphic timescales, which we expect to be small in all cases given the large difference between hydrologic and geomorphic process rates. Lastly, λ is the domain scale factor, where l is the domain side length. λ is large in all cases considered here, and is not expected to affect our results (Anand et al., 2022; Bonetti et al., 2020; Litwin et al., 2022).

The stochastic forcing introduced three additional parameters: mean storm duration $\langle t_r \rangle$, mean interstorm duration $\langle t_b \rangle$, and mean storm depth $\langle d_s \rangle$, while the inclusion of vadose zone dynamics and evapotranspiration introduced two additional parameters: evapotranspiration rate *pet* and plant-available water content n_a. We found that four dimensionless groups were needed to represent the additional parameters, shown in Table 3. These groups were chosen to provide intuition into competing processes. The dimensionless forms of the Schenk model are given in Appendix B, Equations (A15) and (A21).

Although all of the dimensionless groups in Table 3 may be important for hydrological function and emergent landscapes, we focused on variation in σ and aridity index Ai. The water storage index σ describes the competition between the maximum possible saturated zone storage and mean storm depth, where smaller values indicate that local saturated zone storage is more easily exceeded by storms. Ai is the duration-corrected rate of potential evapotranspiration relative to rainfall, which has a critical effect on how much water becomes recharge. The precipitation steadiness index ρ is the proportion of time in which rainfall is occurring, which in the limit of $\rho \to 1$ is the steady case considered by Litwin et al. (2021). Lastly, the moisture content index ϕ describes the vadose zone plant-available water content relative to the saturated zone drainable porosity.

Symbol	Name	Parameter Definition
σ	Water storage index	$\frac{bn_e}{p(\langle t_r \rangle + \langle t_b \rangle)}$
Ai	Aridity index	$\frac{pet\langle t_b \rangle}{p(\langle t_r \rangle + \langle t_b \rangle)}$
ρ	Precipitation steadiness index	$\frac{\langle t_r \rangle}{\langle t_r \rangle + \langle t_b \rangle}$
ϕ	Moisture content index	n_a/n_e

Table 3. The additional dimensionless groups needed to describe the climatic and vadose models.

5 Results

We conducted simulations to explore the effects of subsurface properties and climate on morphology and runoff generation by varying the dimensionless groups identified in Section 4. Although the simulations do not cover the entire parameter space, they are sufficient to show a range of hydrologic behaviors that emerge from the coupled model. The results are presented in three sets of simulations. First, we varied σ and Ai, holding other dimensionless groups constant (except the timescale factor δ, although the effects of this variation are assumed to be negligible). Second, we ran the same combination of σ and Ai but decreased β by a factor of 10 to examine a case where aquifers are thicker relative to relief. Finally, we fixed Ai to a humid value of 0.5 and varied γ and σ to explore the interaction of storage and drainage in the subsurface.

All our results focus on the climatic end-member where storm durations are short relative to the time between storms ($\rho = 0.03$). We used the average value of α investigated by Litwin et al. (2021) ($\alpha = 0.15$), the domain scale factor was fixed at $\lambda = 250$, and others were chosen to be physically reasonable, including a critical slope $S_c = 0.5$ and moisture content index $\phi = 1.5$.

We ran simulations for $2000t_g$, by which time, most simulations had reached an equilibrium where mean relief was no longer increasing (Supplemental Figure S1). Cases not reaching equilibrium tend to be arid, and have poorly developed drainage networks. Once the landscape evolution simulation had completed, we ran the hydrological component of the model (without changing the topography) for $2000(\langle tr \rangle + \langle t_b \rangle)$ using the final water table as an initial condition to collect more detailed information on hydrological state and fluxes. Spatially distributed output (saturated area, recharge) were recorded at the storm-interstorm timescale, while spatially-lumped data (water balance components, total saturated area, total storage) were recorded at intervals corresponding to 1% of maximum timestep for groundwater model stability (Litwin et al., 2020).

5.1 Effects of climate on topography

Before examining the hydrological function of the evolved landscapes, we will begin by examining their topography. Aridity index Ai and water storage index σ play important roles in determining the partitioning of precipitation into evapotranspiration, surface flow, and subsurface flow, which ultimately affects the amount of water available to shape topography through erosion. The hillshades in Figure 1A show the development of characteristic ridge-valley topography when Ai < 1, where drainage dissection decreases with increasing aridity. When Ai ≥ 1 drainage networks are minimal or nonexistent (given the domain size, boundary conditions and other parameters used). Relief also increases with increasing aridity, as relief increases with decreasing drainage dissection while α and S_c are held constant.

The water storage capacity σ modulates the relationship between topography and aridity. When σ is small, the subsurface has a small capacity to store water relative to the average storm depth, and consequently surface runoff is produced more frequently across more of the landscape, increasing dissection and lowering relief. In the results presented, we decreased σ by reducing rainfall frequency and increasing intensity while keeping water storage capacity constant. Figure 1 shows that drainage networks can form under higher aridity climates when σ is small, as large infrequent storm events have more potential to generate surface water runoff than if the same annual precipitation were spread amongst more frequent storms.

Cross sections through the subsurface (Figure 1B–E) show differences in relief and mean water table position between selected model runs. Humid landscapes with small storage indices have the least relief and maintain water tables close to the surface (Figure 1D). Arid landscapes with small σ have the highest relief, and water tables are near the impermeable bedrock except near channels. When σ is large (large permeable thickness and/or many small storms) aridity has a highly non-linear effect on topography, with effectively no stream dissection for cases where Ai>1.

5.2 Water balance partitioning

We examined the water balance at two levels, first partitioning of precipitation into actual evapotranspiration (AET) and total runoff through the lens of the Budyko framework (Budyko, 1974), and then used the L'vovich framework (L'vovich, 1979) to understand the quickflow-baseflow partitioning. The framework was applied to all three sets of model runs (varying Ai and σ, varying Ai and σ with low β, and varying σ and γ), which have corresponding topography in Figures 1, S5, and S6. All results show total fluxes into and out of the domain averaged over $2000(\langle tr\rangle + \langle t_b\rangle)$.

The Budyko plots in Figure 2A,D, show how precipitation is partitioned to evapotranspiration (rather than discharge) as a function of aridity, and the constraints that energy and mass balance place on this partitioning (dashed lines) for high and low β cases. In energy-limited environments, the maximum ratio $\langle AET\rangle/\langle P\rangle$ is $\langle PET\rangle/\langle P\rangle \approx$ Ai, whereas in water-limited environments, the maximum ratio is one. Model results in Figure 2A closely follow respective energy and water limitations at each aridity, indicating actual ET is occurring at close to the potential ET rate. In contrast, Figure 2D shows that when the aquifer relief scale β and water storage index σ are small (i.e., thinner aquifers relative to relief and smaller storage capacity relative to storm depth) and the climate is humid, substantially less precipitation becomes evapotranspiration (and more becomes discharge) than in the previous case. Figure 2G shows how this partitioning is affected by drainage capacity γ for a constant aridity Ai $= 0.5$, where poorly drained landscapes (low γ) appear to produce less actual ET relative to precipitation, although the effect is smaller than that of the aridity index Ai. In the particular stochastic simulations we ran, $\langle PET\rangle/\langle P\rangle >$ Ai, so we place the horizontal line at $\langle PET\rangle/\langle P\rangle$ to show that actual ET still does not exceed potential ET.

The L'Vovich framework allows us to more deeply understand the catchment water balance by decomposing discharge into quickflow Q_f that leaves the watershed rapidly during storms, and baseflow Q_b that is released more slowly. We examine (1) how precipitation is partitioned into quickflow and storage, and then (2) how storage is partitioned into ET and baseflow.

We first consider the fraction of precipitation that becomes quickflow, shown in Figures 2B,E,H. These show that quickflow fraction is sensitive to all dimensionless groups considered (γ, β, σ, and Ai). In Figure 2B, the quickflow fraction decreases rapidly with increasing aridity, until almost no quickflow is generated when Ai ≥ 1. In contrast, Figure 2E shows that when the aquifer relief scale β is small, quickflow is more sensitive to water storage index σ, and for $\sigma = 8$ the quickflow is greater that 50% even when Ai $=$

1. Quickflow fraction declines rapidly with increasing γ (Figure 2H) with a nonlinear dependence that is similar to the effect of aridity shown in Figure 2B.

Second, we can consider how the remaining precipitation (that has become storage rather than leaving as quickflow) is partitioned into evapotranspiration and baseflow (Figure 2C,F,I). In Figure 2C, we see that the baseflow fraction declines linearly with aridity in humid climates, and is minimal for Ai>1. This behavior is insensitive to the water storage index σ except in the smallest case. This is also true when the aquifer relief index β is small (Figure 2F), provided σ is large. However, when σ is small and the climate is humid, partitioning to baseflow is less sensitive to aridity, similar to the sensitivity seen in Figures 2D and E. Although quickflow fraction decreases with γ and aridity (Figures 2B, H), baseflow fraction generally increases with γ Figure 2I), the opposite of the pattern observed in baseflow fraction with aridity (Figure 2C). The baseflow fraction increases with γ until it levels out at a constant value as actual ET approaches potential ET (Figure 2G).

5.3 Spatial structure of recharge and saturated areas

The location and extent of saturated areas vary in time and space responding to changing recharge, water storage, and topographic states. Here we define recharge the same way it has been defined in previous sections, given by Equations (12) and (13). All water that is delivered to the saturated zone is defined as recharge, including when the water table is at the land surface, in which case the groundwater model determines how much will become runoff. As a consequence of the dependence of recharge on depth to water table (Equation 12), there are systematic variations in recharge rate with landscape position. Figure 3 shows the mean recharge rate $\langle r \rangle$ relative to the mean precipitation rate p in the same modeled cases shown previously in Figure 1. Lighter colors in Figure 3 highlight valleys and regions of convergent topography, where the water table tends to be close to the surface. Contrasts in recharge rates across different landscape positions increase with aridity until Ai $= 1$, at which point the water table is deep and the unsaturated zone tends to remain dry enough to hold precipitation without generating recharge (hidden cases in Figure 3 have no recharge). The relative recharge is also sensitive to σ, as large storms relative to permeable thickness (small σ) allow vadose water to reach the water table more frequently than when σ is large.

In order to examine spatial and temporal patterns of saturated area, we defined a metric of saturation occurrence and classified the landscape into zones that are wet, variably saturated, or dry. We define surface saturation based upon where the water table is within $0.025h_g$ of the ground surface. This metric approximates the "squishy boots" test used to identify variable source areas (e.g., Dunne et al., 1975). Areas that are saturated at the end of more than 95% of storms and interstorms are classified as wet, whereas locations that are saturated after less than 5% of storms and interstorms are classified as dry, and variably saturated areas are all others not in either of the previous classes (for our purposes, the classification is relatively insensitive to the choice of threshold values; for details, see Figure S4).

Results in Figure 4 show that the model produces widespread variably saturated areas organized around the interface between the channel network and adjacent hillslopes. In humid landscapes where the water storage index σ is small, channel networks are permanently saturated, and hillslopes can become saturated all the way to ridges at least occasionally (frequency > 0.05), when storm depths approach or exceed local saturated zone storage capacity. With increasing σ, variable source areas retreat to localized zones in channel heads and areas of topographic convergence. With increasing aridity, the water table tends to interact with the surface less frequently, leading to intermittent channel networks when Ai ≥ 1.

The transition to intermittent saturation in valley bottoms is also affected by the drainage capacity γ, due to its influence on the partitioning of water between surface and subsurface flow (Figure S9). When γ is large and σ is small, storms are large relative to storage, but subsurface drainage is efficient. Consequently, ridges remain dry, but saturation in valley bottoms is more variable than cases with lower γ or higher σ (see Figure S9, simulation 4).

Of note, discontinuous wet sections of the channel network emerge from the model without any introduced heterogeneity or spatial variation in permeable thickness. These can be seen for example in Figure 4 subplots 3, 4, 10, and 11, which have large β, intermediate Ai, and small σ. They also appear when γ is large (Figure S9), but are largely absent when β is smaller (Figure 5). These patterns are driven by differences in the local convergence and downslope conveyance capacity associated with topographic curvature and slope. These patterns are indicative of a discontinuous stream channel with both perennial and ephemeral reaches. It should be noted, however, that our saturation metric describes only the proximity of the water table to the surface, and does not include the presence of water routed from upslope, which in our model is not allowed to infiltrate once it has become surface runoff. Nevertheless, the emergence of this discontinuous network of saturated areas indicates that the morphology of the landscape, rather than just variability in subsurface properties, may provide a structural control on heterogeneous patterns of surface flow in valley bottoms. This feature is likely to persist in a model that allows re-infiltration, although instead of variably saturated valley bottoms, some areas of the parameter space may instead produce reaches that gain and lose water, again as a function of adjacent landscape morphology.

Other unusual features emerge as the aquifer relief index β becomes small, in which case the relief of the water table is similar to that of the topography. First, we observe that particular combinations of parameters produce drainage networks that are close to non-dendritic (Figure 5). This is highly unusual in LEMs, particularly those with single-direction flow routing and fluvial incision like this one. We say 'close to' non-dendritic because subtle drainage divides do exist such that surface flow is only routed in one direction at any particular topographic state – i.e., saddle-points. However, variable or even persistent saturation extends all the way up to these saddle-point divides, and flow directions near them may change frequently with evolving topography. Second, some model results show the presence of persistently saturated valley bottoms with widths greater than one pixel (e.g., Figure 5 subplots 10, 11, 17, 23, and 28). This is also uncharacteristic of the type of LEM formulation used here, which will generally incise valleys only one grid cell wide. This illustrates that erosion by runoff on saturated areas near the toes of hillslopes can help account for the formation of valleys that are substantially wider than the channels they contain. LEMs have generally only achieved valleys wider than one pixel by explicitly representing valley widening by lateral channel migration (Langston & Tucker, 2018). These permanent lowland wetland features and non-dendritic drainage networks are evidence of the strong influence that the aquifer structure can exert on surface drainage organization, even in a relatively simple model.

5.4 Co-variant dynamics of spatially-averaged saturation, storage, and discharge

The relationship between saturated area and baseflow discharge is a useful indicator of the relationship between landscape morphology, subsurface properties, and runoff generation (Latron & Gallart, 2007). We chose to examine baseflow rather than total flow because the total flow generated from a storm event for a given antecedent saturated area will be dependent on the storm intensity, whereas exfiltration-driven baseflow should vary more systematically with aquifer properties and topography.

Figure 6 shows the dimensionless baseflow discharge $Q_b^* = Q_b/pA_{tot}$ versus the dimensionless saturated area $A_{sat}^* = A_{sat}/A_{tot}$, where Q_b is the total baseflow discharge for the model domain, A_{sat} is the total saturated area, and A_{tot} is the total domain area. Saturated areas are calculated with the same criterion as in the spatially distributed figures. For reference, light gray points were added to indicate the total dimensionless discharge ($Q^* = Q_b^* + Q_f^*$). Baseflow points are colored by the dimensionless saturated storage $S^* = S/(bn_eA_{tot})$ to show relationships with saturated area and baseflow.

As expected from the spatial patterns of saturation in Figure 4, the range of the dimensionless saturated area decreases with increasing σ. When σ is large, the extent of saturated areas is fixed at approximately 10% of the watershed area in the most humid case, and decreases with increasing aridity. When σ is small, increasing aridity does not prevent the landscape from reaching near full saturation ($A_{sat}^* = 1$), but does lower the minimum saturated area, increasing the range of saturated area observed. Model runs with the same aridity tend to have similar minimum saturated extent, but with decreasing σ, the maximum saturated area generally increases.

Despite differences in the saturation-baseflow discharge relationship with the parameters shown, there are underlying patterns that may reveal features of the coevolved system. Primarily, we notice that the relationship between baseflow and saturated area has a concave up form in most cases, where the rate of change of saturated area increases with baseflow discharge. The simulations with the largest range in (log-transformed) A_{sat}^* (e.g., in Figure 4) appear to have a sigmoidal relationship, which can be divided into three regimes: rapid increase in saturated area with low baseflows, moderate increases in saturated area with moderate baseflows, and again rapid increases in saturated area with the highest baseflows. Several reference lines are included here for comparison with these regimes: $A_{sat}^* \sim Q_b^{*2}$, and $A_{sat}^* \sim Q_b^{*1/3}$, which are indicative of the rates of change in the upper and middle regimes, respectively.

How does the form of the saturation-baseflow discharge relationship relate to topography? We can contextualize the relationship by mapping points in $Q_b^*{-}A_{sat}^*$ space back to their respective spatially distributed saturation patterns. We chose to examine the results in Figure 6-4 ($\sigma = 8.0$, Ai $= 1.0$) in more detail, as it displays the sigmoid form well. The mapping is shown in Figure 7, where subplots B–E show hillshades colored blue where the the ground is saturated, corresponding to the labeled points in subplot A. Subplot (B) shows saturated areas cover only the second order and higher stream channels under low-flow conditions. In (C), saturated areas extend up through first order channels, and some channel-adjacent areas. Above (C), in (D), saturated areas emerge in many unchannelized concave regions, while by (E), saturation is widespread on all concave and planar regions, extending toward ridges. Critically, we can see that the inflection point near (C) represents the threshold above which saturated areas emerge outside of the channel network.

The geomorphic transition between in-channel and out-of-channel saturated areas at the transition between the middle and high baseflow discharge regimes translates to cases that do not display the full sigmoid relationship. Figure S12 shows how saturation patterns are related to points in the baseflow saturated area relationship for the case shown in 6-14 ($\sigma = 8.0$, Ai $= 0.25$). The point of maximum curvature is still associated with increasingly widespread saturation outside of the incised channel network. This supports the idea that the saturated area baseflow relationship embeds information about landscape morphology (at least hillslope-channel transitions). However, as the cases with large σ demonstrate, the extent and variability of saturated areas affect how much of the morphology is visible in this relationship.

Varying the drainage capacity γ affects the shape of the relationship between baseflow discharge and saturated area. The slope of the middle regime decreases with increasing γ, and the transition between the middle and upper regimes sharpens. Topographically, high γ cases also have greater relief, lower drainage density, and sharper transitions between channels and hillslopes (Litwin et al., 2021). In contrast, when the aquifer relief index β is small, the relationship between saturated area and baseflow discharge weakens, as shown in Figure S10. We will return to additional synthesis of these relationships in the discussion.

6 Discussion

6.1 How do topography and hydrology coevolve in DupuitLEM?

The purpose of the model developed in this paper is to help us better understand how real topography and hydrologic dynamics coevolve. Therefore, clearly laying out how the simulated topography and hydrologic dynamics coevolve in the model is important. A clear conceptual understanding would make it far easier to comprehend the sensitivity of the results to variations in the parameters presented above, and to ascertain where the model may provide insight and where it is deceptive. A visualization of our conceptual understanding is illustrated in Figure 8.

In DupuitLEM, hillslope morphology evolves to simultaneously shed water and regolith at the rates they are supplied. Water is supplied by rainfall and is lost to runoff (when it falls on saturated ground), subsurface drainage, and ET. Regolith is supplied by uplift or baselevel change U, may be redistributed by diffusive hillslope transport E_h, and removed by water erosion E_f, which is driven by runoff. Note that diffusive hillslope transport (unlike water erosion) does not remove regolith from the model domain for the most part (except at the boundaries). It only moves regolith around, smoothing the landscape out. Therefore, the simulated landscape morphology must therefore evolve towards a condition where the production of runoff is just sufficient to remove regolith by water erosion at (areal-averaged) rate U.

The key to achieving this balance is the perennial aquifer that forms in areas of topographic convergence. For the visualizations in Figure 8 the perennial aquifer has been defined based on 95% exceedance probability of aquifer thickness, and therefore corresponds to the "wet" saturation zones in Figures 4, 5, S9. The perennial aquifer appears as dark blue in Figure 8. When storms are large and infrequent (i.e., small σ) and transmissivity is moderate (i.e., $\gamma > 1$), the perennial water table determines which areas experience variable and perennial surface saturation and fluvial erosion. Perennial saturation occurs where the aquifer reaches the surface. Variable saturation occurs where the perennial water table is shallow enough that storms can raise the water table to the surface (the variable water table shown in Figure 8 is defined based on 5% exceedance probability of aquifer thickness). Therefore, the landscape morphology must evolve such that the spatial extent of the perennial aquifer is large enough to ensure sufficient surface runoff production.

How does it do so? In short: by balancing supply and demand. The aquifers are continually draining, and so to remain at or above their minimum level, the aquifers must receive a continual supply of lateral subsurface inflows from adjacent hillslopes. Both the drainage rate and supply rate are controlled by the topography. Therefore, by controlling these rates (and therefore the extent of the perennial aquifer) a topography can emerge that ensures sufficient runoff production to remove regolith at the supplied rate U.

The rate lateral flow is supplied to the perennial aquifer is determined by the size of the accumulated area upgradient, and the recharge rate in that area. That recharge is exported downgradient toward convergent areas as subsurface flow. When γ is sufficiently large, the subsurface flow is sufficiently efficient that uplands never experience surface saturation (these are the beige areas in Figure 8).

With no overland flow, upland regolith must be exported to convergent areas via diffusive hillslope transport if it is to be removed from the domain by water erosion. At each point in the uplands, the diffusive flux must transport not only the regolith supplied locally by uplift/base level change, but also the regolith arriving from upslope. The demand for increasing regolith transport capacity with distance from the ridge imparts a convex profile to the uplands, such that slope increases moving downhill, up to the critical slope S_c.

The rates of regolith and water export from the uplands to the convergent areas must strike a delicate balance. The regolith export must be *small* enough that it does not overwhelm the capacity of water erosion in the convergent areas to remove it. The water export must be *large* enough that it can sustain the perennial aquifer that makes that water erosion possible. However *both the regolith export and water export rates will depend on the accumulated area at the transition from uplands to convergent areas.* Therefore, the drainage density must adjust until these demands are in balance. If the drainage density is too small, excess lateral flow from the uplands will expand the perennial aquifer, leading to increased surface saturation and water erosion. If the drainage density is too large, lateral flow will be insufficient to maintain the perennial aquifer and promote water erosion, and so diffusive regolith flux will gradually fill the the convergent areas and remove them from the topography.

The rate of lateral inflow required to maintain the perennial aquifer is the one that matches the rate the perennial aquifer is draining downslope. The perennial aquifer drainage rate is controlled by the transmissivity $k_s b$ (which is fixed), by the local basement slope (which in DupuitLEM is determined by the topography because the permeable thickness b is constant in space), and potentially also by the level of the water table farther downgradient. As discussed later in this section, the latter is only important when β is small, and is overwhelmed by topographic gradients when β is large.

The roles of the recharge, transmissivity, and local slope at the transition from upland to convergent area are captured by the dimensionless parameter γ, which explains its importance in controlling drainage density. The slope of the convex uplands will tend to vary downslope in proportion with distance from the ridge and with ridge curvature. More precisely, at distance x we would expect the slope to be approximately $x\xi(x)h_g/\ell_g^2$. $\xi(x)$ is less than 1 and captures the effect of the nonlinearity in the hillslope diffusion law (in fact $\xi(x) = \tanh\left(xh_g/\ell_g^2/S_c\right) / \left(xh_g/\ell_g^2/S_c\right)$ for the exact form of the nonlinear diffusion law (Equation (3)). The maximum subsurface flow per unit width at that point is therefore $xk_s bh_g\xi(x)/\ell^2$. If area per contour width upslope from that point is $a(x)$ and the recharge is $r(x)$, it follows from the definition of γ that in the vicinity of the transition from uplands to where surface saturation and water erosion becomes important the following is true:

$$\frac{a(x)}{x} \times \frac{r(x)}{p} \times \frac{1}{\xi(x)} \approx \gamma \tag{24}$$

The first term on the left is the area per contour width divided by distance from the ridge. This quantity is a measure of the degree of topographic convergence. It will be ≈ 1 for straight slopes, < 1 for divergent areas, and > 1 for convergent areas. The second term measures the fraction of precipitation that becomes recharge, and is therefore influenced by the aridity Ai. Therefore, γ sets the degree of upland contributing area convergence needed to produce surface saturation and water erosion, modulated by the effect of water balance on recharge and nonlinear slope processes. This makes it clear why γ has such an important control on the drainage density of the coevolved landscapes (see Figure S8), and why aridity also plays a role (see Figure 4). Both effects are illustrated in Figure 8.

Note that γ depends on the transmissivity $k_s b$, rather than on the hydraulic conductivity k_s alone. That means it is possible to vary the permeable thickness while keeping γ constant by also varying the hydraulic conductivity inversely. Doing so amounts to varying β – a small β corresponds with a large permeable thickness. This was explored in Litwin et al. (2021), where β was referred to as the hillslope number Hi. This is perhaps regrettable, because although β is closely related to the hillslope number (as we shall see in Section 6.6), they are not the same thing. As with the hillslope number, when β is small, the aquifer thickness becomes large relative to the relief, making it possible for water table gradients to substantially differ from topographic gradients.

As a consequence, when β is small, the drainage rate of the perennial aquifer is more dependent on the landscape morphology downgradient. Because the slopes downgradient are gentler in lowland areas, the drainage rate is slower relative to the case with large β. Consequently the rate of lateral inflows can be smaller, and a smaller upslope area is needed to supply those inflows. This explains the larger areas of perennial and variable surface saturation when β is small (Figure 5), compared to when it is larger (Figure 4).

Some remarkable effects emerge when β is small, as shown in Figure 5. Under the right circumstances, the large permeable thickness allows the perennial aquifer to be connected across surface topographic divides, resulting in connected loops surrounding isolated 'islands' of uplands. Broad, low-gradient areas of perennial and variable saturation emerge (Figure 8), particularly around confluences.

The conceptual explanation of the model results presented here can also help us understand the variations with σ and Ai that appear in earlier figures. When σ is small, storms are large and infrequent relative to the subsurface storage capacity. Consequently, there is time between storms for the saturated aquifer to contract to only the most convergent areas, where it promotes transient surface saturation during subsequent storm. When σ is large, the perennial aquifer is more extensive because there is not time to contract before the next event, but the smaller storms mean transient surface saturation is less likely. These effects can be seen in Figures 4, 5, 8, and S8.

The variable source areas that emerge when σ is small allow for more widespread water erosion to remove regolith from the landscape. This results in lower relief than when σ is large (Figure 8).

The conceptual understanding presented so far does not account for all of the model behavior though, and additional details need to be considered. In our results, there is a transition between channelized and unchannelized topography between Ai $= 0.71$ and Ai $= 1.41$ in Figure 1, and the transition is more abrupt for large σ. This can be attributed to the reduced likelihood of recharge when Ai > 1 as captured in the Schenk model of the vadose zone. Recall that ET creates a storage deficit in the vadose zone that must be satisfied before rainfall from an individual storm event can produce recharge at depth. When Ai < 1, the potential ET between storms tends to be smaller than the rainfall that typically falls in each storm. Consequently the vadose zone tends to be wet at depth, and the effects of ET are limited to generating deficits close to the surface. However, when Ai > 1, the storage deficit that can accrue between storms is larger than the depth of rain that typically falls in each storm. Consequently the vadose zone is dry at depth, and recharge will only occur from a storm large enough to fill the profile, or when storms are clustered together. This becomes increasingly unlikely when σ is large, because σ includes the ratio of profile thickness to storm depth: $bn_e/p(\langle t_r\rangle + \langle t_b\rangle)$. Note that the likelihood of recharge *per se* is not related to the drainable porosity n_e but to the plant available water content n_a, and so the relevant dimensionless control on recharge is $\sigma\phi$.

Given less frequent recharge when Ai > 1, larger hillslopes are needed to supply the lateral flow necessary to sustain a perennial aquifer in areas of topographic convergence. This makes areas of permanent or variable saturation less extensive.

6.2 How does hydrogeomorphic coevolution play out in transient landscapes?

So far, we have focused on landscapes at dynamic equilibrium between uplift and erosion. This condition is powerful for studying the emergent behavior of LEMs (e.g., Bonetti et al., 2020; Theodoratos et al., 2018); however, transience is likely the norm in real landscapes (Whipple, 2001). Moreover, transience may offer clues to distinctive features of hydrological function at dynamic equilibrium. As a shorthand, we will use the term "age" to refer to the degree of progression toward a dynamic equilibrium, given an initial near-flat surface at baselevel. However, we recognize that this age is largely conceptual; real landscape evolution rarely follows such a linear progression or has such a clear initial state.

To examine transient evolution, we can select some points in time to examine. Although we could have selected points evenly spaced in time, the model state does not progress linearly. Change in mean elevation $\bar{z}$ for example tends to approach the steady-state value asymptotically (Figure S1). Assuming other features of interest may change in a similar way, we selected quantiles of mean elevation through time and examined topography and hydrological function at the corresponding times. Figure 9 presents the results of a single model run at times when mean elevation $\bar{z}$ is 10, 30, 60, and 90% of the final value. Figure 9M shows the time evolution of mean elevation and the four selected quantiles.

With increasing age, topography changes dramatically, from gentle slopes and high levels of drainage dissection, to steeper, broad hillslopes, and a more sparse drainage network (Figure 9A–D). The size of areas that are always and variably saturated decrease with increasing age (Figure 9E–H), from 7.1 and 54.4% of the modeled area, respectively, in the 10% mean elevation case to 0.6 and 24.1% in the 90% mean elevation case. The baseflow-saturated area relationship also evolved substantially (Figure 9I–L). Earlier in the development, the landscape exhibits greater saturated area, storage, and discharge. Mean saturated area decreases 65.0%, Q^* decreases 57.8%, and mean baseflow Q_b^* declines 27.0% over the course of the simulation presented, resulting in an increase in the baseflow index Q_b^*/Q^* with age. Although baseflow index increases, more developed landscapes experienced much lower discharge and storage at their driest states than the same landscape earlier in its development.

Even in the absence of subsurface hydrology, LEMs with flat initial conditions and uplift show increasing elevations as slopes steepen toward the point at which the denudation rate matches uplift. However, when subsurface hydrology is important, steepening slopes can also increase hydraulic gradients, increasing the capacity of the subsurface to drain water. In the absence of surface water that would form rills or channels, longer hillslopes can be maintained. However, hillslope length is limited by the increased recharge that a longer hillslope will collect and have to transport laterally downslope. Steeper hydraulic gradients also reduce the thickness of the aquifer needed to convey the same flux. Decreasing aquifer thickness affects recharge, which decreases when the water table is deeper, further reducing discharge and baseflow, as shown in Figures 9I–L.

The evolution seen in these results may mimic observations in post-glacial landscapes that evolve fluvial drainage from low relief, regolith mantled 'initial' states. The recently glaciated site shown in Figure 9N is located in northern Wisconsin, USA, and has low relief and abundant wetlands. Here, the water table is close to the surface, and subsurface lateral flow is less important for runoff generation than surface water connectivity. In contrast, the driftless region of Wisconsin was not recently glaciated (Figure

9O) and has greater relief and well-developed fluvial topography. Here springs and groundwater flow are more important for runoff generation. The driftless landscape is well drained, and watersheds may even have intermittent streamflow regimes (Sartz et al., 1977). The contrast between these two sites is consistent with observed decreases in runoff and saturation with age in our simulations. The evolution of post-glacial landscapes has been examined in further detail by Cullen et al. (2022), who found that groundwater flow plays an essential role in concentrating discharge and initiating the formation of fluvial topography in low-relief landscapes. They focused on the erosion of channels into a confined aquifer, rather than emergence of saturated areas from an unconfined aquifer. Further work could be conducted to unify the saturation excess runoff process presented here with the confined aquifer system that Cullen et al. (2022) have examined, which may explain more of the emergent hydrogeomorphic dynamics of post-glacial landscapes when considered together.

Lastly, we return to the question of the applicability of this catchment "age" more broadly. Although Troch et al. (2015) suggested that a hydrologically relevant age could be useful in understanding differences in hydrologic function between sites, in general the hydrologically relevant age of a landscape is not an easily defined quantity. They provided a framework for catchment coevolution in which age does not increase one-to-one with time, but rather increases at different (and potentially nonlinear) rates depending on lithology, climate, and tectonics. For example, the hydrologically relevant age may increase faster in a wetter climate than in a drier one. Applying this concept to our transient results, we see that differences in climate and subsurface properties affect the rate of relief change, which in turn affects the rate hydrological response changes. However, defining an age inevitably encounters the issue of defining an initial condition from which to start the clock. Troch et al. (2015) give the example of applying this framework to volcanic catchments, which have well-defined initial conditions from which the evolution can be measured (Jefferson et al., 2010; Yoshida & Troch, 2016). However, this may be the only case where such a clear initial hydrologic and geomorphic condition can be identified (although the post-glacial scenario we have discussed may be adequate). The direction of hydrologic response change with age is also particularly sensitive to the initial condition. Although we see decreasing saturation with time in our simulations, the trend may be very different if we were to take, for example, a Davisian approach in which the initial condition is a high plain that gradually erodes to baselevel (Davis, 1899). All of this indicates that evolving hydrological function is a complex story that would be best told within a geological context. More work would be needed before we can adequately apply the framework of evolving catchment function to real sites.

6.3 How realistic is the hydrology in DupuitLEM?

As illustrated in the results above, DupuitLEM produces landscapes that not only have the appearance of realistic topography, they function hydrologically as one would expect of a realistic landscape – up to a point. The model results deviate from what we might expect in a real landscape in several ways that are worth highlighting.

In the arid cases, as shown in Figure 2A, almost no runoff is produced by the model, and the resulting landscape is unchannelized. Many real arid landscapes will still produce substantial runoff at an aridity index of 2 (the maximum value we considered) (e.g., Wang & Wu, 2013), and exhibit widespread channelization. However, runoff is rarely produced by the interaction of the water table with the ground surface in those landscapes. In that sense our model is in full agreement. Instead, runoff in arid landscapes is more often generated by a low infiltration capacity relative to rainfall intensity (infiltration excess overland flow) (Wu et al., 2021). This mechanism is not included in the analysis here, but can be easily added through the modular modeling framework of DupuitLEM.

Another deviation from our expectations appears in the water balance when β and σ are small: as Figure 2D shows, deviations from the energy and water bounds are large in the Budyko plot. The increased quickflow fraction shown in Figure 2B (relative to the high β case in 2E) offers a clue as to why this deviation may be occurring. Because quickflow is primarily derived from precipitation on saturated areas, the deviations from energy and water limitations indicate these cases have more extensive saturated areas than their high β counterparts in Figure 2B. We can confirm this by examining spatial patterns of saturation in Figures 4 and 5. Indeed there are large areas of permanent saturation in the low β case. A larger fraction of quickflow is more likely when σ is small because in these cases storms more easily overwhelm available storage and produce additional saturated areas. As more precipitation becomes quickflow, less is available to become evapotranspiration, and the Budyko plot (Figure 2D) deviates from water and energy balance constraints.

The issue is exacerbated by the lack of ET from the saturated zone in our model. In reality ET may be substantial from the large permanently saturated areas shown in Figure 5, but in the model ET from these areas is zero (because ET is only accounted for in the unsaturated zone, and there is no unsaturated zone where the water table reaches the surface). This is an issue that can be explored in future work.

With the parameters we have considered, the other large deviation of $\langle AET \rangle / \langle P \rangle$ from $\langle PET \rangle / \langle P \rangle$ occurs when γ is small. This is somewhat paradoxical; Troch et al. (2013) found that landscapes with the longest drainage timescales tend to have the highest ET relative to precipitation because water that stays in the landscape longer is more likely to become ET. In fact, we can see that this is partially still the case in our results. Figure 2I shows that the baseflow fraction of remaining water is smallest when γ is small, indicating that more water is becoming ET. However, this is not controlling the overall water balance behavior. Instead, quickflow behavior controls the decrease in $\langle AET \rangle / \langle P \rangle$ with decreasing γ, as the proportion of precipitation that becomes quickflow declines precipitously with increasing γ, as shown in Figure 2H. Poorly drained landscapes (with low γ) have water tables closer to the surface, and greater saturated areas to generate quickflow during storms. Increasing this quickflow fraction decreases the water that remains available to become ET. Poorly drained landscapes also would be expected to make more water available for ET, as Troch et al. (2013) showed, but because our model ET cannot access water in the saturated zone, we are not able to reproduce this observation.

The one-way coupling of saturated and unsaturated flow has implications for runoff generation as well as ET. For example, with little or no additional recharge, the water table can rise rapidly into the capillary fringe (e.g., Crosbie et al., 2005; Gillham, 1984; Weeks, 2002). If the capillary fringe extends to the surface, as it may in wetter areas like concave hillslopes and valley bottoms, saturated areas could expand rapidly during storm events. Saturation of the soil profile due to wetting front propagation (e.g., Ogden et al., 2017) also could enhance the rapid emergence of saturated areas. On the other hand, ET from the saturated zone where it is near the surface could substantially reduce saturated areas during interstorm periods. Because we do not capture these features, we may substantially underestimate the variability of saturated areas and, depending on their relative importance, we may overestimate or underestimate runoff generation from saturation excess.

The form of our groundwater model may also affect features that we observe across our parameter space. In order to have tractable solutions for the landscape evolution model, the groundwater flow model we use relies on the Dupuit-Forcheimer approximations, which are valid where the component of flow normal to an impermeable lower boundary is small. This usually occurs when saturated thickness is small relative to hillslope or seepage face length (Bresciani et al., 2014), which may not be valid everywhere in our model parameter space. Even where this assumption is valid, the model focuses on relatively shallow groundwater flow paths. Field studies have shown that deeper flow paths through bedrock are important components of stream runoff, especially during baseflow conditions. Accounting for these deeper flow paths could increase baseflow discharge, changing the L'vovich water balance partitioning shown in Figure 2.

6.4 What processes were left out of DupuitLEM?

In the interest of creating a tractable model, we have left out several key climatic, hydrologic, and geomorphic processes that may affect the coevolution of runoff generation and topography. First, our representation of climate is simplified, as we neglected seasonality of precipitation or potential ET, which are important controls on the water balance and on the extent of saturated areas (Latron & Gallart, 2007; Yokoo et al., 2008). In the previous section we described two missing hydrological processes: infiltration excess overland flow and ET from the saturated zone. We also neglected the two-way coupling between saturated and unsaturated flow, and the presence of reinfiltration from run-on, both of which would require more sophisticated models and computationally-intensive iterative solutions. Deeper groundwater systems, which may make important contributions to baseflow, were also neglected (Hare et al., 2021). Considering only single direction flow routing with no depression storage also limits the development of valley bottoms and wetlands that can be important zones for saturation excess overland flow, although we did observe that valley bottoms can emerge despite model limitations in areas of the parameter space where aquifers are thick relative to topographic relief.

The style of water erosion is also limited in this model, as we consider only detachment-limited fluvial erosion, neglecting fluvial sediment deposition and factors such as groundwater sapping (Abrams et al., 2009; Laity & Malin, 1985) and pore-pressure driven landslides (Montgomery & Dietrich, 1994), which could be the subject of separate studies of coevolution between topography and groundwater systems.

We have also limited our study to understanding the evolution of topography, while the progressive weathering of rock and development of a regolith mantle are simultaneous components of critical zone evolution. Furthermore, we have considered only cases where the subsurface porosity and hydraulic conductivity is constant in a zone that uniformly parallel to topography. This can have unintended consequences. During transient evolution, areas that aggrade due to hillslope diffusion must turn sediment back into bedrock to maintain a constant thickness. Although this issue should not affect results at dynamic equilibrium, more work would be needed to accurately treat the subsurface in LEMs.

Recently, critical zone science has provided insights into the structure and evolution of the subsurface. Critical zone structure varies with depth, but may also vary systematically across landscapes, even mirroring topography in settings experiencing strong tectonic compression (St. Clair et al., 2015). Other hypotheses for subsurface evolution related to geomorphic, geochemical, and ecological processes have been put forth (Anderson et al., 2013, 2019; Brantley, Eissenstat, et al., 2017; Brantley, Lebedeva, et al., 2017; Harman & Cosans, 2019), and would likely result in different surface evolution when considering subsurface-driven runoff generation. Here we have laid the foundation for future modeling that can build toward whole critical zone evolution that considers both surface and subsurface features and processes.

6.5 Does DupuitLEM match field evidence for the relationship between saturated area and baseflow?

As we have shown, saturated area-discharge relationships contain information about runoff generation. However, variation in saturated area through time has not been widely reported in the literature as the measurements are labor intensive and can be sensitive to the judgement of the observer. Latron and Gallart (2007) compiled many published relationships into a single plot (reproduced in Figure 10) that shows a range of forms the relationship can take. We would like to compare our results with those in this plot, but so far we have only presented dimensionless versions. Choosing a set of dimensioned parameters (as is necessary to run the model) allows us to re-project the results into the dimensioned world for comparison. We did this for several results presented in Figure 6. The caveat to this approach is that the position of the results, especially along the x-axis, is subject to the particular dimensioned parameters we have chosen.

In humid climates, our results show strong resemblance to the concave up form observed by Dunne (1978) at Sleepers River, VT, USA. Saturated area and baseflow in this relationship were measured in Sleepers River Watershed W-2, which has gentle topography and relatively low permeability soils (Dunne et al., 1975), consistent with our low σ cases. Dunne et al. (1975) also observed lower variability in baseflow discharge and saturated areas in a steeper watershed with deeper and more permeable soils (Sleepers River Watershed WC-4, not shown), consistent with our high σ cases.

Field relationships by Ambroise (1986), Latron (1990), and Myrabø (1986) shown in Figure 10 have convex forms, where baseflow increases faster than saturated area in log-space. Some of our model results (e.g., Figure 7) also have convex forms for lower baseflow and saturated areas, but these relationships seem to have a different origin. In our case, the low baseflow regime was associated with channel network ephemerality, whereas the field studies are still primarily describing variable source areas in valley bottoms and adjacent hillslopes. In fact, the studies here with the lowest saturated extents appear to have linear or slightly concave relationships. However the linear relationship shown by Latron and Gallart (2007) is from a terraced landscape with fragmented saturated areas, which obscure the link between topography and baseflow. Reasons why observed relationships could be different from our model predictions are numerous. Our model has only considered a limited number of runoff generation and landscape evolution processes, and lacks the heterogeneities and complexities of real watersheds. However, it is encouraging that our results agree with field surveys from Dunne et al. (1975), given that ours are emergent features of coevolution.

6.6 How does DupuitLEM compare to the Dunne Diagram? Role of the hillslope number

Dunne (1978) presented a synthesis of how runoff generation mechanisms are related to topography, subsurface properties, and climate, often called the "Dunne Diagram" (Figure 11A). On the humid half of the diagram, Dunne associated saturation excess overland flow (i.e., Dunne overland flow) with gentle topography, and moderate to poorly drained soils. Subsurface storm flow was considered the opposite end member, and was associated with deeper, more permeable soils and steeper straight to convex topography.

We have mapped this conceptual relationship into a quantitative relationship between hydrological and geomorphic metrics to compare with our results to see whether the relationship applies. We quantified the geomorphic aspect by focusing on the difference between gentle and steep topography. We used topographic variance $\overline{Z}$ to quantify hillslope relief above valley bottoms without channel or hillslope delineation. Because of the domain boundary conditions (zero flux on all but the bottom) elevation increases systematically from the bottom to top boundaries, but not between the side boundaries, so we calculated the variance of topographic elevation for each horizontal slice of the domain, found the mean of the slice variances, and took the square root to obtain $\overline{Z}$ with units of length. We normalized $\overline{Z}$ with the characteristic height scale h_g for consistency with our dimensionless framework. The hydrologic metric is more straightforward. In our model, quickflow is generated primarily by Dunne overland flow, so the fraction of quickflow relative to total flow $\langle Q_f \rangle / \langle Q \rangle$ can quantify the importance of this mechanism.

In our results, the proportion of runoff generated by Dunne overland flow is almost entirely explained by the mean topographic variance of the watershed. Figure 11B shows

$\langle Q_f \rangle / \langle Q \rangle$ versus the mean topographic variance $\overline{Z}/h_g$. A clear mapping is shown between model runs that have gentle topography (low $\overline{Z}$) and those that generate runoff via Dunne overland flow. Figure 11C shows the same results, but colored to show the parameters. All cases are humid (Ai $= 0.5$), but have a range of values for the other parameters discussed in this paper. The most consistent pattern is that low γ cases tend to produce more quickflow. The storage index σ is a secondary control, with generally gentle topography and more Dunne overland flow produced when σ is small, provided that γ is not too large. Low β cases are the most likely to break expectations, which is expected given their tendency to evolve unique features like non-dendritic drainage networks and wide valley bottoms.

In the Dunne Diagram framework, Dunne overland flow is associated with moderate to poorly drained soils and low relief, gentle topography. In our model, poorly drained soils (relative to climate forcing) *produce* the associated gentle topography through water erosion to maintain the balance discussed in Section 6.1. The same can be said in the reverse direction. Well-drained soils produce steeper (higher mean variance) topography by expanding the zone where overland flow and water erosion do not occur, and therefore they develop a hydrological response dominated by subsurface flow (baseflow) rather than Dunne overland flow.

These results convey some information about the variably saturated area (shown in colors); however, close inspection of Figure 11B shows that the relationship between quickflow fraction and variably saturated area is not monotonically increasing. This is expected, because permanently saturated areas also can generate Dunne overland flow. However, variably saturated areas are distinct as an expression of the transition zone between areas of recharge and discharge, between diffusive transport and perennial water erosion. Could there be unique controls on variably saturated extent that are not captured in Figure 11?

The answer to this question may lie in connection to the hillslope number. In Section 4, we discussed how Litwin et al. (2021) called $\beta = h_g/h_a$ the hillslope number, which is defined as hillslope relief divided by the aquifer thickness. However the relief and mean aquifer thickness are emergent products of our coevolving system that we cannot specify ahead of time. We found that the actual emergent hillslope number has some bearing on the extent of variably saturated areas.

Before plotting the hillslope number, we first plotted the proportion of the domain classified as variably saturated against the dimensionless mean topographic variance (Figure 12A). The pattern is similar to that shown in Figure 11B, but with more scatter. The scatter shows greater difference in topographic variance between model runs that have the same variably saturated area but different σ (among other factors).

Dividing mean topographic variance by the actual mean aquifer thickness $\langle h \rangle$ rather than the characteristic height scale h_g gives an estimate of the emergent hillslope number, $\bar{Z}/\langle h \rangle$, on the y-axis. Figure 12B shows that this produces three tight relationships, separated by differences in aquifer relief index β. The hillslope numbers that we observe for the high β case are within the range described by Lyon and Troch (2007), who calculated hillslope numbers in the range of 18–96 for several real sites, although this will be sensitive to exactly how the relief is defined.

The importance of β in Figure 12B is expected given its role as a type of characteristic hillslope number based on model parameters. By normalizing the hillslope number with β we obtain a relationship (Figure 12C) that is tighter than the original between variably saturated are and topographic variance (Figure 12A). This indicates that there is a trade-off between the hillslope number and the proportion that is variably saturated: larger normalized hillslope numbers, which are associated with thin aquifers relative to relief, emerge with smaller variably saturated areas; thicker aquifers relative to relief emerge with greater variably saturated areas. The hillslope number has proved to be a useful concept to understand hydrologic response (Lyon & Troch, 2007), and here reveals a connection with emergent landscape features that to our knowledge, has not been shown before. We will not attempt to explain why this relationship exists here, but it certainly demonstrates that there are rich and largely unexplored avenues of research in emergent hydrogeomorphic dynamics.

6.7 Does coevolution explain Freeze's observation about the prevalence of Dunne overland flow?

Freeze (1980) observed a "delicate hydrologic balance on a hillslope" where only narrow combinations of parameters produced Dunne overland flow, despite the prevalence of Dunne overland flow in nature and the wide plausible ranges of parameter values. This led Freeze to hypothesize that there is a "very close relationship between climate, hydraulic conductivity, and the development of geomorphic landforms," in nature that tends to produce runoff as Dunne overland flow. We have also suggested that there is delicate balance in landscapes. However, within the scope of the processes in DupuitLEM, we did not see a tendency toward Dunne overland flow. Instead at geomorphic dynamic equilibrium water is partitioned to maintain balance between the size of recharge and discharge areas (Section 6.1). Consequently, coevolution reinforces the associations described by the Dunne diagram: places with thick, highly permeable soils evolve steep topography and subsurface-dominated runoff generation, whereas places with thinner less permeable soils evolve gentler topography and more Dunne overland flow (Section 6.6).

However, this does not indicate that these results represent conclusive evidence against Freeze's hypothesis. Although we explored the role of coevolving topography ("geomorphic landforms"), we selected climate and subsurface properties as parameters. The potential coevolution of these parameters is not accounted for. The transmissivity is a notable example of this. Li et al. (2014) broadened the exploration begun by Freeze (1980) and found evidence that indicates coevolution *between* subsurface properties and climate is important. They conducted a comprehensive study of the prevalence of Hortonian overland flow, Dunne overland flow, and subsurface stormflow using a suite of synthetic watersheds where climate, subsurface parameters, and topographic relief were varied independently. Runoff behavior varied widely with model parameters, and many runs did not conform to the Dunne diagram (e.g., arid climate with predominantly Dunne overland flow). Considering only model runs where the partitioning between ET and discharge was close to the empirical Budyko curve provided a behavioral constraint on the water balance that eliminated many, but not all, of the model runs that did not conform to the Dunne diagram. Although the tendency of watersheds to fall close to the Budyko curve is not fully understood, it has been associated with coevolution between soil, vegetation, and climate (Troch et al., 2013).

Our study indicates that hydrogeomorphic constraints could complement the Budyko water balance constraint. When Li et al. (2014) varied topography in their synthetic watersheds, they stretched the vertical dimension of a digital elevation model, effectively decoupling catchment morphology from other attributes, as they intended. Although the Budyko constraint eliminated some of the unrealistic runoff behavior by invoking the coevolution of climate, subsurface properties, and vegetation, Li et al. (2014) did not have an equivalent way to remove unrealistic behavior due to the relationship between climate, subsurface properties, and topography. Perhaps something like Equation (24) that relates transmissivity and climate to source area size and convergence, or the relationship between relief and quickflow fraction in Figure 11 could be used to provide a hydrogeomorphic behavioral constraint, and eliminate even more model runs that deviated from the Dunne diagram in Li et al. (2014). Such a constraint would need to be grounded in field evidence, but could use relationships derived from our simulations as plausible hypotheses. Although this is interesting in a theoretical sense, it could also be useful for constraining parameters in large-scale predictive models, where the appropriate values of subsurface parameters are unknown and difficult to measure.

7 Conclusions

Landscape evolution models are powerful tools for understanding the surface processes, acting as testing grounds for theories about how tectonics, climate, and lithology affect geomorphic features we observe today. Hydrology is often the glue that links these forcings and features together, as water is a powerful and ubiquitous agent for transporting solid and dissolved material from headwaters to depocenters. Here we have shown that LEMs have the potential to provide insights into the emergence of hydrological processes as well, provided the mechanisms underlying those processes are resolved in sufficient detail.

We have shown just one potential avenue for using an LEM to answer hydrological questions, in which runoff from shallow groundwater and precipitation on saturated areas provides the shear stress for detachment-limited erosion. Within this scope, we have revealed complex interactions between topography, aquifer properties, and hydrologic function, including water balance partitioning, patterns of recharge and saturated areas, and the emergence of variable source area runoff generation. Most importantly, we found that:

1. Drainage dissection increases not only with decreasing drainage capacity, as shown by (Litwin et al., 2021), but also with hydroclimatic properties including the subsurface storage capacity relative to storm depth and the aridity index.
2. When aquifers are thick relative to relief, it is possible to generate topographic features that are uncharacteristic of the streampower-diffusion LEM, including wide valley bottoms and nondendritic drainage networks.
3. In emergent landscapes, the relationship between saturated area and baseflow has a distinct bend: saturated area increases gradually with baseflow until the channel network is saturated, at which point saturated area increases rapidly across unchannelized areas with baseflow.
4. During evolution from a flat initial condition toward dynamic equilibrium, hydraulic gradients increase, which reduces the saturated area and flashiness of discharge.
5. At dynamic equilibrium, the size of the diffusion-dominated uplands that saturate very infrequently and supply recharge balances with the size of the lowlands that remain saturated and experience persistent water erosion.
6. The relationships between hydrology and geomorphology on the humid side of the Dunne Diagram, in which landscapes with deep soil and steep topography are associated with subsurface stormflow, and gentle topography and poorly drained soils are associated with saturation excess overland flow, can emerge as a result of coevolution.

This study lays the foundations for future work in which LEMs can be used to ask hydrological questions, and dynamic hydrological processes are given more consideration in spatially resolved landscape evolution models.

8 Notation

Variable definitions are below, with dimensions length L, time T, and mass M. Prime always indicates the dimensionless equivalent, where dimensionless equivalents are defined in the text.

variable	name	dimension
x, y	horizontal coordinates	[L]
t	time	[T]
$z(x, y, t)$	topographic elevation	[L]
$d(x, y)$	depth below surface	[L]
$h(x, y, t)$	aquifer thickness	[L]
$S_d(d, t)$	unsaturated storage below depth d	[L]
$A(x, y, t)$	area upslope	[L^2]
$a(x, y, t)$	area upslope per unit contour width	[L]
$\theta(x, y, t)$	aquifer base slope angle	[rad]
h_g	characteristic geomorphic height scale	[L]
ℓ_g	characteristic geomorphic length scale	[L]
t_g	characteristic geomorphic time scale	[T]
h_a	characteristic aquifer thickness	[L]
t_d	characteristic time to drain aquifer storage	[T]
l	domain side length	[L]
α	characteristic gradient	[-]
β	aquifer relief scale	[-]
γ	drainage capacity	[-]
δ	timescale factor	[-]
λ	domain scale factor	[-]
σ	water storage index	[-]
ρ	precipitation steadiness index	[-]
Ai	aridity index	[-]
ϕ	moisture content index	[-]
E_f	fluvial incision rate	[L/T]
E_h	hillslope diffusion rate	[L/T]
E_0	streampower threshold	[L/T]
S_c	critical slope	[-]
U	uplift rate	[L/T]
K	streampower incision coefficient	[1/T]
v_0	characteristic contour width	[L]
b	permeable thickness	[L]
q_h	hillslope sediment transport rate	[L^2/T]
D	hillslope diffusivity	[L^2/T]
k_{sf}	timestep scaling factor	[-]
$R_d(d, t)$	recharge for water table at depth d	[L]
$r(x, y, t)$	recharge rate	[L/T]
$q(x, y, t)$	groundwater specific-discharge	[L^2/T]
$q_s(x, y, t)$	local surface runoff	[L/T]
$Q(x, y, t)$	discharge	[L^3/T]
$Q^*(x, y, t)$	dimensionless discharge	[-]
p	average precipitation rate	[L/T]
pet	interstorm potential evapotranspiration rate	[L/T]
d_s	storm depth	[L]
t_r	storm duration	[T]
t_b	interstorm duration	[T]
i	precipitation intensity	[L/T]
k_s	hydraulic conductivity	[L/T]
n_e	drainable porosity	[-]
n_a	plant-available water content	[-]
$\mathcal{G}$	step function	
$\mathcal{R}$	ramp function	

cont.

variable	name	dimension
$\langle PET \rangle$	long-term average potential evapotranspiration rate	[L^3/T]
$\langle AET \rangle$	long-term average actual evapotranspiration rate	[L^3/T]
$\langle P \rangle$	long-term average precipitation rate	[L^3/T]
$\langle R \rangle$	long-term average recharge rate	[L^3/T]
$\langle Q_b \rangle$	long-term average baseflow discharge	[L^3/T]
$\langle Q_f \rangle$	long-term average quickflow discharge	[L^3/T]
$Q_b(t)$	baseflow discharge for model domain	[L^3/T]
$Q_b^*(t)$	dimensionless baseflow discharge for model domain	[-]
$S(t)$	model domain saturated storage	[L^3]
$S^*(t)$	dimensionless model domain saturated storage	[$-$]
A_{tot}	model domain area	[L^2]
$A_{sat}(t)$	area saturated	[L^2]
$A^*_{sat}(t)$	dimensionless area saturated	[-]

Appendices

A Nondimensionalization of landscape evolution with nonlinear diffusion

Litwin et al. (2021) nondimensionalized the landscape evolution equation using the concept of symmetry groups. Here we modify that nondimensionalization to include nonlinear hillslope diffusion (Equation (4)) rather than linear diffusion. We begin by replacing the dimensioned model parameters with equivalent combinations of the characteristic scales:

$$\frac{\partial z}{\partial t} = -\frac{\sqrt{v_0}}{t_g}\langle Q^* \rangle \sqrt{a}|\nabla z| + \frac{\ell_g^2}{t_g}\nabla \cdot \left(\nabla z \left(1 + (|\nabla z|/S_c)^2\right)\right) + \frac{h_g}{t_g} \tag{A1}$$

$$-\nabla \cdot \left(a\frac{\nabla z}{|\nabla z|}\right) = 1 \tag{A2}$$

The hydrological equations are:

$$\frac{\partial h}{\partial t} = \frac{h_a}{t_d}\left(\frac{r}{p} - \frac{\nabla \cdot q}{p} - \frac{q_s}{p}\right) \tag{A3}$$

$$\frac{q}{p} = -h\cos^2(\arctan|\nabla z|)\frac{\ell_g^2}{h_g h_a}\left(\nabla h + \nabla z\right) \tag{A4}$$

$$\frac{q_s}{p} = \mathcal{G}\left(\frac{h}{b}\right)\mathcal{R}\left(\frac{r}{p} - \frac{\nabla \cdot q}{p}\right) \tag{A5}$$

$$Q^* = \frac{1}{Ap}\int_A q_s dA_c \tag{A6}$$

We now seek to identify sets of parameters that can be scaled by a constant factor ‘c’ while leaving the equations unchanged. See Litwin et al. (2021) for a detailed explanation of this approach. We find that the same two groups of parameters used previously for the DupuitLEM model can again be used:

$$\begin{aligned} &\{t \to ct, t_g \to ct_g, t_d \to ct_d\} \\ &\{x \to cx, y \to cy, a \to ca, A \to c^2A, l_g \to cl_g, \\ &\quad q \to cq, z \to cz, h \to ch, h_g \to ch_g, h_a \to ch_a, b \to cb\} \end{aligned} \tag{A7}$$

B Nondimensionalization of Schenk Vadose Model

For simplicity of notation, we begin by rewriting governing equation of Schenk (2008) (equation (11)) with the following simplifications: $S(d,t) \rightarrow S_d$, $S(d,t{+}\Delta t){-}S(d,t) \rightarrow \Delta S_d$, $i(t)\Delta t \rightarrow I$, and $e(t)\Delta t \rightarrow PET$.

$$\Delta S_d = \min\left(dn_a - S_d, I\right) - \min\left(S_d, PET\right) \tag{A8}$$

Now we introduce the dimensionless variables:

$$\begin{aligned} d &= d'b && \text{(A9)}\\ S_d &= S_d' p(\langle t_r\rangle + \langle t_r\rangle) && \text{(A10)}\\ \Delta S_d &= \Delta S_d' p(\langle t_r\rangle + \langle t_r\rangle) && \text{(A11)}\\ I &= I' p(\langle t_r\rangle + \langle t_r\rangle) && \text{(A12)}\\ PET &= PET' pet\langle t_r\rangle && \text{(A13)} \end{aligned}$$

where the prime indicates a dimensionless equivalent quantity. Substitution yields the following:

$$\Delta S_d' = \min\left(\frac{d'bn_a}{p(\langle t_r\rangle + \langle t_r\rangle)} - S_d', I'\right) - \min\left(S_d', PET'\frac{pet\langle t_r\rangle}{p(\langle t_r\rangle + \langle t_r\rangle)}\right). \tag{A14}$$

We rewrite this as:

$$\Delta S_d' = \min\left(d'\sigma\phi - S_d', I'\right) - \min\left(S_d', PET'\mathrm{Ai}\right) \tag{A15}$$

where:

$$\begin{aligned} \sigma =& \frac{bn_e}{p\left(\langle t_r\rangle + \langle t_b\rangle\right)} && \text{Water storage index} && \text{(A16)}\\ \mathrm{Ai} =& \frac{pet\langle t_b\rangle}{p\left(\langle t_r\rangle + \langle t_b\rangle\right)} && \text{Aridity index} && \text{(A17)}\\ \phi =& n_a/n_e && \text{Moisture content index} && \text{(A18)} \end{aligned}$$

In order to uniquely determine the mean storm duration and interstorm duration (Equations (8) and (9)), we introduce one final parameter:

$$\rho = \frac{\langle t_r\rangle}{\langle t_r\rangle + \langle t_b\rangle} \qquad \text{Precipitation steadiness index} \tag{A19}$$

Likewise, the simplified expression for storm recharge R (equation (12)) is:

$$R_d = I - \min\left(dn_a - S_d, I\right) \tag{A20}$$

and the equivalent dimensionless form is:

$$R_d' = I' - \min\left(\frac{d'bn_a}{p(\langle t_r\rangle + \langle t_r\rangle)} - S_d', I'\right) \tag{A21}$$

where $R_d = R_d' p(\langle t_r\rangle + \langle t_r\rangle)$. When the dimensionless parameter definitions are substituted, this becomes:

$$R_d' = I' - \min\left(d'\sigma\phi - S_d', I'\right). \tag{A22}$$

9 Open Research

No original data are presented in this paper. The Python package DupuitLEM v1.1 (Litwin et al., 2023a) contains the models and scripts used to generate and post-process the model output. All model output are archived on Zenodo (Litwin et al., 2023b). Landlab v2.0 (Barnhart et al., 2020) is a core dependency of DupuitLEM. The complete list of input parameter values can be found in Table S1 of Supporting Information S1, and in the model output archive.

Acknowledgments

This work was supported by National Science Foundation grants EAR-2012264, EAR-1654194, ACI-1450409, EAR-1725774, and EAR-1831623. Model simulations were carried out at the Advanced Research Computing at Hopkins (ARCH) core facility (rockfish.jhu.edu), which is supported by the National Science Foundation (NSF) grant number OAC-1920103. Any use of trade, firm, or product names is for descriptive purposes only and does not imply endorsement by the U.S. Government.

References

Abrams, D. M., Lobkovsky, A. E., Petroff, A. P., Straub, K. M., McElroy, B., Mohrig, D. C., ... Rothman, D. H. (2009). Growth laws for channel networks incised by groundwater flow. *Nature Geoscience*, *2*(3), 193–196. doi: 10.1038/ngeo432

Ambroise, B. (1986). Rôle hydrologique des surfaces saturées en eau dans le bassin de Ringelbach à Soultzeren (Hautes Vosges, France). In *Colloque scientifique des Universités du Rhin supérieur «Recherches sur l'environnement dans la région». 1* (pp. 619–630).

Anand, S. K., Bonetti, S., Camporeale, C., Hooshyar, M., & Porporato, A. (2022). Comment on "Groundwater affects the geomorphic and hydrologic properties of coevolved landscapes" by Litwin et al. *Journal of Geophysical Research: Earth Surface*, *127*(10), e2022JF006669. doi: https://doi.org/10.1029/2022JF006669

Anderson, R. S., Anderson, S. P., & Tucker, G. E. (2013). Rock damage and regolith transport by frost: An example of climate modulation of the geomorphology of the critical zone. *Earth Surface Processes and Landforms*, *38*(3), 299–316. doi: 10.1002/esp.3330

Anderson, R. S., Rajaram, H., & Anderson, S. P. (2019). Climate driven coevolution of weathering profiles and hillslope topography generates dramatic differences in critical zone architecture. *Hydrological Processes*, *33*(1), 4–19. doi: 10.1002/hyp.13307

Andrews, D. J., & Bucknam, R. C. (1987). Fitting degradation of shoreline scarps by a nonlinear diffusion model. *Journal of Geophysical Research*, *92*(B12), 12857–12867.

Barenblatt, G. I. (1996). *Scaling, self-similarity, and intermediate asymptotics* (No. 14). Cambridge; New York: Cambridge University Press.

Barnhart, K. R., Glade, R. C., Shobe, C. M., & Tucker, G. E. (2018). Terrainbento 1.0: A Python package for multi-model analysis in long-term drainage basin evolution. *Geoscientific Model Development Discussions*(October), 1–57. doi: 10.5194/gmd-2018-204

Barnhart, K. R., Hutton, E. W. H., Tucker, G. E., Gasparini, N. M., Istanbulluoglu, E., Hobley, D. E. J., ... Bandaragoda, C. (2020). Short communication: Landlab v2.0: A software package for Earth surface dynamics. *Earth Surface Dynamics*, *8*(2), 379–397. doi: 10.5194/esurf-8-379-2020

Bishop, P. (2007). Long-term landscape evolution: Linking tectonics and surface processes. *Earth Surface Processes and Landforms*, *32*(3), 329–365. doi: 10.1002/esp.1493

Bonetti, S., Bragg, A. D., & Porporato, A. (2018). On the theory of drainage area for regular and non-regular points. *Proceedings of the Royal Society A:*

Mathematical, Physical and Engineering Sciences, *474*(2211), 20170693. doi: 10.1098/rspa.2017.0693

Bonetti, S., Hooshyar, M., Camporeale, C., & Porporato, A. (2020). Channelization cascade in landscape evolution. *Proceedings of the National Academy of Sciences*, *117*(3), 1375–1382. doi: 10.1073/pnas.1911817117

Botter, G., Porporato, A., Rodriguez-Iturbe, I., & Rinaldo, A. (2007). Basin-scale soil moisture dynamics and the probabilistic characterization of carrier hydrologic flows: Slow, leaching-prone components of the hydrologic response. *Water Resources Research*, *43*(2), 1–14. doi: 10.1029/2006WR005043

Brantley, S. L., Eissenstat, D. M., Marshall, J. A., Godsey, S. E., Balogh-Brunstad, Z., Karwan, D. L., ... Weathers, K. C. (2017). Reviews and syntheses: On the roles trees play in building and plumbing the critical zone. *Biogeosciences*, *14*(22), 5115–5142. doi: 10.5194/bg-14-5115-2017

Brantley, S. L., Lebedeva, M. I., Balashov, V. N., Singha, K., Sullivan, P. L., & Stinchcomb, G. (2017). Toward a conceptual model relating chemical reaction fronts to water flow paths in hills. *Geomorphology*, *277*, 100–117. doi: 10.1016/j.geomorph.2016.09.027

Braun, J., & Willett, S. D. (2013). A very efficient O(n), implicit and parallel method to solve the stream power equation governing fluvial incision and landscape evolution. *Geomorphology*, *180–181*, 170–179. doi: 10.1016/j.geomorph.2012.10.008

Bresciani, E., Davy, P., & de Dreuzy, J. R. (2014). Is the Dupuit assumption suitable for predicting the groundwater seepage area in hillslopes? *Water Resources Research*, *50*(3), 2394–2406. doi: 10.1002/2013WR014284

Brutsaert, W. (2005). *Hydrology: An introduction*. Cambridge; New York: Cambridge University Press.

Budyko, M. I. (1974). *Climate and life* (No. 18). New York: Academic Press.

Callahan, R. P., Ferrier, K. L., Dixon, J., Dosseto, A., Hahm, W. J., Jessup, B. S., ... Riebe, C. S. (2019). Arrested development: Erosional equilibrium in the southern Sierra Nevada, California, maintained by feedbacks between channel incision and hillslope sediment production. *GSA Bulletin*, *131*(7-8), 1179–1202. doi: 10.1130/B35006.1

Campbell Grant, E. H., Lowe, W. H., & Fagan, W. F. (2007). Living in the branches: Population dynamics and ecological processes in dendritic networks. *Ecology Letters*, *10*(2), 165–175. doi: 10.1111/j.1461-0248.2006.01007.x

Chen, A., Darbon, J., & Morel, J.-M. (2014). Landscape evolution models: A review of their fundamental equations. *Geomorphology*, *219*, 68–86. doi: 10.1016/j.geomorph.2014.04.037

Childs, E. C. (1971). Drainage of groundwater resting on a sloping bed. *Water Resources Research*, *7*(5), 1256–1263. doi: 10.1029/WR007i005p01256

Crosbie, R. S., Binning, P., & Kalma, J. D. (2005). A time series approach to inferring groundwater recharge using the water table fluctuation method. *Water Resources Research*, *41*(1). doi: 10.1029/2004WR003077

Cullen, C., Anders, A. M., Lai, J., & Druhan, J. L. (2022). Numerical modeling of groundwater-driven stream network evolution in low-relief post-glacial landscapes. *Earth Surface Processes and Landforms*, *47*(2), 658–671. doi: 10.1002/esp.5278

Davis, W. M. (1899). The geographical cycle. *The Geographical Journal*, *14*(5), 481–504. doi: 10.2307/1774538

Deal, E., Braun, J., & Botter, G. (2018). Understanding the role of rainfall and hydrology in determining fluvial erosion efficiency. *Journal of Geophysical Research: Earth Surface*, *123*(4), 744–778. doi: 10.1002/2017JF004393

Dietrich, W. E., Bellugi, D. G., Sklar, L. S., Stock, J. D., Heimsath, A. M., & Roering, J. J. (2003). Geomorphic transport laws for predicting landscape form and dynamics. In P. R. Wilcock & R. M. Iverson (Eds.), *Geophysical Monograph*

Series (pp. 103–132). Washington, D.C.: American Geophysical Union. doi: 10.1029/135GM09

Doane, T. H., Furbish, D. J., Roering, J. J., Schumer, R., & Morgan, D. J. (2018). Nonlocal sediment transport on steep lateral moraines, eastern Sierra Nevada, California, USA. *Journal of Geophysical Research: Earth Surface*, *123*(1), 187–208. doi: 10.1002/2017JF004325

Dunne, T. (1978). Field studies of hillslope flow processes. In M. J. Kirkby (Ed.), *Hillslope hydrology.* Chichester; New York: Wiley.

Dunne, T., & Black, R. D. (1970). Partial area contributions to storm runoff in a small New England watershed. *Water Resources Research*, *6*(5), 1296–1311. doi: 10.1029/WR006i005p01296

Dunne, T., Moore, T., & Taylor, C. H. (1975). Recognition and prediction of runoff-producing zones in humid regions. *Hydrol. Sci. Bull*, *20*(3), 305–327.

Eagleson, P. (1978). Introduction to water balance dynamics. *Water Resources Research*, *14*(5), 705–712. doi: 10.1016/j.compchemeng.2012.11.011

Freeze, R. A. (1980). A stochastic-conceptual analysis of rainfall-runoff processes on a hillslope. *Water Resources Research*, *16*(2), 391–408. doi: 10.1029/WR016i002p00391

Gabet, E. J. (2003). Sediment transport by dry ravel. *Journal of Geophysical Research: Solid Earth*, *108*(B1). doi: 10.1029/2001JB001686

Ganti, V., Passalacqua, P., & Foufoula-Georgiou, E. (2012). A sub-grid scale closure for nonlinear hillslope sediment transport models. *Journal of Geophysical Research: Earth Surface*, *117*(F2). doi: 10.1029/2011JF002181

Gillham, R. W. (1984). The capillary fringe and its effect on water-table response. *Journal of Hydrology*, *67*(1), 307–324. doi: 10.1016/0022-1694(84)90248-8

Godard, V., & Tucker, G. E. (2021). Influence of climate-forcing frequency on hillslope response. *Geophysical Research Letters*, *48*(18), e2021GL094305. doi: 10.1029/2021GL094305

Haitjema, H. M., & Mitchell-Bruker, S. (2005). Are water tables a subdued replica of the topography? *Groundwater*, *43*(6), 781–786. doi: 10.1111/j.1745-6584.2005.00090.x

Hare, D. K., Helton, A. M., Johnson, Z. C., Lane, J. W., & Briggs, M. A. (2021). Continental-scale analysis of shallow and deep groundwater contributions to streams. *Nature Communications*, *12*(1), 1450. doi: 10.1038/s41467-021-21651-0

Harman, C. J., & Cosans, C. L. (2019). A low-dimensional model of bedrock weathering and lateral flow coevolution in hillslopes: 2. Controls on weathering and permeability profiles, drainage hydraulics, and solute export pathways. *Hydrological Processes*(December 2018), 1168–1190. doi: 10.1002/hyp.13385

Harman, C. J., & Troch, P. A. (2014). What makes Darwinian hydrology "Darwinian"? Asking a different kind of question about landscapes. *Hydrology and Earth System Sciences*, *18*(2), 417–433. doi: 10.5194/hess-18-417-2014

Hewlett, J. D., & Hibbert, A. R. (1967). Factors affecting the response of small watersheds to precipitation in humid areas. In *Int. Symp. Forest Hydrology.* doi: 10.1177/0309133309338118

Hobley, D. E. J., Adams, J. M., Nudurupati, S. S., Hutton, E. W. H., Gasparini, N. M., Istanbulluoglu, E., & Tucker, G. E. (2017). Creative computing with Landlab: An open-source toolkit for building, coupling, and exploring two-dimensional numerical models of Earth-surface dynamics. *Earth Surface Dynamics*, *5*(1), 21–46. doi: 10.5194/esurf-5-21-2017

Horton, R. E. (1933). The role of infiltration in the hydrologic cycle. *Eos, Transactions American Geophysical Union*. doi: 10.1029/TR014i001p00446

Huang, X., & Niemann, J. D. (2006). Modelling the potential impacts of groundwater hydrology on long-term drainage basin evolution. *Earth Surface Processes and Landforms*. doi: 10.1002/esp.1369

Huang, X., & Niemann, J. D. (2008). How do streamflow generation mechanisms affect watershed hypsometry? *Earth Surface Processes and Landforms*. doi: 10.1002/esp.1573

Ijjász-Vásquez, E. J., Bras, R. L., & Moglen, G. E. (1992). Sensitivity of a basin evolution model to the nature of runoff production and to initial conditions. *Water Resources Research*. doi: 10.1029/92WR01561

Jefferson, A., Grant, G. E., Lewis, S. L., & Lancaster, S. T. (2010). Coevolution of hydrology and topography on a basalt landscape in the Oregon Cascade Range, USA. *Earth Surface Processes and Landforms*, *35*(7), 803–816. doi: 10.1002/esp.1976

Jensen, C. K., McGuire, K. J., & Prince, P. S. (2017). Headwater stream length dynamics across four physiographic provinces of the Appalachian Highlands. *Hydrological Processes*, *31*(19), 3350–3363. doi: 10.1002/hyp.11259

Lague, D., Hovius, N., & Davy, P. (2005). Discharge, discharge variability, and the bedrock channel profile. *Journal of Geophysical Research: Earth Surface*, *110*(F4). doi: 10.1029/2004JF000259

Laity, J. E., & Malin, M. C. (1985). Sapping processes and the development of theater-headed valley networks on the Colorado Plateau. *Geological Society of America Bulletin*, *96*, 203–217.

Langston, A. L., & Tucker, G. E. (2018). Developing and exploring a theory for the lateral erosion of bedrock channels for use in landscape evolution models. *Earth Surface Dynamics*, *6*(1), 1–27. doi: 10.5194/esurf-6-1-2018

Lapides, D. A., David, C., Sytsma, A., Dralle, D., & Thompson, S. (2020). Analytical solutions to runoff on hillslopes with curvature: Numerical and laboratory verification. *Hydrological Processes*, hyp.13879. doi: 10.1002/hyp.13879

Latron, J. (1990). Caractérisation géomorphologique et hydrologique du bassin versant versant du Strengbach (Aubure). *Université Louis Pasteur, Strasbourg I*.

Latron, J., & Gallart, F. (2007). Seasonal dynamics of runoff-contributing areas in a small mediterranean research catchment (Vallcebre, Eastern Pyrenees). *Journal of Hydrology*, *335*(1), 194–206. doi: 10.1016/j.jhydrol.2006.11.012

Li, H. Y., Sivapalan, M., Tian, F., & Harman, C. J. (2014). Functional approach to exploring climatic and landscape controls of runoff generation: 1. Behavioral constraints on runoff volume. *Water Resources Research*. doi: 10.1002/2014WR016307

Litwin, D. G., Barnhart, K. R., Tucker, G. E., & Harman, C. J. (2023a). *DupuitLEM: groundwater landscape evolution with landlab.* Zenodo. doi: 10.5281/zenodo.7620978

Litwin, D. G., Barnhart, K. R., Tucker, G. E., & Harman, C. J. (2023b). *Model output for "Catchment coevolution and the geomorphic origins of variable source area hydrology"*. Zenodo. doi: 10.5281/zenodo.7621354

Litwin, D. G., Tucker, G., Barnhart, K., & Harman, C. J. (2020). GroundwaterDupuitPercolator: A Landlab component for groundwater flow. *Journal of Open Source Software*, *5*(46), 1935. doi: 10.21105/joss.01935

Litwin, D. G., Tucker, G. E., Barnhart, K. R., & Harman, C. J. (2021). Groundwater affects the geomorphic and hydrologic properties of coevolved landscapes. *Journal of Geophysical Research: Earth Surface*, *127*, e2021JF006239. doi: 10.1029/2021JF006239

Litwin, D. G., Tucker, G. E., Barnhart, K. R., & Harman, C. J. (2022). Reply to comment by Anand et al. on "Groundwater affects the geomorphic and hydrologic properties of coevolved landscapes". *Journal of Geophysical Research: Earth Surface*, *127*(10), e2022JF006722. doi: 10.1029/2022JF006722

Luijendijk, E. (2022). Transmissivity and groundwater flow exert a strong influence on drainage density. *Earth Surface Dynamics*, *10*(1), 1–22. doi: 10.5194/esurf-10-1-2022

L'vovich. (1979). *World Water Resources and their Future* (First ed.). American

Geophysical Union (AGU). doi: 10.1029/SP013

Lyon, S. W., & Troch, P. A. (2007). Hillslope subsurface flow similarity: Real-world tests of the hillslope Péclet number. *Water Resources Research*, *43*(7). doi: 10.1029/2006WR005323

Marçais, J., de Dreuzy, J. R., & Erhel, J. (2017). Dynamic coupling of subsurface and seepage flows solved within a regularized partition formulation. *Advances in Water Resources*, *109*, 94–105. doi: 10.1016/j.advwatres.2017.09.008

McMillan, H. (2020). Linking hydrologic signatures to hydrologic processes: A review. *Hydrological Processes*, *34*(6), 1393–1409. doi: 10.1002/hyp.13632

Montgomery, D. R., & Dietrich, W. E. (1994). A physically based model for the topographic control on shallow landsliding. *Water Resources Research*, *30*(4), 1153–1171. doi: 10.1029/93WR02979

Myrabø, S. (1986). Runoff studies in a small catchment: Paper presented at the Nordic Hydrological Conference (Reykjavik, Iceland, August – 1986). *Hydrology Research*, *17*(4-5), 335–346. doi: 10.2166/nh.1986.0025

Ogden, F. L., Allen, M. B., Lai, W., Zhu, J., Seo, M., Douglas, C. C., & Talbot, C. A. (2017). The soil moisture velocity equation. *Journal of Advances in Modeling Earth Systems*, *9*(2), 1473–1487. doi: 10.1002/2017MS000931

O'Loughlin, E. M. (1981). Saturation regions in catchments and their relations to soil and topographic properties. *Journal of Hydrology*, *53*(3-4), 229–246. doi: 10.1016/0022-1694(81)90003-2

Pelletier, J. D. (2013). 2.3 Fundamental principles and techniques of landscape evolution modeling. In J. F. Shroder (Ed.), *Treatise on Geomorphology* (pp. 29–43). San Diego: Academic Press. doi: 10.1016/B978-0-12-374739-6.00025-7

Prancevic, J. P., & Kirchner, J. W. (2019). Topographic controls on the extension and retraction of flowing streams. *Geophysical Research Letters*, *46*, 2084–2092. doi: 10.1029/2018GL081799

Riebe, C. S., Hahm, W. J., & Brantley, S. L. (2017). Controls on deep critical zone architecture: A historical review and four testable hypotheses. *Earth Surface Processes and Landforms*, *42*(1), 128–156. doi: 10.1002/esp.4052

Rodriguez-Iturbe, I., Porporato, A., Ridolfi, L., Isham, V., Coxi, D. R., Society, T. R., & Sciences, E. (1999). Probabilistic modelling of water balance at a point: The role of climate, soil and vegetation. *Proceedings of the Royal Society of London.Series A: Mathematical, Physical and Engineering Sciences*, *455*(1990), 3789–3805. doi: 10.1098/rspa.1999.0477

Roering, J. J., Kirchner, J. W., & Dietrich, W. E. (1999). Evidence for nonlinear, diffusive sediment transport on hillslopes and implications for landscape morphology. *Water Resources Research*, *35*(3), 853–870. doi: 10.1029/1998WR900090

Roering, J. J., Kirchner, J. W., & Dietrich, W. E. (2001). Hillslope evolution by nonlinear, slope-dependent transport: Steady state morphology and equilibrium adjustment timescales. *Journal of Geophysical Research: Solid Earth*, *106*(B8), 16499–16513. doi: 10.1029/2001jb000323

Rosenbloom, N. A., & Anderson, R. S. (1994). Hillslope and channel evolution in a marine terraced landscape, Santa Cruz, California. *Journal of Geophysical Research: Solid Earth*, *99*(B7), 14013–14029. doi: 10.1029/94JB00048@10.1002/(ISSN)2169-9356.TECTOP1

Rossi, M. W., Whipple, K. X., & Vivoni, E. R. (2016). Precipitation and evapotranspiration controls on daily runoff variability in the contiguous United States and Puerto Rico. *Journal of Geophysical Research: Earth Surface*, *121*(1), 128–145. doi: 10.1002/2015JF003446

Sartz, R. S., Curtis, W. R., & Tolsted, D. N. (1977). Hydrology of small watersheds in Wisconsin's driftless area. *Water Resources Research*, *13*(3), 524–530. doi: 10.1029/WR013i003p00524

Schenk, H. J. (2008). The shallowest possible water extraction profile: A null model for global root distributions. *Vadose Zone Journal*, *7*(3), 1119–1124. doi: 10.2136/vzj2007.0119

Singha, K., & Navarre-Sitchler, A. (2022). The importance of groundwater in critical zone science. *Groundwater*, *60*(1), 27–34. doi: 10.1111/gwat.13143

St. Clair, J., Moon, S., Holbrook, W. S., Perron, J. T., Riebe, C. S., Martel, S. J., ... De Richter, D. B. (2015). Geophysical imaging reveals topographic stress control of bedrock weathering. *Science*, *350*(6260), 534–538. doi: 10.1126/science.aab2210

Theodoratos, N., Seybold, H., & Kirchner, J. W. (2018). Scaling and similarity of a stream-power incision and linear diffusion landscape evolution model. *Earth Surface Dynamics*, *6*(3), 779–808. doi: 10.5194/esurf-6-779-2018

Troch, P. A., Carrillo, G., Sivapalan, M., Wagener, T., & Sawicz, K. (2013). Climate-vegetation-soil interactions and long-term hydrologic partitioning: Signatures of catchment co-evolution. *Hydrology and Earth System Sciences*, *17*(6), 2209–2217. doi: 10.5194/hess-17-2209-2013

Troch, P. A., Lahmers, T., Meira, A., Mukherjee, R., Pedersen, J. W., Roy, T., & Valdes-Pineda, R. (2015). Catchment coevolution: A useful framework for improving predictions of hydrological change? *Water Resources Research*, *51*(7), 4903–4922. doi: 10.1002/2015WR017032

Troch, P. A., Paniconi, C., & Van Loon, E. E. (2003). Hillslope-storage Boussinesq model for subsurface flow and variable source areas along complex hillslopes: 1. Formulation and characteristic response. *Water Resources Research*, *39*(11). doi: 10.1029/2002WR001728

Tucker, G. E. (2004). Drainage basin sensitivity to tectonic and climatic forcing: Implications of a stochastic model for the role of entrainment and erosion thresholds. *Earth Surface Processes and Landforms*, *29*(2), 185–205. doi: 10.1002/esp.1020

Tucker, G. E., & Bradley, D. N. (2010). Trouble with diffusion: Reassessing hillslope erosion laws with a particle-based model. *Journal of Geophysical Research: Earth Surface*, *115*(F1). doi: 10.1029/2009JF001264

Tucker, G. E., & Bras, R. L. (1998). Hillslope processes, drainage density, and landscape morphology. *Water Resources Research*, *34*(10), 2751–2764. doi: 10.1029/98WR01474

Tucker, G. E., & Bras, R. L. (2000). A stochastic approach to modeling the role of rainfall variability in drainage basin evolution. *Water Resources Research*, *36*(7), 1953–1964. doi: 10.1029/2000WR900065

Tucker, G. E., & Hancock, G. R. (2010). Modelling landscape evolution. *Earth Surface Processes and Landforms*, *35*(1), 28–50. doi: 10.1002/esp.1952

Tucker, G. E., & Slingerland, R. (1997). Drainage basin responses to climate change. *Water Resources Research*, *33*(8), 2031–2047. doi: 10.1029/97WR00409

Valters, D. (2016). Modelling geomorphic systems: Landscape evolution. In *Geomorphological Techniques.* United Kingdom: British Society for Geomorphology. doi: 10.13140/RG.2.1.1970.9047

Wagener, T., Sivapalan, M., Troch, P., & Woods, R. (2007). Catchment classification and hydrologic similarity. *Geography Compass*, *1*(4), 901–931. doi: 10.1111/j.1749-8198.2007.00039.x

Wang, D., & Wu, L. (2013). Similarity of climate control on base flow and perennial stream density in the Budyko framework. *Hydrology and Earth System Sciences*, *17*(1), 315–324. doi: 10.5194/hess-17-315-2013

Warix, S. R., Godsey, S. E., Lohse, K. A., & Hale, R. L. (2021). Influence of groundwater and topography on stream drying in semi-arid headwater streams. *Hydrological Processes*, *35*(5), e14185. doi: 10.1002/hyp.14185

Weeks, E. P. (2002). The Lisse Effect revisited. *Groundwater*, *40*(6), 652–656. doi: 10.1111/j.1745-6584.2002.tb02552.x

Whipple, K. X. (2001). Fluvial landscape response time: How plausible is steady-state denudation? *American Journal of Science*, *301*(4-5), 313–325. doi: 10.2475/ajs.301.4-5.313

Willgoose, G. (2005). Mathematical modeling of whole landscape evolution. *Annual Review of Earth and Planetary Sciences*, *33*, 443–459.

Wu, S., Zhao, J., Wang, H., & Sivapalan, M. (2021). Regional patterns and physical controls of streamflow generation across the conterminous United States. *Water Resources Research*, *57*(6), e2020WR028086. doi: 10.1029/2020WR028086

Yokoo, Y., Sivapalan, M., & Oki, T. (2008). Investigating the roles of climate seasonality and landscape characteristics on mean annual and monthly water balances. *Journal of Hydrology*, *357*(3), 255–269. doi: 10.1016/j.jhydrol.2008.05.010

Yoshida, T., & Troch, P. A. (2016). Coevolution of volcanic catchments in Japan. *Hydrology and Earth System Sciences*, *20*(3), 1133–1150. doi: 10.5194/hess-20-1133-2016

Zhang, Y., Slingerland, R., & Duffy, C. (2016). Fully-coupled hydrologic processes for modeling landscape evolution. *Environmental Modelling and Software*, *82*, 89–107. doi: 10.1016/j.envsoft.2016.04.014

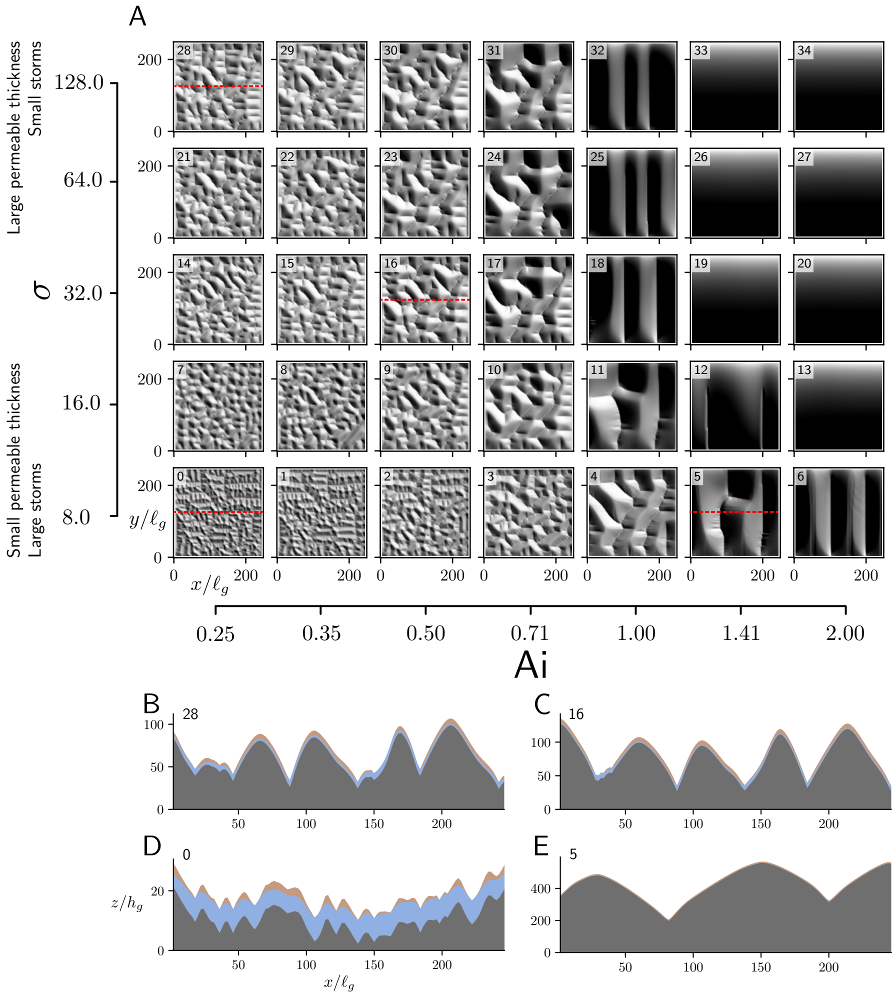

Figure 1. (A) Hillshades of modeled topography with varying aridity index Ai and water storage index σ, showing strong declines in dissection with increasing aridity, and a weaker positive relationship between dissection and σ. Here $\gamma = 4.0$, $\beta = 0.5$, $\rho = 0.03$, $\phi = 1.5$, $\alpha = 0.15$, $S_c = 0.5$, $\lambda = 250$, and $\delta = 2.0e-5$. The simulation numbers are in the upper left hand corner. Lower subplots (B–E) are lateral transects through topography along the red dashed lines for model runs corresponding to the small numbers on subplots in (A). Gray areas are impermeable bedrock, and brown areas are regolith, which is shown behind the mean aquifer thickness in light blue. Note differences in the vertical scale in B–E.

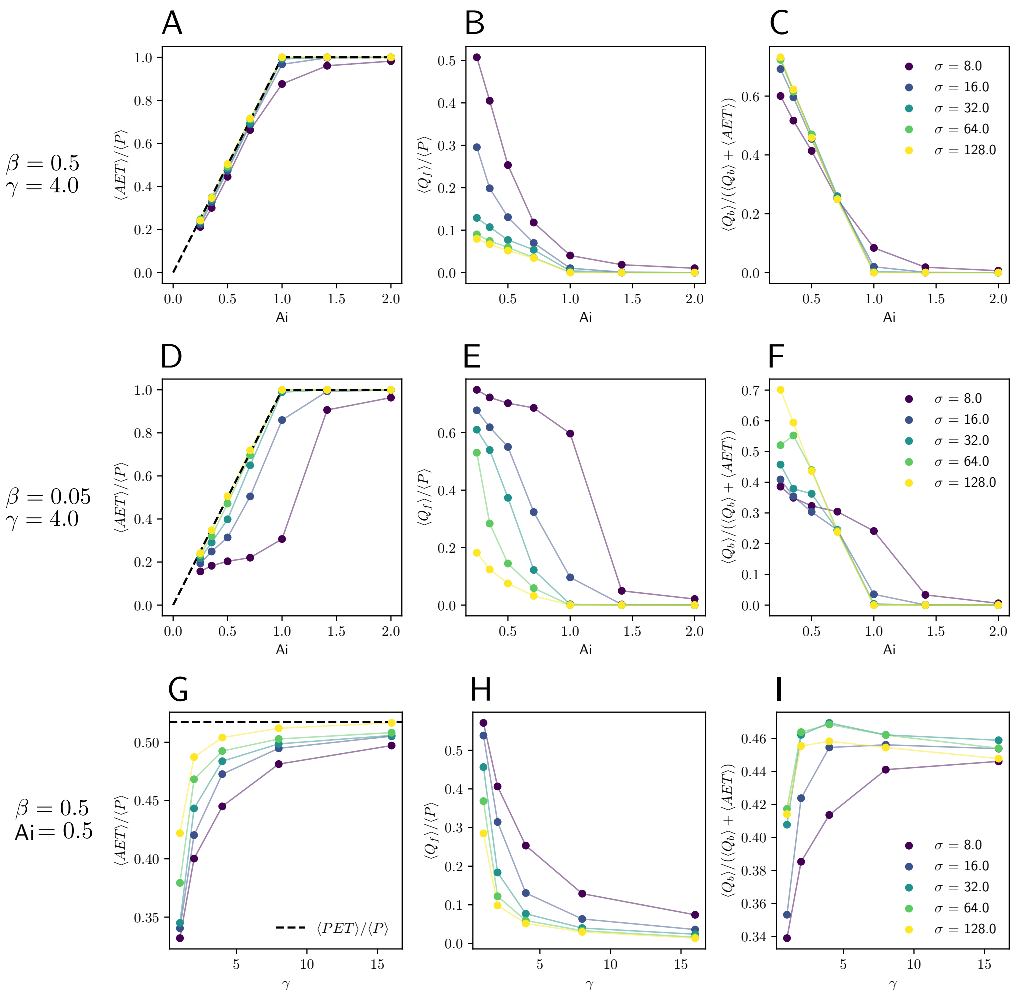

Figure 2. Water balance partitioning showing (A) Budyko-type plot, (B) the quickflow fraction of precipitation $\langle Q_f \rangle / \langle P \rangle$, and the baseflow fraction of storage, $\langle Q_b \rangle / (\langle Q_b \rangle + \langle AET \rangle)$ for the same simulations as in Figure 1. Storage is the amount of precipitation that does not become quickflow. (D–F) show the same partitioning as (A–C) above but for the model set with reduced aquifer relief scale $\beta = 0.05$ ($\gamma = 4.0$, $\rho = 0.03$, $\phi = 1.5$, $\alpha = 0.15$, $S_c = 0.5$, $\lambda = 250$, and $\delta = 2\mathrm{e}-4$). (G–I) show the same partitioning when the drainage capacity γ is varied while holding the aridity index constant at Ai $= 0.5$ ($\beta = 0.5$, $\rho = 0.03$, $\phi = 1.5$, $\alpha = 0.15$, $S_c = 0.5$, $\lambda = 250$, and $\delta = 2\mathrm{e}-5$). The dashed line in A–G shows the maximum ET fraction based on the energy or water limited condition. Subplot G is slightly different than (A) and (D) because all model runs have the same aridity, so the maximum value of $\langle PET \rangle / \langle P \rangle$ is a constant value.

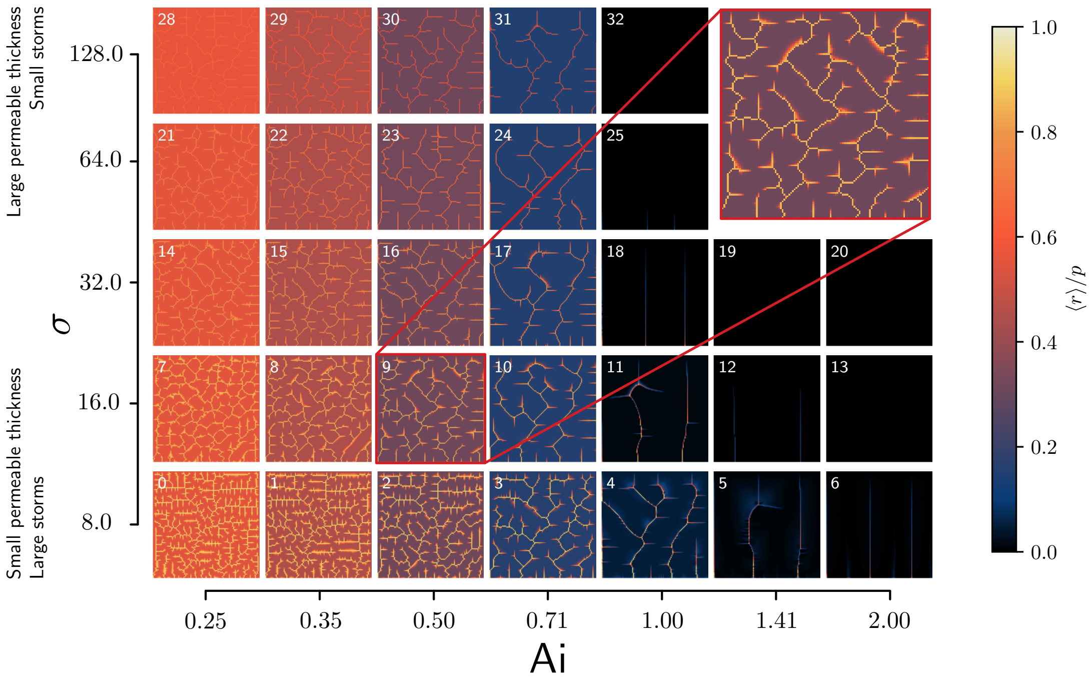

Figure 3. Average storm recharge rate $\langle r \rangle$ relative to the mean precipitation rate p for the same model runs that appear in Figure 1. Black areas indicate the absence of recharge. Hidden model runs (26, 27, 33, 34) did not produce any recharge. Results show expected decrease in recharge relative to precipitation with increasing aridity, although this effect is dampened when σ is small. The inset plot highlights that recharge is greatest in valley bottoms and convergent areas, revealing sensitivity to water table depth.

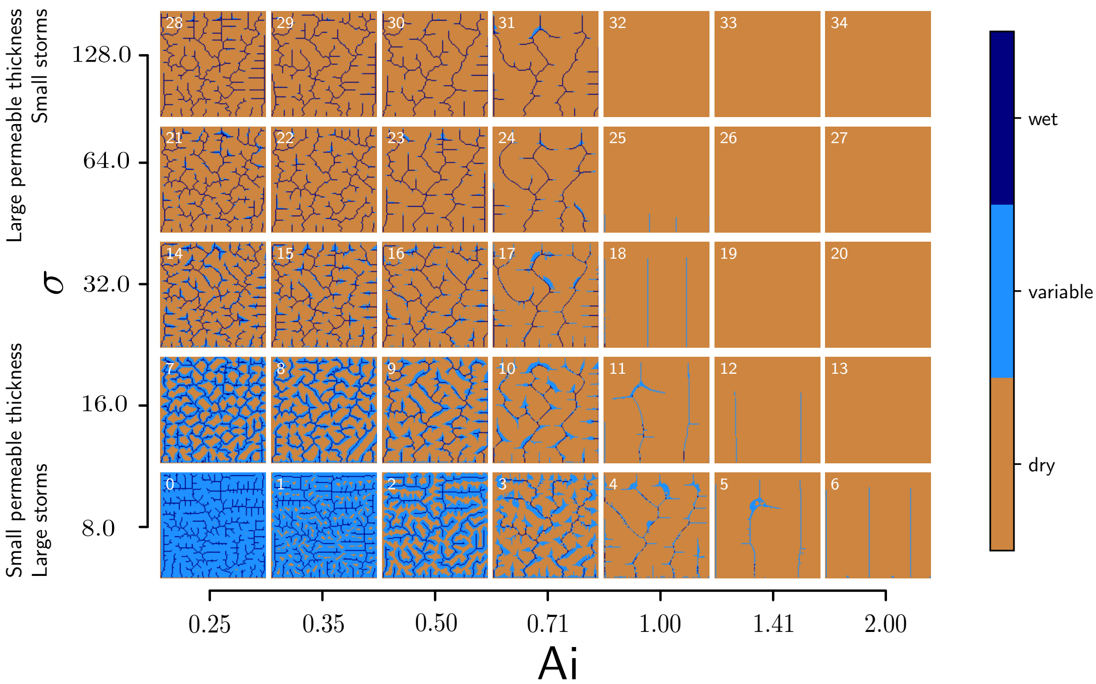

Figure 4. Classification of surface saturation for the same model set presented in Figure 1. Surface saturation is determined on the basis of time-variable water table proximity to the surface. Locations are classified as dry if they experience surface saturation at $<$ 5% of the ends of storms and interstorms, and are classified as wet if they are saturated at the end of $>$ 95% of storms and interstorms. Variably saturated areas are everywhere that does not meet either of these criteria. The results show the extent of variably saturated areas is greatest when σ is small. Non-permanent streams emerge in some cases as aridity increases, including cases like simulation 5, in which there are discontinuous zones of that are always wet.

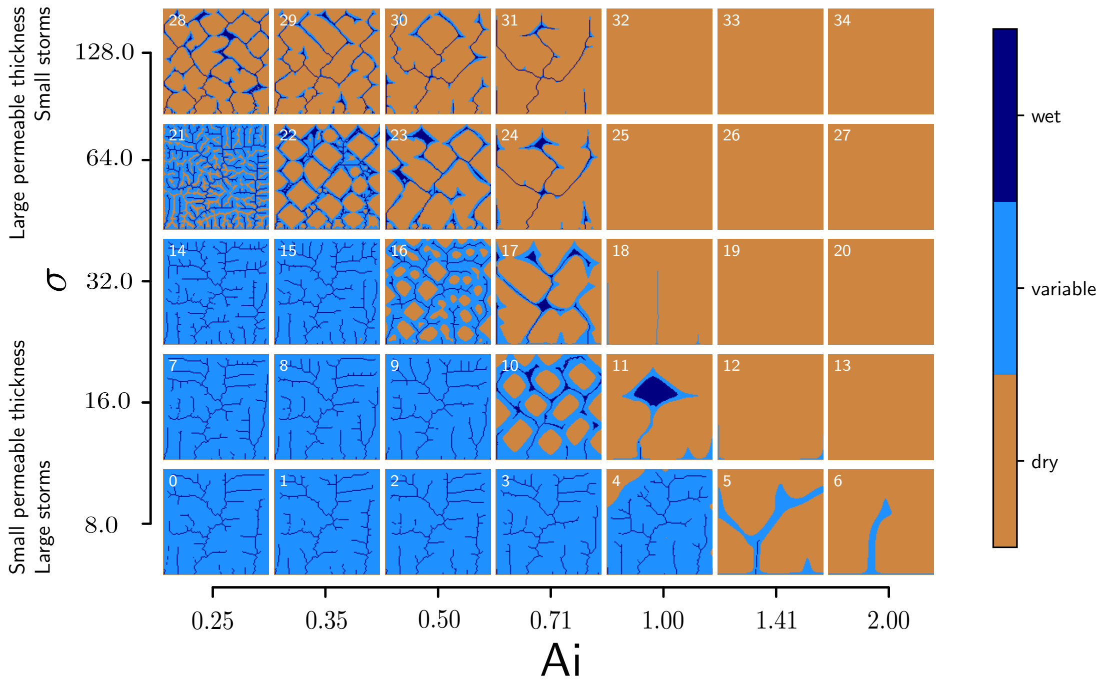

Figure 5. Classification of surface saturation for the model runs that appear in Supplemental Figure S5 and Figure 2(D–F), with $\beta = 0.05$. The classes are the same as in Figure 4. In contrast to the higher β case, here we see variably saturated areas from valleys to ridges in much of this parameter space. In the transition zone between widespread variable saturation and the zone without any channels, we see unusual channel forms, including nondendritic drainages (10, 16, 22, 23, 28), and extensive valley bottom wetland zones (11, 17, 23, 24, 28).

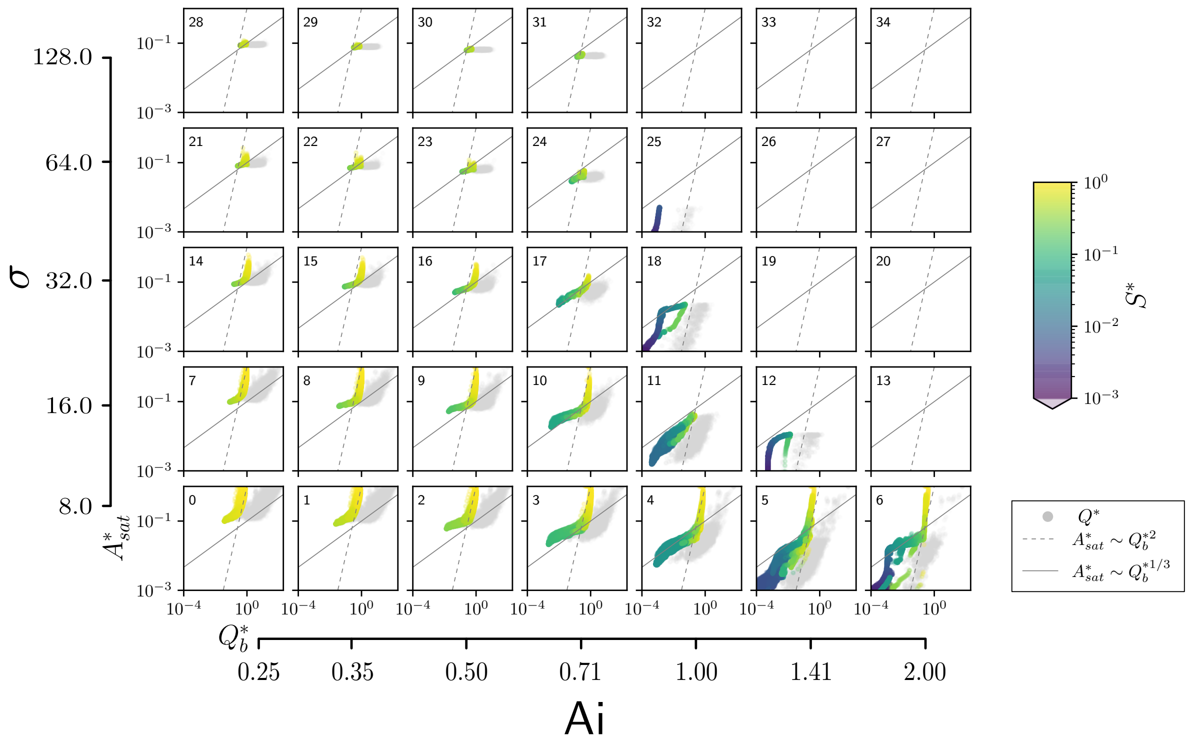

Figure 6. Dimensionless discharge Q^* and baseflow Q^*_b versus dimensionless saturated area A^*_{sat} for the same model runs that appear in Figure 1. A^*_{sat} is calculated using the same saturation criteria as all other figures, and has a maximum value of 1 when all cells are saturated. Each point depicts a model timestep, recorded at intervals corresponding to 1% of maximum timestep for groundwater model stability. Dimensionless discharge Q^* is depicted in gray. Dimensionless baseflow Q^*_b is colored by the dimensionless storage S^*, which varies from 1 when aquifer thickness is 0 everywhere to 1 when aquifer thickness is equal to permeable thickness everywhere. All quantities are totals of the model domain, and normalized by total area. We have left off subscripts for simplicity of notation. Dashed lines indicate the baseflow discharge equal to exfiltration at the mean recharge rate from the given saturated area. Data are absent for runs 19, 20, 26, 27, 33, and 34 because surface runoff was not produced.

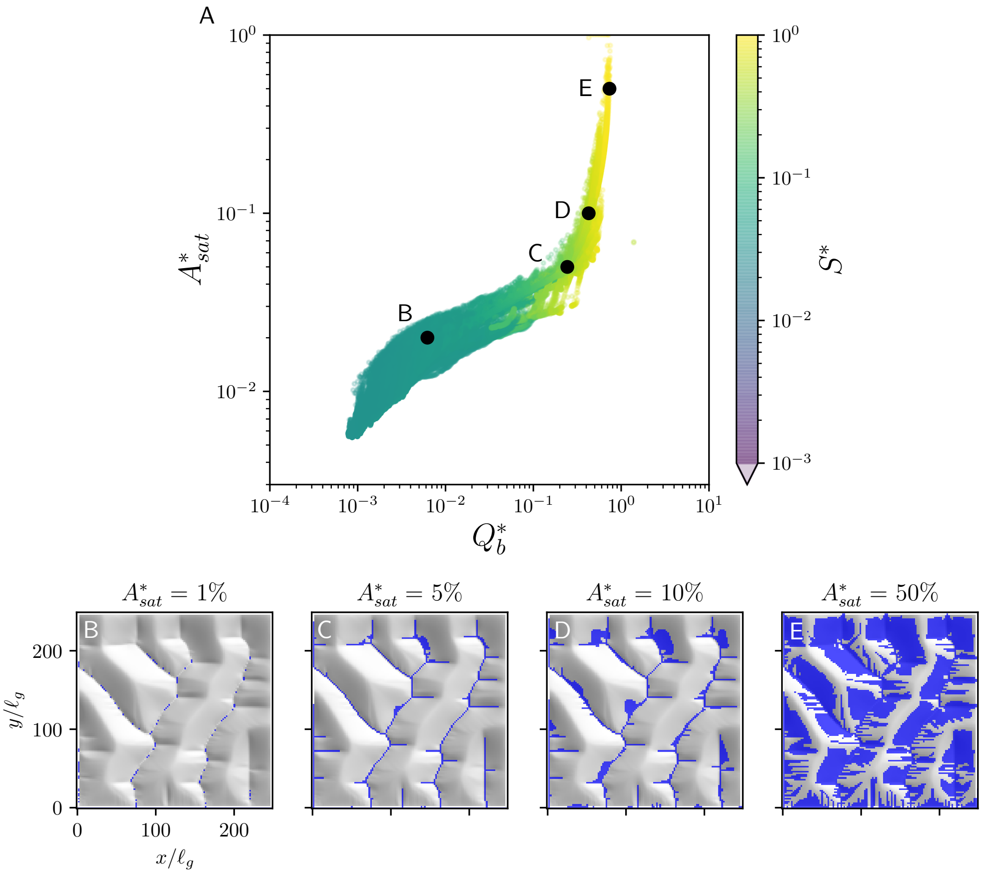

Figure 7. Detailed view of the dimensionless baseflow versus saturated area plot presented in Figure 6-4. Subplots (B–E) show the spatial distribution of saturation (in blue) at model timesteps corresponding to the locations (B–E) in panel (A). (B) shows saturation in second order channels. (C) sits right at the inflection point of the saturation-baseflow relationship, and corresponds to saturation just beginning to extend beyond the 1st order channel network. (D) shows more extensive saturation in unchanneled concave areas, while (E) shows widespread saturation on concave and planar slopes.

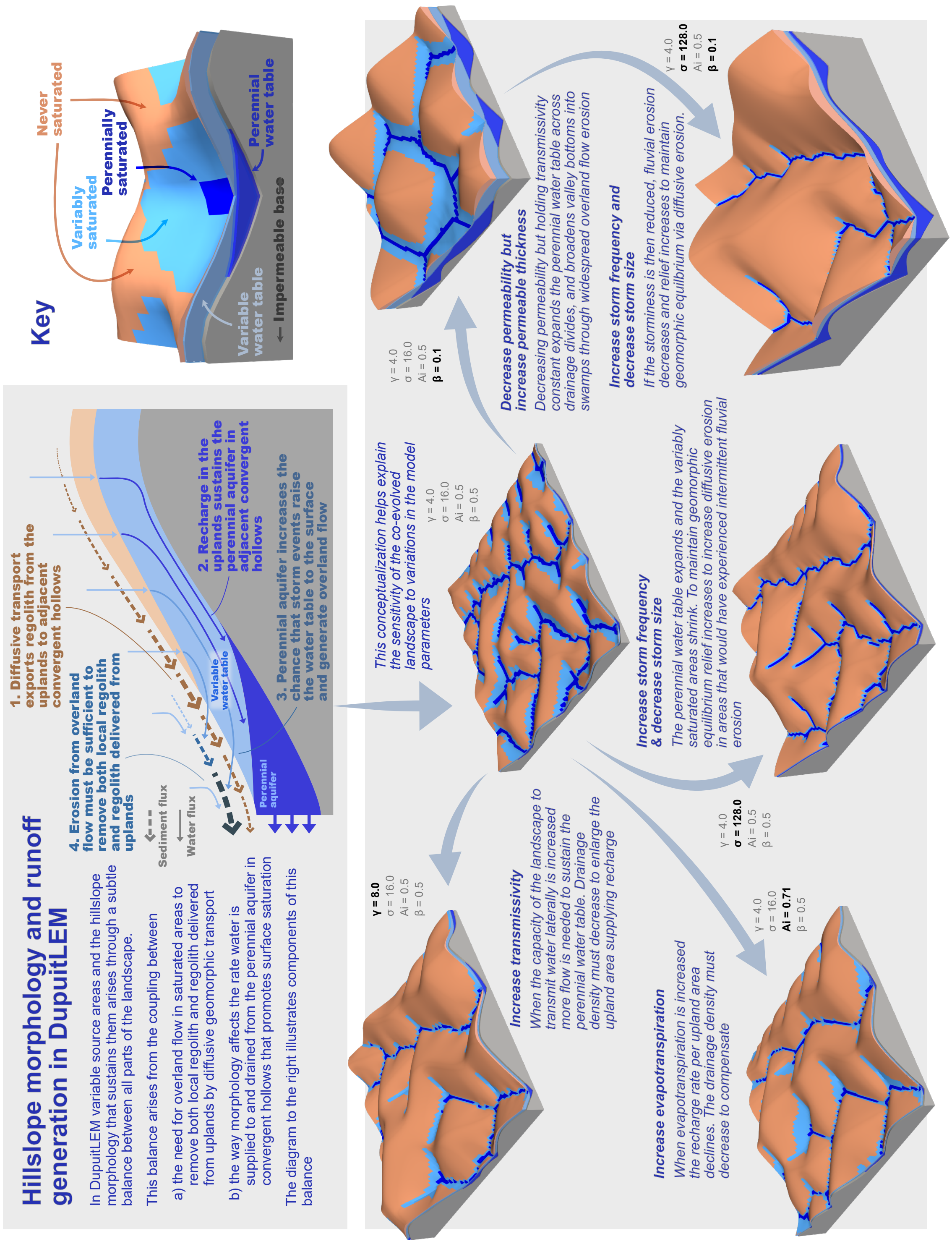

Figure 8. Conceptual figure illustrating how hillslope morphology and hydrology interact in DupuitLEM. This concept helps explain why varying the model parameters results in variations in drainage density and variable source area extent.

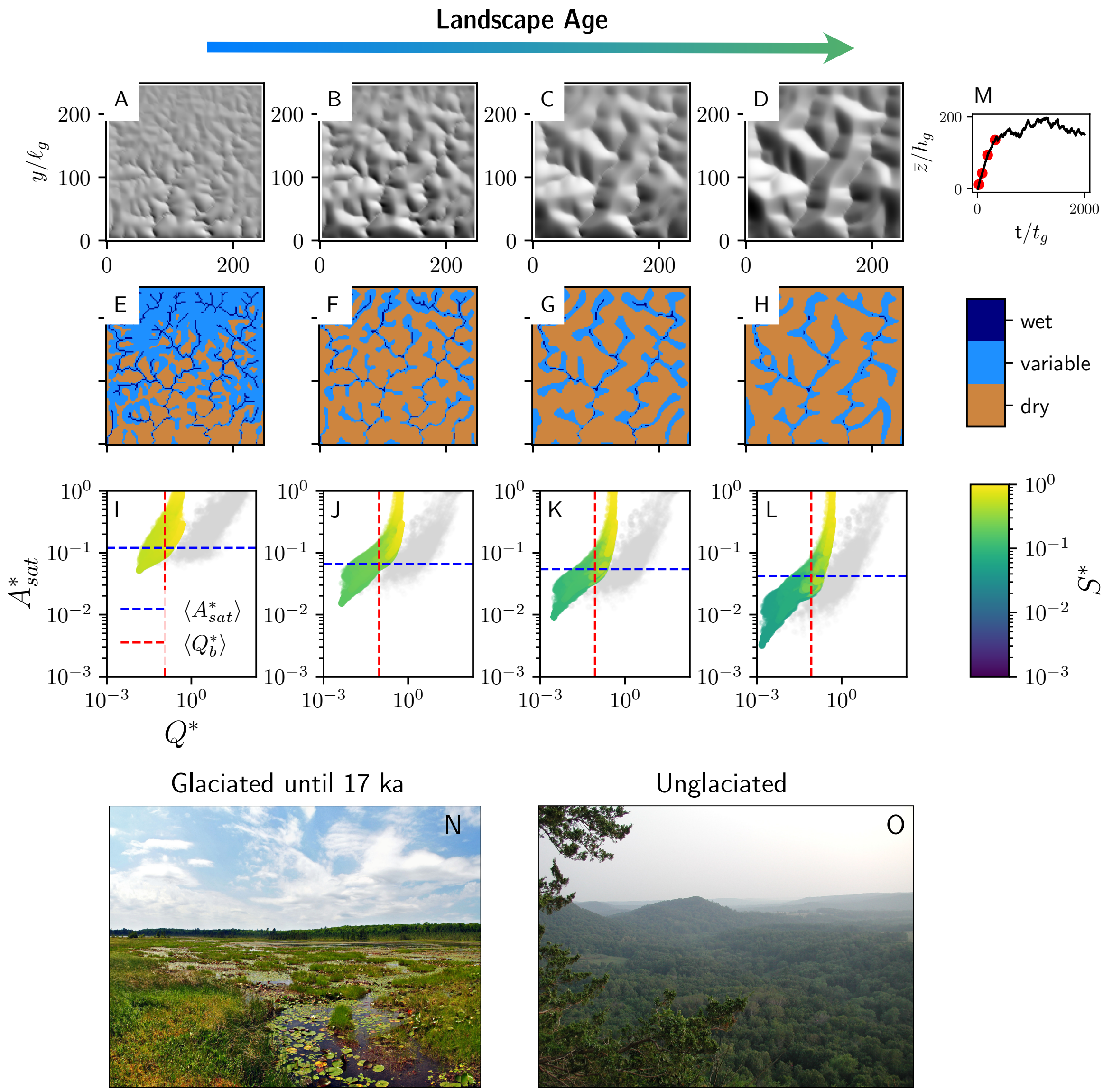

Figure 9. Comparison between results with increasing modelled age, as defined in the text above. (A–D) Hillshades of topography from a model run when mean elevation is 10, 30, 60, and 90% of the final value respectively (mean elevation is shown in (M)), showing decrease in dissection and steepening of slopes. (E–H) corresponding saturation classes showing transition from extensive wet drainage network and intermittently saturated zones to sparser drainage network with variably saturated channel adjacent zones. (I–L) corresponding dimensionless saturation baseflow plots, showing decrease in mean baseflow and mean saturated area, especially associated with decrease in frequency of the highest flows and highest saturated areas, and decreases in the lowest flows and saturated areas. (N) Recently glaciated Grandma Lake Wetlands in northern Wisconsin, USA, showing low relief and widespread saturation. CC-BY-SA Aarongunnar via WikiMedia Commons. (O) Unglaciated site in the Driftless Area of Wisconsin at Wildcat Mountain State Park showing forest cover and greater relief. CC-BY-SA Dandog77 via WikiMedia Commons

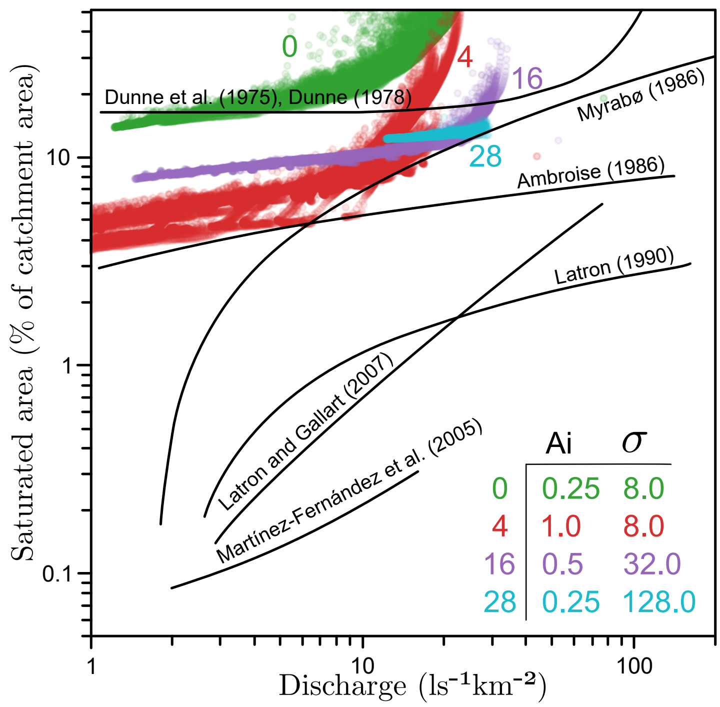

Figure 10. The relationship between saturated area and baseflow discharge for a several well-studied sites, reproduced from Latron and Gallart (2007), along with several of our model runs, 0, 4, 16, and 28, from Figure 6, which have been re-dimensionalized for the sake of obtaining baseflow discharge in the appropriate units. Parameters that vary are listed in the inset table. Our results are clipped to the extent originally presented in Latron and Gallart (2007).

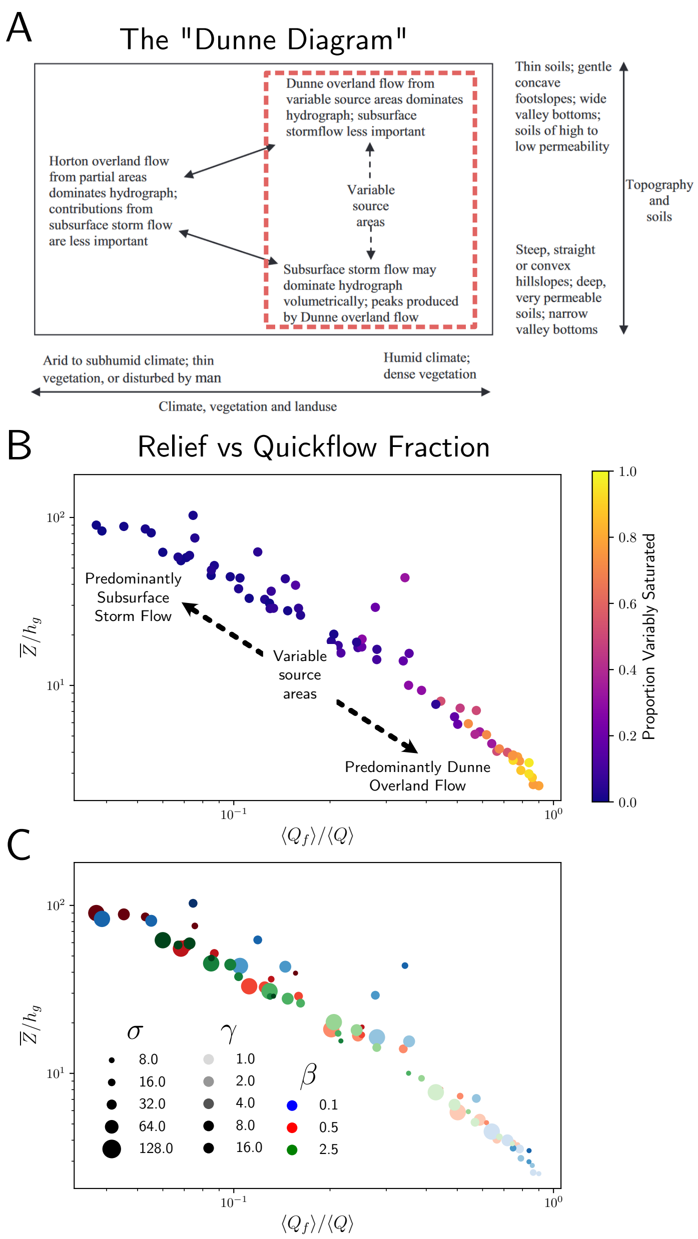

Figure 11. (A) The Dunne Diagram, reproduced from Li et al. (2014), highlighting the humid environments (red dashed box). (B) The relationship between the quickflow fraction and the mean relief, normalized by the characteristic height scale h_g for three sets of parameters, varying σ, γ, and β. All model runs are for humid climates (Ai $=$ 0.5). Other parameters are the same as those used previously ($\rho = 0.03$, $\phi = 1.5$, $\alpha = 0.15$, $\lambda = 250$, $S_c = 0.5$, δ varies from 1e $-$ 4 to 4e $-$ 6 with β). Colors indicate the fraction of the landscape classified as variably saturated under the definition used in previous sections. (C) The same plot as (B), but colored to show the particular combination of the three parameters varied. Dot size scales with σ, color lightness with γ, and base color with β.

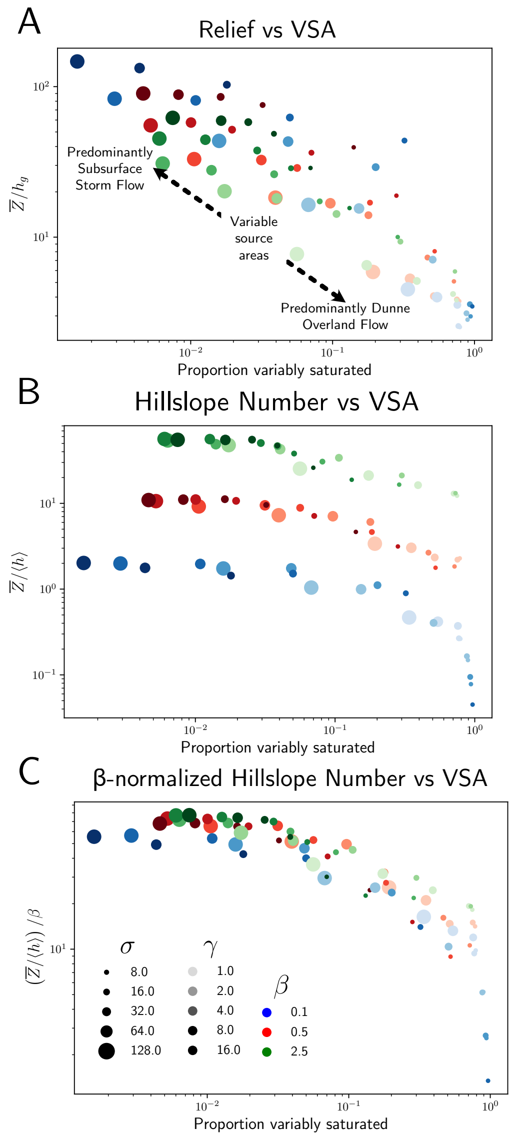

Figure 12. (A) variation in dimensionless relief $\overline{Z}/h_g$ versus the variably saturated area (VSA) as a fraction of the total area based on the definition introduced in Section 5.3 using the same model runs shown in Figure 11, showing substantially more scatter than Figure 11A. (B) The hillslope number $\overline{Z}/\langle h \rangle$ plotted against the proportion variably saturated, showing parallel but distinct relationships for each value of β. (C) Normalizing the vertical axis in (B) by β collapses all the relationships, and shows that the β-normalized hillslope number is maximized when the fraction of the watershed that is variably saturated is small, and minimized when the variably saturated fraction is large.

Catchment coevolution and the geomorphic origins of variable source area hydrology

David G. Litwin[1], Gregory E. Tucker[2,3], Katherine R. Barnhart[4], Ciaran J. Harman[1,5]

[1]Department of Environmental Health and Engineering, Johns Hopkins University, Baltimore, MD, USA
[2]Cooperative Institute for Research in Environmental Sciences (CIRES), University of Colorado, Boulder, CO, USA
[3]Department of Geological Sciences, University of Colorado, Boulder, CO, USA
[4]U.S. Geological Survey, Geologic Hazards Science Center, Golden, CO, USA
[5]Department of Earth and Planetary Science, Johns Hopkins University, Baltimore, MD, USA

Key Points:

- A landscape evolution model with runoff from shallow groundwater was used to explore how hydrological function coevolves with topography.
- Landscapes evolve toward equilibrium where unchanneled uplands supply just enough water for persistence of lowland saturated areas.
- We found local relief decreases log-linearly with the fraction of runoff generated by saturation excess, in agreement with field studies.

Corresponding author: Ciaran J. Harman, charman1@jhu.edu

Abstract

Features of landscape morphology—including slope, curvature, and drainage dissection—are important controls on runoff generation in upland landscapes. Over long timescales, runoff plays an essential role in shaping these same features through surface erosion. This feedback between erosion and runoff generation suggests that modeling long-term landscape evolution together with dynamic runoff generation could provide insight into hydrological function. Here we examine the emergence of variable source area runoff generation in a new coupled hydro-geomorphic model that accounts for water balance partitioning between surface flow, subsurface flow, and evapotranspiration as landscapes evolve over millions of years. We derive a minimal set of dimensionless numbers that provide insight into how hydrologic and geomorphic parameters together affect landscapes. We find an inverse relationship between the dimensionless local relief and the fraction of the landscape that produces saturation excess overland flow, in agreement with the synthesis described in the "Dunne Diagram." Furthermore, we find an inverse, nonlinear relationship between the Hillslope number, which describes topographic relief relative to aquifer thickness, and the proportion of the landscape that variably saturated. Certain parameter combinations produce features wide valley bottom wetlands and nondendritic, diamond-shaped drainage networks, which cannot be produced by simple landscape evolution models alone. With these results, we demonstrate the power of coupled hydrogeomorphic models for generating new insights into hydrological processes, and also suggest that subsurface hydrology may be integral for modeling aspects of long-term landscape evolution.

Plain Language Summary

The topography of landscapes affects how much and where precipitation becomes runoff, while runoff itself plays a role in shaping topography over long times through erosion. Some landscapes may exist exist in an equilibrium state, where the landscape is ideally shaped to carry the amount of runoff produced. Understanding this equilibrium may provide insights into why landscapes have different hydrological styles; for example, some landscapes contribute runoff to streams primarily through the ground, whereas others develop saturated areas during storms that generate surface runoff when rain falls on them. Here we use a new model to simulate dynamic runoff as we expect it to occur in humid temperate environments while also using this runoff to evolve topography. The results show that landscapes that already have a tendency to produce variably saturated areas because they are poor at storing water or transmitting it laterally through the ground also evolve to have lower relief, which helps variably saturated areas to persist. The results highlight the role that landscape history plays in the hydrological processes observed today and can be used to better understand the role of subsurface hydrological processes in long-term landscape evolution.

1 Introduction

1.1 Motivation

Landscape geomorphology is inextricably connected to runoff generation. Topographic slope is often a strong predictor of hydraulic gradient (Haitjema & Mitchell-Bruker, 2005), whereas topographic curvature affects how water is concentrated or dispersed as it moves downslope (Lapides et al., 2020; Prancevic & Kirchner, 2019; Troch et al., 2003), all of which affects the likelihood of surface runoff. Subsurface porosity and permeability further affect these quantities, as they affect how effectively the subsurface can infiltrate water and transmit it laterally toward streams (Horton, 1933; O'Loughlin, 1981). At the same time, runoff can alter geomorphic properties of landscapes because it drives erosion and ultimately the incision of river channels, which then affect the morphology of adjacent hillslopes (Callahan et al., 2019; Dietrich et al., 2003; Roering et al., 2001).

Landscape evolution models (LEMs) have been essential tools for understanding topographic change over long timescales (e.g., reviews by Bishop, 2007; Chen et al., 2014; Pelletier, 2013; Tucker & Hancock, 2010; Valters, 2016; Willgoose, 2005) and thus are expected to be useful for understanding relationships between topography and runoff. However, landscape evolution simulations usually simplify hydrology to an extent that feedbacks between landscape evolution and subsurface flow dynamics cannot be examined. Recent studies have made progress in representing hydrologic processes more explicitly in LEMs, and show that drainage density scales linearly (Luijendijk, 2022) or nonlinearly (Litwin et al., 2021) with transmissivity when runoff is generated by saturation excess overland flow. Although these studies broke new ground by revealing how runoff generation affects topography, it is still unclear how this coevolution affects hydrological function. Understanding how landscape history affects current hydrological function has the potential to transform how we understand Earth's critical zone, and how we make hydrological predictions (Harman & Troch, 2014; Singha & Navarre-Sitchler, 2022; Troch et al., 2015).

Hydrological function describes the quantity, timing, and location of the storage and release of water from watersheds. Relationships between various stores and fluxes are used to describe a watershed's hydrological functioning. One of the most fundamental is the catchment water balance, which describes the long-term partitioning of water into storage, evapotranspiration, runoff, and deep recharge. On shorter timescales, storage-discharge relationships have been essential for understanding rainfall-runoff response and catchment recession (McMillan, 2020). The relationship between saturated area or active stream network length and discharge has illuminated geologic and topographic and climatic controls on runoff generation (Jensen et al., 2017; Latron & Gallart, 2007; Prancevic & Kirchner, 2019; Warix et al., 2021). Although these attributes of hydrological function are important in their own right (e.g., habitat extent and connectivity provided by the flowing stream network (Campbell Grant et al., 2007)), when taken together and compared across many sites, mappings can be developed that relate hydrological function to catchment attributes. These can improve hydrological predictions where historical datasets are short or not available (Wagener et al., 2007). Understanding how hydrological function coevolves with catchment attributes may provide a deeper understanding of these mappings, including why they exist at all.

1.2 Runoff generation and saturated areas

Dunne (1978) provided a succinct framework for understanding the relationship between climate, landscape morphology, and runoff generation mechanisms. In humid climates with minimal anthropogenic disturbance, thick soils in steep landscapes produce primarily subsurface variable source areas (Hewlett & Hibbert, 1967), where a saturated wedge may form in the subsurface near the toe of the hillslope and expand up the hillslope in response to recharge. In contrast, humid environments with shallow soils and more gentle topography tend to produce saturation excess overland flow (Dunne & Black, 1970), where subsurface lateral flow capacity is exceeded, producing saturated areas where groundwater may exfiltrate and become surface runoff along with precipitation on saturated areas. These relationships between topographic properties and runoff generation mechanisms were recently re-examined by Wu et al. (2021), who used a larger dataset than Dunne (1978) and identified characteristic features of different runoff generation mechanisms in rainfall-runoff relationships. While the inclusion of more diverse environmental settings required further subdivision of runoff generation mechanisms and controls, the fundamental relationships identified by Dunne (1978) still emerged.

However, research so far has not provided sufficient explanation for why certain combinations of topographic properties and runoff generation mechanisms appear (Li et al., 2014). This question is not particularly new. As distributed hydrological modeling of runoff generation became possible, Freeze (1980) noted:

> The simulations carried out in this study have placed the author in some awe of the delicate hydrologic balance on a hillslope. If one fixes the mean hydraulic conductivity of a hillslope, then there is only a very narrow range of topographic slopes that can lead to runoff generated by the Dunne mechanism. If one fixes the topographic slope of a hillslope, then there is only a very narrow range of hydraulic conductivities that will lead to a water table that is high enough to allow the Dunne mechanism to be operative in a given climatic regime. The fact that the Dunne mechanism is so common in nature in spite of these theoretical limitations on its occurrence infers a very close relationship between climate, hydraulic conductivity, and the development of geomorphic landforms.

What Freeze (1980) observed in simulations indicates that some sort of catchment coevolution (Troch et al., 2015) might be needed to explain a tendency toward saturation excess variable source area runoff generation (the "Dunne mechanism"). The literature exploring the evolution of climate–morphology–runoff generation relationships is minimal. Here our goal is to provide a broad picture of what kinds of landscapes and hydrological behavior emerge as we allow climatic, hydrologic, and geologic properties to vary, assuming that runoff generation is driven by saturation excess from shallow groundwater flow and subsurface stormflow. We provide a synthesis of some of our results in the context of relationships identified in field data, including those of Dunne (1978), which indicate that at least certain features of that relationship are emergent products of catchment coevolution.

1.3 Climate stochasticity in landscape evolution models

Precipitation variability has long been recognized as an important factor in landscape evolution. Ijjász-Vásquez et al. (1992) considered steady-state subsurface flow and an exponential distribution of rainfall depths, and showed that the statistical distribution of resulting erosion rates effectively smoothed hillslope-valley transitions. Tucker and Bras (1998) found similar smoothing of hillslope-valley transitions with a comparable model that used a steady state partitioning of flow between surface and subsurface for storm events drawn from exponential distributions of depth, duration, and interstorm duration. Similar approaches with stochastic precipitation but steady-state hydrological models are still widely in use (e.g., Barnhart et al., 2018). However, these models are limited in that antecedent conditions are not considered; the runoff and sediment transport rate during each event is independent from previous events.

Other studies have taken different approaches to capture some of the effects of memory and event sequence on runoff and erosion. Lague et al. (2005) examined the effects of discharge variability on channel long profile evolution by using a power law distribution of runoff rates, forgoing an explicit model of the processes that convert rainfall to runoff. Deal et al. (2018) further advanced understanding of how runoff distributions affect channel long profiles using the stochastic hydrological model developed by Botter et al. (2007) to generate runoff from a coupled, spatially lumped soil moisture and linear reservoir groundwater model. This approach accounts for the important effects of antecedent water storage and evapotranspiration on runoff generation, which ultimately affects fluvial erosion (Rossi et al., 2016). Because of these features, the model developed by Deal et al. (2018) shows promise for understanding how climate translates into erosion events and long-term evolution. However, models of channel long profile evolution cannot quantify spatially distributed hydrological features of interest, such as variably saturated areas. Moreover, it remains unclear exactly how the hydrological parameters (e.g., the reservoir coefficient, or reservoir size) needed for the model developed by Deal et al. (2018) are best linked to the evolving channel profile or surrounding hillslopes.

Although a few previous studies have used LEMs that resolve spatially distributed hydrological features, none have investigated the hydrological function that emerges at geomorphic dynamic equilibrium. Huang and Niemann (2006) used a coupled groundwater-LEM to examine how topographic evolution changed runoff generation at a well studied site, but evolved the landscape for far less time than needed to achieve dynamic equilibrium. Huang and Niemann (2008) investigated long-term evolution with a coupled groundwater-LEM, but examined the sensitivity of modeled topography to hydrologic parameters by prescribing changes onto the slope-area relationship rather than directly simulating the evolution to dynamic equilibrium, which makes evaluating the role of coevolution between runoff generation and topography challenging. Lastly, Zhang et al. (2016) presented a highly detailed coupled hydrological and landscape evolution model, but the model has only been used as a proof of concept.

1.4 Approach

Here, we focus on the coevolution of topography and runoff generated by groundwater return flow and precipitation on saturated areas. To do this, we use the streampower-diffusion LEM called DupuitLEM that was developed by Litwin et al. (2021), in which runoff produces the shear stress for detachment limited erosion, and topography sets the boundary conditions for the groundwater system. To capture time-varying runoff generation, we include stochastic storm generation and a simplified representation of vadose zone dynamics. We evolve the coupled model toward geomorphic dynamic equilibrium where the denudation rate is approximately equal to the uplift rate. At this point the hydrological function of the landscape is in some sense in equilibrium with topography– what exactly this equilibrium is and how it emerges are central to our results and discussion.

Hydrologic function of emergent landscapes likely depends on geomorphic, hydraulic, and climatic parameters in the model. However, this parameter space is large, and combinations of parameters do not necessarily result in unique model outputs. Dimensional analysis of the model allows us to approach both of these problems. We use a nondimensionalization approach to produce a minimal set of dimensionless groups that both uniquely determine model output and provide insight into the competing processes that affect evolved morphology and hydrologic function. We begin with the nondimensionalization developed by Litwin et al. (2021), and expand it to include the effects of the vadose zone and time-varying climatic forcing.

Still, this dimensionless parameter space is too large for a comprehensive investigation of all possibilities. Without a full investigation of the parameter space, we can still answer key questions about how hydrological function coevolves with topography. We do this by focusing on how dimensionless groups that express climate and subsurface hydraulics affect (1) topography and drainage dissection, (2) water balance and flux partitioning, (3) spatial patterns of hydrologic fluxes and saturation, and (4) temporal relationships between saturated area, discharge, and storage. Based on the results, we present a perceptual model of the emergence and persistence of variable source area hydrology and show that the relationships between geomorphology and runoff generation in humid landscapes that were identified by (Dunne, 1978) can be obtained through coevolution. Finally we discuss the potential for using landscape history to understand present hydrological function.

2 Model Description

2.1 Topographic evolution

The LEM used here considers the evolution of topographic elevation $z(x, y, t)$ by water erosion $E_f(x, y, t)$, erosion resulting from the divergence of hillslope regolith transport $E_h(x, y, t)$, and uplift or baselevel change U.

$$\frac{\partial z}{\partial t} = -E_f - E_h + U \tag{1}$$

Litwin et al. (2021) derived the water erosion term from excess shear stress, arriving at a form that is similar to the detachment-limited streampower law, but using the area per contour width a instead of upslope area A. Bonetti et al. (2018) define $a(x, y)$ as the scalar field satisfying $-\nabla \cdot \left(a \frac{\nabla z}{|\nabla z|} \right) = 1$, which is an elegant analytical definition of the concept usually defined as $a = A/v_0$ in the limit of small contour width v_0. The erosion law also scales linearly with the dimensionless discharge $Q^* = Q/(pA)$, where Q is the volumetric discharge and p is the mean precipitation rate, which we derived from the hydrological model as discussed below. The rate of water erosion is:

$$E_f = K\sqrt{v_0}Q^*\sqrt{a}|\nabla z| - E_0 \tag{2}$$

where K is the streampower erosion coefficient, and E_0 is a threshold below which no water erosion occurs. Although erosion thresholds can have important effects on morphology (e.g., Tucker, 2004), here we only present results for $E_0 = 0$, as we found the threshold to have little effect on the hydrological behavior of interest in this study.

The term E_h describes gravity-driven movement of sediment via processes such as frost heave, animal burrowing, and tree throw. A simple formulation for E_h begins by assuming that the sediment flux is proportional to the local slope gradient, $q_h \sim \nabla z$, and the resulting elevation change is the divergence of this flux, $E_h \sim \nabla^2 z$. This is the linear hillslope diffusion law, which was used in Litwin et al. (2021). This assumption produces unrealistically steep toe slopes ($|\nabla z| > 1$) as hillslopes become long. Landscapes with high relief and long hillslopes generally have a form better described by nonlinear sediment flux laws, where flux increases super-linearly with slope. Near ridges and when relief is low, the law produces near-parabolic topography (like the linear diffusion law), but as the slope gradient increases it produces increasingly planar hillslopes. This replicates a shift from short-range transport to longer-distance transport processes such as dry ravel and shallow mass failures (e.g., Doane et al., 2018; Gabet, 2003; Roering et al., 1999; Tucker & Bradley, 2010). Data compiled by Godard and Tucker (2021) showed that most documented field case studies of hillslope morphology, transport efficiency, and erosion rate fall within the nonlinear transport regime. We chose the hillslope transport model described by Ganti et al. (2012), which is a Taylor expansion of the critical slope model

$$q_h = \frac{D\nabla z}{1 - (|\nabla z|/S_c)^2} \tag{3}$$

used by Andrews and Bucknam (1987) and Roering et al. (1999), but is more computationally tractable for landscape evolution simulations. The rate of elevation change due to hillslope erosion is

$$E_h = \nabla \cdot q_h = D\nabla \cdot \left(\nabla z \left(1 + \left(\frac{|\nabla z|}{S_c} \right)^2 \right) \right) \tag{4}$$

where D is the transport coefficient and S_c is a critical slope. This expression represents the first two terms of the Taylor expansion, which Ganti et al. (2012) showed to be a close approximation of the original partial differential equation.

Combining the water- and gravity-driven erosion terms with a constant rate of base-level change U, we arrive at the governing equations of the LEM:

$$\frac{\partial z}{\partial t} = -K\sqrt{v_0}\langle Q^*\rangle\sqrt{a}|\nabla z| + D\nabla\cdot\left(\nabla z\left(1+(|\nabla z|/S_c)^2\right)\right) + U \tag{5}$$

$$-\nabla\cdot\left(a\frac{\nabla z}{|\nabla z|}\right) = 1 \tag{6}$$

where the angled brackets $\langle\cdot\rangle$ indicate the time-averaged value of the quantity.

2.2 Subsurface model

As in Litwin et al. (2021), we consider only a homogeneous, surface-parallel layer of permeable material with thickness b above impermeable bedrock. We will refer to this as the 'permeable thickness' as we do not distinguish between mobile regolith and weathered or fractured bedrock. Although deeper groundwater flow can be important for runoff generation, here the permeable thickness sets the lower boundary for groundwater circulation. We will sometimes refer to 'regolith' when discussing hillslope sediment transport, although ultimately the geomorphic model is agnostic to the composition of the subsurface. That is, we assume there is always enough regolith to meet the slope-based hillslope flux law. Lastly, the term 'soil' is used when referencing or drawing comparison with field studies that use this term, in which case the analogous term in our model is permeable thickness.

How exactly the subsurface of real landscapes evolves to keep pace with surface evolution is an active subject of research that so far has no consensus (Riebe et al., 2017). Surface-parallel permeability structure is sometimes (but not always) observed in the field St. Clair et al. (2015), and also emerges at geomorphic steady state with the widely used exponential production model (e.g., Rosenbloom & Anderson, 1994; Tucker & Slingerland, 1997). Fixing the permeable thickness rather than tracking its evolution does have limitations, as discussed in Section 6.4, but ultimately we decided to keep the subsurface representation simple to focus on the dynamics of topographic and hydrologic evolution.

2.3 Hydroclimatological model

Given the long timescales of landscape evolution relative to runoff generation, it was necessary to make compromises between process representation and computational efficiency. Our goal was to develop a minimally complex model that captured the emergence of catchment and hillslope scale hydrological function (sensu Wagener et al., 2007) including water balance partitioning, and the presence of surface and subsurface variable source areas. We therefore aimed to construct a model that incorporated the following elements:

- rainfall, and therefore recharge, varies in time,
- rainfall is partitioned between quickflow and storage,
- storage is partitioned between ET and baseflow,
- ET is limited by energy in humid climates, and by water availability in dry climates.

To address the first element, we generated stochastic storm depth d_s, duration t_r, and interstorm duration t_b using exponential distributions, following Eagleson (1978), and many papers in the hydrology (e.g., Botter et al., 2007; Rodriguez-Iturbe et al., 1999)) and landscape evolution literature (e.g., Barnhart et al., 2018; Tucker & Bras, 2000)). Previously we introduced the mean precipitation rate, p, which is related to the above parameters as $p = \langle d_s\rangle/(\langle t_r\rangle + \langle t_b\rangle)$. The distributions for storm depth, duration, and interstorm duration are:

$$
\begin{aligned}
f(d_s) =& \frac{1}{\langle d_s \rangle} \exp\left(- \frac{d_s}{\langle d_s \rangle} \right) & (7)\\
f(t_r) =& \frac{1}{\langle t_r \rangle} \exp\left(- \frac{t_r}{\langle t_r \rangle} \right) & (8)\\
f(t_b) =& \frac{1}{\langle t_b \rangle} \exp\left(- \frac{t_b}{\langle t_b \rangle} \right). & (9)\\
& & (10)
\end{aligned}
$$

To address elements 2 and 3, we needed to account for storage in the unsaturated zone as well as the saturated zone. A thorough treatment of coupled saturated-unsaturated zone dynamics would be computationally prohibitive for landscape evolution simulations. We opted instead for a one-way coupling between a simple unsaturated zone model and the Dupuit-Forcheimer groundwater model, which is capable of capturing important features.

Schenk (2008) presented a simple model (called here the Schenk model) for vadose zone dynamics in a 1-dimensional profile that serves our purpose well. The model is based on the assumption that plants extract water from the shallowest depth where water is available, and use all available water at that depth before extracting water from deeper in the profile. Conversely, precipitation fills available storage at the ground surface first, and displaces water already present deeper into the profile. Schenk (2008) showed that the distribution of depths from which water is extracted in this model mimics the plant rooting depth distributions in a wide range of climates. This is useful to our study because the depths of root water uptake emerge as a result of the climate and subsurface hydraulic properties selected rather than requiring an additional parameter.

We took a spatially-integrated approach to the unsaturated zone state, modeling unsaturated zone storage with the Schenk model, from which we derived spatially distributed estimates of groundwater recharge based on the water table depth. The Schenk model can be written in cumulative form using the coordinate d, depth below the ground surface. The model tracks the volume (per unit area) of storage S_d above depth d, which evolves in time according to:

$$S_d(d, t + \Delta t) - S_d(d, t) = \min\left(dn_a - S_d(d, t), i(t)\Delta t\right) - \min\left(S_d(d, t), pet(t)\Delta t\right) \tag{11}$$

where t is the current time, Δt is the timestep, n_a is the plant-available water content (equal to the field capacity minus the water content below which plants will prefer to use water from deeper depths), $i(t)$ is the storm intensity (equal to $d_s/\Delta t$ during storms, and zero otherwise), and $pet(t)$ is the potential evapotranspiration (ET) rate (equal to a constant rate pet during interstorms and zero otherwise). Equation (11) states that the change in vadose water stored above depth d over the time interval Δt is the lesser of the available vadose storage above d and the depth of rainfall during the interval, minus the lesser of the water in vadose storage above d and the evapotranspiration during the interval. We assumed that the recharge R_d received by a water table at depth d is the amount of water that has infiltrated below d in the vadose profile:

$$R_d(d, t) = i(t)\Delta t - \min\left(dn_a - S_d(d, t), i(t)\Delta t\right) \tag{12}$$

from which we arrive at the recharge rate:

$$r(x, y, t) = \frac{R_d(b - h(x, y, t), t)}{\Delta t} \tag{13}$$

where the depth to the water table is $b-h(x, y, t)$, the permeable thickness minus the aquifer thickness. We have set the maximum profile depth equal to the permeable thickness b, such that $d \leq b$, which ensured continuity between saturated and unsaturated flow models. Note that the recharge rate in Equation (13) is equal to the precipitation rate i when the water table is at the surface ($b-h=0$). The groundwater model discussed in Section 2.4 then determines how this recharge will be partitioned between overland flow and saturated subsurface flow. A full sample calculation of the Schenk model is shown in Supplemental Figure S2.

The Schenk model was run such that each timestep was either an entire storm or an entire interstorm period. Any recharge generated was assumed to arrive at the groundwater table at a steady rate over the storm period. During interstorm periods, the recharge rate is assumed to be zero (even if the water table has risen farther into the unsaturated zone), and the actual evapotranspiration will always equal the potential evapotranspiration rate when water in vadose storage is available. We calculate total actual evapotranspiration by subtracting the total recharge from the total precipitation, assuming all precipitation that did not become recharge to the saturated zone was transpired. We explored the possibility of allowing for root water uptake from the saturated zone; however, we found that conservation of mass would only be possible if the unsaturated zone state was tracked uniquely at each location where we track water table elevation, defeating the purpose of choosing this model for its computational efficiency. In tests we found saturated zone root water uptake would be a relatively small component of the water balance in much of the parameter space (although we cannot rule out its importance in some edge cases). We leave further exploration of this for future work.

2.4 Groundwater flow and runoff generation

Runoff is generated by exfiltrating subsurface lateral flow and from precipitation (i.e., recharge from the unsaturated zone model) on saturated areas. We use a quasi 3-dimensional shallow unconfined aquifer model based on the Dupuit-Forcheimer approximations (Childs, 1971) for groundwater flow above a sloping impermeable boundary. We solve for the (saturated) aquifer thickness $h(x,y,t)$ based upon the lateral groundwater flux $q(x,y,t)$, local runoff production $q_s(x,y,t)$, and recharge $r(x,y,t)$. Surface water discharge $Q(x,y,t)$ is calculated by instantaneously routing q_s over the area upslope from a given location. The governing equations for the hydrological model are:

$$\frac{\partial h}{\partial t} = \frac{1}{n_e}\Big(r - \nabla \cdot q - q_s\Big) \tag{14}$$

$$q = -h\cos\theta k_s \big(\nabla z + \nabla h\big)\cos\theta \tag{15}$$

$$q_s = \mathcal{G}\Big(\frac{h}{b}\Big)\mathcal{R}\Big(r - \nabla \cdot q\Big) \tag{16}$$

$$Q = \int_A q_s dA \tag{17}$$

where n_e is the drainable porosity, which we assume to have a constant value, k_s is the saturated hydraulic conductivity, and $\theta(x,y,t)$ is the slope of the aquifer base. The regularization function $\mathcal{G}(\cdot)$ is equal to zero when the argument is less than 1, and approaches 1 as the argument approaches 1. In this case the argument h/b represents the portion of the total permeable thickness b that is occupied by the aquifer with thickness h. The ramp function $\mathcal{R}(\cdot)$ is zero when the argument is less than zero and is equal to the argument when it is greater than zero. Thus, Equation (16) says that runoff will occur when the ground is saturated to near the surface and the recharge exceeds the divergence of the groundwater flux.

In our analysis, we further divide discharge into a fast-responding component (quickflow), and a slow-responding component (baseflow). Discharge during interstorm periods is defined as entirely baseflow, whereas baseflow during storm events is estimated by linear interpolation between the pre-storm-event discharge and the post-storm-event discharge. This approach works for our model because all runoff generated during storm events is instantaneously routed to the outlet (Equation 17), leaving only the slowly varying exfiltration to leave as runoff during interstorm periods; see Figure S3 for an example. Quickflow, which is nonzero only during storm events, is then some combination of exfiltration and precipitation on saturated areas. Although the regularization functions in Equation (16) make it difficult to isolate their respective contributions, precipitation on saturated areas is usually the dominant contribution to quickflow as the model lacks mechanisms that would rapidly increase exfiltration during storm events.

3 Model implementation

3.1 Modeling platform

The governing equations were solved on a 125×125 square raster grid. The grid cell size is best considered within the framework of the nondimensionalization we use, which will be discussed in Section 4. The top, right, and left boundaries are zero-flux boundaries, while the bottom boundary is a fixed value (Dirichlet) boundary, where the land surface and water table elevation are coincident. The initial condition is a near flat, roughened surface with zero elevation above baselevel. The domain can be considered in a moving reference frame, where the bottom boundary is an adjacent lateral stream (albeit with zero slope) incising at a rate U. The vadose profile was discretized such that each depth increment is equal in size and has a maximum unsaturated storage $\leq$ 1% of the mean storm depth.

The model is implemented as a Python package called DupuitLEM that is built on process components from the Earth surface modeling platform Landlab (Barnhart et al., 2020; Hobley et al., 2017). The LEM is solved using existing process components in a loosely coupled scheme, where diffusion is solved with a forward Euler finite volume method and the streampower erosion module is solved with an implicit method based on Braun and Willett (2013). The groundwater model (Litwin et al., 2020) is solved with an approach that combines explicit calculation of lateral groundwater flow and an analytical solution for groundwater rise and exfiltration based on the regularization presented by Marçais et al. (2017).

3.2 Upscaling discharge to geomorphic time

In any computationally feasible model of landscape evolution that incorporates hydrological processes, some scaling is needed between the timescales of the two models. We simply cannot simulate hydrological processes for millions of years. This temporal scaling has two primary approaches: online updating and offline updating. An online updating approach matches one hydrological time step to one geomorphic time step, and simply scales the effect of each event to represent some longer duration of time. An offline updating approach simulates hydrology on a fixed landscape over some duration from which meaningful average quantities can be derived. The average quantities, including discharge, are then used to evolve the landscape over some longer duration. Although both approaches have benefits and drawbacks, here we used an offline updating approach, as it allows for greater continuity of hydrological state. In an online updating approach, the model may erode substantial regolith and the water within the regolith in each time step, making it difficult to have a meaningful water balance. Here we ran the hydrological model for 25 storms before using the results to evolve the landscape forward in time. The scaling factor between hydrologic and geomorphic time varies by the simulation from 250 to 64000, depending on the duration of the mean storm-interstorm period.

In this paper we consider time-varying precipitation and recharge, and as a result Q^* will also vary substantially on hydrological timescales. As stated previously, $\langle Q^* \rangle$ is the temporal average of Q^* used to obtain an effective value that can be applied on landscape evolution timescales. Because Equation (5) is linear in $\langle Q^* \rangle$, this can simply be the time-weighted mean discharge. This would not be the case when an incision threshold is present, or when the exponents in the incision model are changed.

4 Scaling analysis

Dimensional analysis is a powerful tool for examining the behavior of models, allowing us to identify groups of parameters that affect the solutions to the governing equations in related ways. Litwin et al. (2021) nondimensionalized a simpler version of the model presented here with linear hillslope diffusion and uniform recharge directly to the water table. The nondimensionalization applied the concept of symmetry groups (Barenblatt, 1996), minimal sets of parameters that, when scaled by a constant factor, leave the governing equations unchanged. We nondimensionalized the governing equations systematically by carefully choosing the constant factors and introducing definitions of equivalent dimensionless variables.

The approach used characteristic scales derived from the model parameters to isolate dimensions of the model. These are listed in Table 1. We applied the same symmetry group approach presented in Litwin et al. (2021) to the continuum equations of the model used here to determine the following dimensionless governing equations:

$$\frac{\partial z'}{\partial t'} = - Q^* \sqrt{a'} |\nabla' z'| + \nabla' \cdot \left(\nabla' z' \left(1 + \left(\frac{\nabla' z'}{S_c/\alpha} \right)^2 \right) \right) + 1 \tag{18}$$

$$- \nabla' \cdot \left(a' \frac{\nabla' z'}{|\nabla' z'|} \right) = 1 \tag{19}$$

$$\delta \frac{\partial h'}{\partial t} = r' - \nabla' \cdot q' - q'_s \tag{20}$$

$$q' = - h' \cos^2 \left(\arctan |\alpha \nabla' z'| \right) \left(\nabla' h'/\beta + \nabla' z' \right) \tag{21}$$

$$q'_s = \mathcal{G} \left(\frac{h'}{\gamma} \right) \mathcal{R} \left(r' - \nabla' \cdot q' \right) \tag{22}$$

$$Q^* = \frac{1}{A'} \int_{A'} q'_s dA' \tag{23}$$

where prime indicates a dimensionless equivalent (defined in Section 8). Five dimensionless groups, plus the critical gradient S_c, remain as parameters. These are listed in Table 2.

Symbol	Name	Definition
h_g	Characteristic geomorphic height scale	$\left(\frac{DU^3}{v_0^2 K^4}\right)^{1/3}$
ℓ_g	Characteristic geomorphic length scale	$\left(\frac{D^2}{v_0 K^2}\right)^{1/3}$
t_g	Characteristic geomorphic time scale	$\left(\frac{D}{v_0^2 K^4}\right)^{1/3}$
h_a	Characteristic aquifer thickness	$\frac{p\ell_g}{k_s h_g/\ell_g}$
t_d	Characteristic drainage timescale	$\frac{\ell_g n_e}{k_s h_g/\ell_g}$
l	Domain length	–

Table 1. Characteristic scales that were derived to isolate the dimensions (length, height, and time) of the model.

Symbol	Name	Characteristic Scale Definition	Parameter Definition
α	Characteristic gradient	$\frac{h_g}{\ell_g}$	$\frac{U}{v_0^{1/3} D^{1/3} K^{2/3}}$
β	Aquifer relief scale	$\frac{h_g}{h_a} = \frac{k_s h_g^2}{p \ell_g^2}$	$\frac{k_s U^2}{p\, v_0^{2/3} D^{2/3} K^{4/3}}$
γ	Drainage capacity	$\frac{b}{h_a} = \frac{b k_s h_g / \ell_g}{p \ell_g}$	$\frac{b k_s U}{p D}$
δ	Timescale factor	$\frac{t_d}{t_g}$	$\frac{n_e\, v_0^{2/3} D^{2/3} K^{4/3}}{k_s U}$
λ	Domain scale factor	$\frac{l}{\ell_g}$	$\frac{l v_0^{1/3} K^{2/3}}{D^{2/3}}$

Table 2. The dimensionless groups (plus S_c) that appear in the dimensionless equations (18–23).

Of the dimensionless groups, we expect β and γ to be the most important controls on emergent hydrological behavior, as they affect critical aspects of hydrological function. The aquifer relief scale β describes the geomorphic height scale relative to aquifer thickness, which was called the hillslope number in Litwin et al. (2021) because its form is analogous to Brutsaert (2005, their Eq. 10.139) used to understand shallow groundwater dynamics. However, we found that it was harder to interpret β as a hillslope number in this study due to the combination of evolving landscape form, time-variable recharge and evapotranspiration. We will return to the discussion of the hillslope number and the role of β in Section 6.6. The drainage capacity γ describes the permeable thickness relative to characteristic aquifer thickness, or equivalently the ratio of a characteristic Darcy flux to precipitation on a hillslope with length ℓ_g. The characteristic gradient α is the ratio of geomorphic height and length scales, which we will keep fixed in this paper, but was explored in Litwin et al. (2021). The timescale factor δ is the ratio of hydrologic to geomorphic timescales, which we expect to be small in all cases given the large difference between hydrologic and geomorphic process rates. Lastly, λ is the domain scale factor, where l is the domain side length. λ is large in all cases considered here, and is not expected to affect our results (Anand et al., 2022; Bonetti et al., 2020; Litwin et al., 2022).

The stochastic forcing introduced three additional parameters: mean storm duration $\langle t_r \rangle$, mean interstorm duration $\langle t_b \rangle$, and mean storm depth $\langle d_s \rangle$, while the inclusion of vadose zone dynamics and evapotranspiration introduced two additional parameters: evapotranspiration rate *pet* and plant-available water content n_a. We found that four dimensionless groups were needed to represent the additional parameters, shown in Table 3. These groups were chosen to provide intuition into competing processes. The dimensionless forms of the Schenk model are given in Appendix B, Equations (A15) and (A21).

Although all of the dimensionless groups in Table 3 may be important for hydrological function and emergent landscapes, we focused on variation in σ and aridity index Ai. The water storage index σ describes the competition between the maximum possible saturated zone storage and mean storm depth, where smaller values indicate that local saturated zone storage is more easily exceeded by storms. Ai is the duration-corrected rate of potential evapotranspiration relative to rainfall, which has a critical effect on how much water becomes recharge. The precipitation steadiness index ρ is the proportion of time in which rainfall is occurring, which in the limit of $\rho \to 1$ is the steady case considered by Litwin et al. (2021). Lastly, the moisture content index ϕ describes the vadose zone plant-available water content relative to the saturated zone drainable porosity.

Symbol	Name	Parameter Definition
σ	Water storage index	$\frac{bn_e}{p(\langle t_r \rangle + \langle t_b \rangle)}$
Ai	Aridity index	$\frac{pet\langle t_b \rangle}{p(\langle t_r \rangle + \langle t_b \rangle)}$
ρ	Precipitation steadiness index	$\frac{\langle t_r \rangle}{\langle t_r \rangle + \langle t_b \rangle}$
ϕ	Moisture content index	n_a/n_e

Table 3. The additional dimensionless groups needed to describe the climatic and vadose models.

5 Results

We conducted simulations to explore the effects of subsurface properties and climate on morphology and runoff generation by varying the dimensionless groups identified in Section 4. Although the simulations do not cover the entire parameter space, they are sufficient to show a range of hydrologic behaviors that emerge from the coupled model. The results are presented in three sets of simulations. First, we varied σ and Ai, holding other dimensionless groups constant (except the timescale factor δ, although the effects of this variation are assumed to be negligible). Second, we ran the same combination of σ and Ai but decreased β by a factor of 10 to examine a case where aquifers are thicker relative to relief. Finally, we fixed Ai to a humid value of 0.5 and varied γ and σ to explore the interaction of storage and drainage in the subsurface.

All our results focus on the climatic end-member where storm durations are short relative to the time between storms ($\rho = 0.03$). We used the average value of α investigated by Litwin et al. (2021) ($\alpha = 0.15$), the domain scale factor was fixed at $\lambda = 250$, and others were chosen to be physically reasonable, including a critical slope $S_c = 0.5$ and moisture content index $\phi = 1.5$.

We ran simulations for $2000t_g$, by which time, most simulations had reached an equilibrium where mean relief was no longer increasing (Supplemental Figure S1). Cases not reaching equilibrium tend to be arid, and have poorly developed drainage networks. Once the landscape evolution simulation had completed, we ran the hydrological component of the model (without changing the topography) for $2000(\langle tr \rangle + \langle t_b \rangle)$ using the final water table as an initial condition to collect more detailed information on hydrological state and fluxes. Spatially distributed output (saturated area, recharge) were recorded at the storm-interstorm timescale, while spatially-lumped data (water balance components, total saturated area, total storage) were recorded at intervals corresponding to 1% of maximum timestep for groundwater model stability (Litwin et al., 2020).

5.1 Effects of climate on topography

Before examining the hydrological function of the evolved landscapes, we will begin by examining their topography. Aridity index Ai and water storage index σ play important roles in determining the partitioning of precipitation into evapotranspiration, surface flow, and subsurface flow, which ultimately affects the amount of water available to shape topography through erosion. The hillshades in Figure 1A show the development of characteristic ridge-valley topography when Ai < 1, where drainage dissection decreases with increasing aridity. When Ai ≥ 1 drainage networks are minimal or nonexistent (given the domain size, boundary conditions and other parameters used). Relief also increases with increasing aridity, as relief increases with decreasing drainage dissection while α and S_c are held constant.

The water storage capacity σ modulates the relationship between topography and aridity. When σ is small, the subsurface has a small capacity to store water relative to the average storm depth, and consequently surface runoff is produced more frequently across more of the landscape, increasing dissection and lowering relief. In the results presented, we decreased σ by reducing rainfall frequency and increasing intensity while keeping water storage capacity constant. Figure 1 shows that drainage networks can form under higher aridity climates when σ is small, as large infrequent storm events have more potential to generate surface water runoff than if the same annual precipitation were spread amongst more frequent storms.

Cross sections through the subsurface (Figure 1B–E) show differences in relief and mean water table position between selected model runs. Humid landscapes with small storage indices have the least relief and maintain water tables close to the surface (Figure 1D). Arid landscapes with small σ have the highest relief, and water tables are near the impermeable bedrock except near channels. When σ is large (large permeable thickness and/or many small storms) aridity has a highly non-linear effect on topography, with effectively no stream dissection for cases where Ai>1.

5.2 Water balance partitioning

We examined the water balance at two levels, first partitioning of precipitation into actual evapotranspiration (AET) and total runoff through the lens of the Budyko framework (Budyko, 1974), and then used the L'vovich framework (L'vovich, 1979) to understand the quickflow-baseflow partitioning. The framework was applied to all three sets of model runs (varying Ai and σ, varying Ai and σ with low β, and varying σ and γ), which have corresponding topography in Figures 1, S5, and S6. All results show total fluxes into and out of the domain averaged over $2000(\langle tr\rangle + \langle t_b\rangle)$.

The Budyko plots in Figure 2A,D, show how precipitation is partitioned to evapotranspiration (rather than discharge) as a function of aridity, and the constraints that energy and mass balance place on this partitioning (dashed lines) for high and low β cases. In energy-limited environments, the maximum ratio $\langle AET\rangle/\langle P\rangle$ is $\langle PET\rangle/\langle P\rangle \approx$ Ai, whereas in water-limited environments, the maximum ratio is one. Model results in Figure 2A closely follow respective energy and water limitations at each aridity, indicating actual ET is occurring at close to the potential ET rate. In contrast, Figure 2D shows that when the aquifer relief scale β and water storage index σ are small (i.e., thinner aquifers relative to relief and smaller storage capacity relative to storm depth) and the climate is humid, substantially less precipitation becomes evapotranspiration (and more becomes discharge) than in the previous case. Figure 2G shows how this partitioning is affected by drainage capacity γ for a constant aridity Ai $= 0.5$, where poorly drained landscapes (low γ) appear to produce less actual ET relative to precipitation, although the effect is smaller than that of the aridity index Ai. In the particular stochastic simulations we ran, $\langle PET\rangle/\langle P\rangle >$ Ai, so we place the horizontal line at $\langle PET\rangle/\langle P\rangle$ to show that actual ET still does not exceed potential ET.

The L'Vovich framework allows us to more deeply understand the catchment water balance by decomposing discharge into quickflow Q_f that leaves the watershed rapidly during storms, and baseflow Q_b that is released more slowly. We examine (1) how precipitation is partitioned into quickflow and storage, and then (2) how storage is partitioned into ET and baseflow.

We first consider the fraction of precipitation that becomes quickflow, shown in Figures 2B,E,H. These show that quickflow fraction is sensitive to all dimensionless groups considered (γ, β, σ, and Ai). In Figure 2B, the quickflow fraction decreases rapidly with increasing aridity, until almost no quickflow is generated when Ai ≥ 1. In contrast, Figure 2E shows that when the aquifer relief scale β is small, quickflow is more sensitive to water storage index σ, and for $\sigma = 8$ the quickflow is greater that 50% even when Ai $=$

1. Quickflow fraction declines rapidly with increasing γ (Figure 2H) with a nonlinear dependence that is similar to the effect of aridity shown in Figure 2B.

Second, we can consider how the remaining precipitation (that has become storage rather than leaving as quickflow) is partitioned into evapotranspiration and baseflow (Figure 2C,F,I). In Figure 2C, we see that the baseflow fraction declines linearly with aridity in humid climates, and is minimal for Ai>1. This behavior is insensitive to the water storage index σ except in the smallest case. This is also true when the aquifer relief index β is small (Figure 2F), provided σ is large. However, when σ is small and the climate is humid, partitioning to baseflow is less sensitive to aridity, similar to the sensitivity seen in Figures 2D and E. Although quickflow fraction decreases with γ and aridity (Figures 2B, H), baseflow fraction generally increases with γ Figure 2I), the opposite of the pattern observed in baseflow fraction with aridity (Figure 2C). The baseflow fraction increases with γ until it levels out at a constant value as actual ET approaches potential ET (Figure 2G).

5.3 Spatial structure of recharge and saturated areas

The location and extent of saturated areas vary in time and space responding to changing recharge, water storage, and topographic states. Here we define recharge the same way it has been defined in previous sections, given by Equations (12) and (13). All water that is delivered to the saturated zone is defined as recharge, including when the water table is at the land surface, in which case the groundwater model determines how much will become runoff. As a consequence of the dependence of recharge on depth to water table (Equation 12), there are systematic variations in recharge rate with landscape position. Figure 3 shows the mean recharge rate $\langle r \rangle$ relative to the mean precipitation rate p in the same modeled cases shown previously in Figure 1. Lighter colors in Figure 3 highlight valleys and regions of convergent topography, where the water table tends to be close to the surface. Contrasts in recharge rates across different landscape positions increase with aridity until Ai $= 1$, at which point the water table is deep and the unsaturated zone tends to remain dry enough to hold precipitation without generating recharge (hidden cases in Figure 3 have no recharge). The relative recharge is also sensitive to σ, as large storms relative to permeable thickness (small σ) allow vadose water to reach the water table more frequently than when σ is large.

In order to examine spatial and temporal patterns of saturated area, we defined a metric of saturation occurrence and classified the landscape into zones that are wet, variably saturated, or dry. We define surface saturation based upon where the water table is within $0.025h_g$ of the ground surface. This metric approximates the "squishy boots" test used to identify variable source areas (e.g., Dunne et al., 1975). Areas that are saturated at the end of more than 95% of storms and interstorms are classified as wet, whereas locations that are saturated after less than 5% of storms and interstorms are classified as dry, and variably saturated areas are all others not in either of the previous classes (for our purposes, the classification is relatively insensitive to the choice of threshold values; for details, see Figure S4).

Results in Figure 4 show that the model produces widespread variably saturated areas organized around the interface between the channel network and adjacent hillslopes. In humid landscapes where the water storage index σ is small, channel networks are permanently saturated, and hillslopes can become saturated all the way to ridges at least occasionally (frequency > 0.05), when storm depths approach or exceed local saturated zone storage capacity. With increasing σ, variable source areas retreat to localized zones in channel heads and areas of topographic convergence. With increasing aridity, the water table tends to interact with the surface less frequently, leading to intermittent channel networks when Ai ≥ 1.

The transition to intermittent saturation in valley bottoms is also affected by the drainage capacity γ, due to its influence on the partitioning of water between surface and subsurface flow (Figure S9). When γ is large and σ is small, storms are large relative to storage, but subsurface drainage is efficient. Consequently, ridges remain dry, but saturation in valley bottoms is more variable than cases with lower γ or higher σ (see Figure S9, simulation 4).

Of note, discontinuous wet sections of the channel network emerge from the model without any introduced heterogeneity or spatial variation in permeable thickness. These can be seen for example in Figure 4 subplots 3, 4, 10, and 11, which have large β, intermediate Ai, and small σ. They also appear when γ is large (Figure S9), but are largely absent when β is smaller (Figure 5). These patterns are driven by differences in the local convergence and downslope conveyance capacity associated with topographic curvature and slope. These patterns are indicative of a discontinuous stream channel with both perennial and ephemeral reaches. It should be noted, however, that our saturation metric describes only the proximity of the water table to the surface, and does not include the presence of water routed from upslope, which in our model is not allowed to infiltrate once it has become surface runoff. Nevertheless, the emergence of this discontinuous network of saturated areas indicates that the morphology of the landscape, rather than just variability in subsurface properties, may provide a structural control on heterogeneous patterns of surface flow in valley bottoms. This feature is likely to persist in a model that allows re-infiltration, although instead of variably saturated valley bottoms, some areas of the parameter space may instead produce reaches that gain and lose water, again as a function of adjacent landscape morphology.

Other unusual features emerge as the aquifer relief index β becomes small, in which case the relief of the water table is similar to that of the topography. First, we observe that particular combinations of parameters produce drainage networks that are close to non-dendritic (Figure 5). This is highly unusual in LEMs, particularly those with single-direction flow routing and fluvial incision like this one. We say 'close to' non-dendritic because subtle drainage divides do exist such that surface flow is only routed in one direction at any particular topographic state – i.e., saddle-points. However, variable or even persistent saturation extends all the way up to these saddle-point divides, and flow directions near them may change frequently with evolving topography. Second, some model results show the presence of persistently saturated valley bottoms with widths greater than one pixel (e.g., Figure 5 subplots 10, 11, 17, 23, and 28). This is also uncharacteristic of the type of LEM formulation used here, which will generally incise valleys only one grid cell wide. This illustrates that erosion by runoff on saturated areas near the toes of hillslopes can help account for the formation of valleys that are substantially wider than the channels they contain. LEMs have generally only achieved valleys wider than one pixel by explicitly representing valley widening by lateral channel migration (Langston & Tucker, 2018). These permanent lowland wetland features and non-dendritic drainage networks are evidence of the strong influence that the aquifer structure can exert on surface drainage organization, even in a relatively simple model.

5.4 Co-variant dynamics of spatially-averaged saturation, storage, and discharge

The relationship between saturated area and baseflow discharge is a useful indicator of the relationship between landscape morphology, subsurface properties, and runoff generation (Latron & Gallart, 2007). We chose to examine baseflow rather than total flow because the total flow generated from a storm event for a given antecedent saturated area will be dependent on the storm intensity, whereas exfiltration-driven baseflow should vary more systematically with aquifer properties and topography.

Figure 6 shows the dimensionless baseflow discharge $Q_b^* = Q_b/pA_{tot}$ versus the dimensionless saturated area $A_{sat}^* = A_{sat}/A_{tot}$, where Q_b is the total baseflow discharge for the model domain, A_{sat} is the total saturated area, and A_{tot} is the total domain area. Saturated areas are calculated with the same criterion as in the spatially distributed figures. For reference, light gray points were added to indicate the total dimensionless discharge ($Q^* = Q_b^* + Q_f^*$). Baseflow points are colored by the dimensionless saturated storage $S^* = S/(bn_e A_{tot})$ to show relationships with saturated area and baseflow.

As expected from the spatial patterns of saturation in Figure 4, the range of the dimensionless saturated area decreases with increasing σ. When σ is large, the extent of saturated areas is fixed at approximately 10% of the watershed area in the most humid case, and decreases with increasing aridity. When σ is small, increasing aridity does not prevent the landscape from reaching near full saturation ($A_{sat}^* = 1$), but does lower the minimum saturated area, increasing the range of saturated area observed. Model runs with the same aridity tend to have similar minimum saturated extent, but with decreasing σ, the maximum saturated area generally increases.

Despite differences in the saturation-baseflow discharge relationship with the parameters shown, there are underlying patterns that may reveal features of the coevolved system. Primarily, we notice that the relationship between baseflow and saturated area has a concave up form in most cases, where the rate of change of saturated area increases with baseflow discharge. The simulations with the largest range in (log-transformed) A_{sat}^* (e.g., in Figure 4) appear to have a sigmoidal relationship, which can be divided into three regimes: rapid increase in saturated area with low baseflows, moderate increases in saturated area with moderate baseflows, and again rapid increases in saturated area with the highest baseflows. Several reference lines are included here for comparison with these regimes: $A_{sat}^* \sim Q_b^{*2}$, and $A_{sat}^* \sim Q_b^{*1/3}$, which are indicative of the rates of change in the upper and middle regimes, respectively.

How does the form of the saturation-baseflow discharge relationship relate to topography? We can contextualize the relationship by mapping points in Q_b^*–A_{sat}^* space back to their respective spatially distributed saturation patterns. We chose to examine the results in Figure 6-4 ($\sigma = 8.0$, Ai $= 1.0$) in more detail, as it displays the sigmoid form well. The mapping is shown in Figure 7, where subplots B–E show hillshades colored blue where the the ground is saturated, corresponding to the labeled points in subplot A. Subplot (B) shows saturated areas cover only the second order and higher stream channels under low-flow conditions. In (C), saturated areas extend up through first order channels, and some channel-adjacent areas. Above (C), in (D), saturated areas emerge in many unchannelized concave regions, while by (E), saturation is widespread on all concave and planar regions, extending toward ridges. Critically, we can see that the inflection point near (C) represents the threshold above which saturated areas emerge outside of the channel network.

The geomorphic transition between in-channel and out-of-channel saturated areas at the transition between the middle and high baseflow discharge regimes translates to cases that do not display the full sigmoid relationship. Figure S12 shows how saturation patterns are related to points in the baseflow saturated area relationship for the case shown in 6-14 ($\sigma = 8.0$, Ai $= 0.25$). The point of maximum curvature is still associated with increasingly widespread saturation outside of the incised channel network. This supports the idea that the saturated area baseflow relationship embeds information about landscape morphology (at least hillslope-channel transitions). However, as the cases with large σ demonstrate, the extent and variability of saturated areas affect how much of the morphology is visible in this relationship.

Varying the drainage capacity γ affects the shape of the relationship between baseflow discharge and saturated area. The slope of the middle regime decreases with increasing γ, and the transition between the middle and upper regimes sharpens. Topographically, high γ cases also have greater relief, lower drainage density, and sharper transitions between channels and hillslopes (Litwin et al., 2021). In contrast, when the aquifer relief index β is small, the relationship between saturated area and baseflow discharge weakens, as shown in Figure S10. We will return to additional synthesis of these relationships in the discussion.

6 Discussion

6.1 How do topography and hydrology coevolve in DupuitLEM?

The purpose of the model developed in this paper is to help us better understand how real topography and hydrologic dynamics coevolve. Therefore, clearly laying out how the simulated topography and hydrologic dynamics coevolve in the model is important. A clear conceptual understanding would make it far easier to comprehend the sensitivity of the results to variations in the parameters presented above, and to ascertain where the model may provide insight and where it is deceptive. A visualization of our conceptual understanding is illustrated in Figure 8.

In DupuitLEM, hillslope morphology evolves to simultaneously shed water and regolith at the rates they are supplied. Water is supplied by rainfall and is lost to runoff (when it falls on saturated ground), subsurface drainage, and ET. Regolith is supplied by uplift or baselevel change U, may be redistributed by diffusive hillslope transport E_h, and removed by water erosion E_f, which is driven by runoff. Note that diffusive hillslope transport (unlike water erosion) does not remove regolith from the model domain for the most part (except at the boundaries). It only moves regolith around, smoothing the landscape out. Therefore, the simulated landscape morphology must therefore evolve towards a condition where the production of runoff is just sufficient to remove regolith by water erosion at (areal-averaged) rate U.

The key to achieving this balance is the perennial aquifer that forms in areas of topographic convergence. For the visualizations in Figure 8 the perennial aquifer has been defined based on 95% exceedance probability of aquifer thickness, and therefore corresponds to the “wet” saturation zones in Figures 4, 5, S9. The perennial aquifer appears as dark blue in Figure 8. When storms are large and infrequent (i.e., small σ) and transmissivity is moderate (i.e., $\gamma > 1$), the perennial water table determines which areas experience variable and perennial surface saturation and fluvial erosion. Perennial saturation occurs where the aquifer reaches the surface. Variable saturation occurs where the perennial water table is shallow enough that storms can raise the water table to the surface (the variable water table shown in Figure 8 is defined based on 5% exceedance probability of aquifer thickness). Therefore, the landscape morphology must evolve such that the spatial extent of the perennial aquifer is large enough to ensure sufficient surface runoff production.

How does it do so? In short: by balancing supply and demand. The aquifers are continually draining, and so to remain at or above their minimum level, the aquifers must receive a continual supply of lateral subsurface inflows from adjacent hillslopes. Both the drainage rate and supply rate are controlled by the topography. Therefore, by controlling these rates (and therefore the extent of the perennial aquifer) a topography can emerge that ensures sufficient runoff production to remove regolith at the supplied rate U.

The rate lateral flow is supplied to the perennial aquifer is determined by the size of the accumulated area upgradient, and the recharge rate in that area. That recharge is exported downgradient toward convergent areas as subsurface flow. When γ is sufficiently large, the subsurface flow is sufficiently efficient that uplands never experience surface saturation (these are the beige areas in Figure 8).

With no overland flow, upland regolith must be exported to convergent areas via diffusive hillslope transport if it is to be removed from the domain by water erosion. At each point in the uplands, the diffusive flux must transport not only the regolith supplied locally by uplift/base level change, but also the regolith arriving from upslope. The demand for increasing regolith transport capacity with distance from the ridge imparts a convex profile to the uplands, such that slope increases moving downhill, up to the critical slope S_c.

The rates of regolith and water export from the uplands to the convergent areas must strike a delicate balance. The regolith export must be *small* enough that it does not overwhelm the capacity of water erosion in the convergent areas to remove it. The water export must be *large* enough that it can sustain the perennial aquifer that makes that water erosion possible. However *both the regolith export and water export rates will depend on the accumulated area at the transition from uplands to convergent areas.* Therefore, the drainage density must adjust until these demands are in balance. If the drainage density is too small, excess lateral flow from the uplands will expand the perennial aquifer, leading to increased surface saturation and water erosion. If the drainage density is too large, lateral flow will be insufficient to maintain the perennial aquifer and promote water erosion, and so diffusive regolith flux will gradually fill the the convergent areas and remove them from the topography.

The rate of lateral inflow required to maintain the perennial aquifer is the one that matches the rate the perennial aquifer is draining downslope. The perennial aquifer drainage rate is controlled by the transmissivity $k_s b$ (which is fixed), by the local basement slope (which in DupuitLEM is determined by the topography because the permeable thickness b is constant in space), and potentially also by the level of the water table farther downgradient. As discussed later in this section, the latter is only important when β is small, and is overwhelmed by topographic gradients when β is large.

The roles of the recharge, transmissivity, and local slope at the transition from upland to convergent area are captured by the dimensionless parameter γ, which explains its importance in controlling drainage density. The slope of the convex uplands will tend to vary downslope in proportion with distance from the ridge and with ridge curvature. More precisely, at distance x we would expect the slope to be approximately $x\xi(x)h_g/\ell_g^2$. $\xi(x)$ is less than 1 and captures the effect of the nonlinearity in the hillslope diffusion law (in fact $\xi(x) = \tanh\left(xh_g/\ell_g^2/S_c\right) / \left(xh_g/\ell_g^2/S_c\right)$ for the exact form of the nonlinear diffusion law (Equation (3)). The maximum subsurface flow per unit width at that point is therefore $xk_sbh_g\xi(x)/\ell^2$. If area per contour width upslope from that point is $a(x)$ and the recharge is $r(x)$, it follows from the definition of γ that in the vicinity of the transition from uplands to where surface saturation and water erosion becomes important the following is true:

$$\frac{a(x)}{x} \times \frac{r(x)}{p} \times \frac{1}{\xi(x)} \approx \gamma \tag{24}$$

The first term on the left is the area per contour width divided by distance from the ridge. This quantity is a measure of the degree of topographic convergence. It will be ≈ 1 for straight slopes, < 1 for divergent areas, and > 1 for convergent areas. The second term measures the fraction of precipitation that becomes recharge, and is therefore influenced by the aridity Ai. Therefore, γ sets the degree of upland contributing area convergence needed to produce surface saturation and water erosion, modulated by the effect of water balance on recharge and nonlinear slope processes. This makes it clear why γ has such an important control on the drainage density of the coevolved landscapes (see Figure S8), and why aridity also plays a role (see Figure 4). Both effects are illustrated in Figure 8.

Note that γ depends on the transmissivity $k_s b$, rather than on the hydraulic conductivity k_s alone. That means it is possible to vary the permeable thickness while keeping γ constant by also varying the hydraulic conductivity inversely. Doing so amounts to varying β – a small β corresponds with a large permeable thickness. This was explored in Litwin et al. (2021), where β was referred to as the hillslope number Hi. This is perhaps regrettable, because although β is closely related to the hillslope number (as we shall see in Section 6.6), they are not the same thing. As with the hillslope number, when β is small, the aquifer thickness becomes large relative to the relief, making it possible for water table gradients to substantially differ from topographic gradients.

As a consequence, when β is small, the drainage rate of the perennial aquifer is more dependent on the landscape morphology downgradient. Because the slopes downgradient are gentler in lowland areas, the drainage rate is slower relative to the case with large β. Consequently the rate of lateral inflows can be smaller, and a smaller upslope area is needed to supply those inflows. This explains the larger areas of perennial and variable surface saturation when β is small (Figure 5), compared to when it is larger (Figure 4).

Some remarkable effects emerge when β is small, as shown in Figure 5. Under the right circumstances, the large permeable thickness allows the perennial aquifer to be connected across surface topographic divides, resulting in connected loops surrounding isolated 'islands' of uplands. Broad, low-gradient areas of perennial and variable saturation emerge (Figure 8), particularly around confluences.

The conceptual explanation of the model results presented here can also help us understand the variations with σ and Ai that appear in earlier figures. When σ is small, storms are large and infrequent relative to the subsurface storage capacity. Consequently, there is time between storms for the saturated aquifer to contract to only the most convergent areas, where it promotes transient surface saturation during subsequent storm. When σ is large, the perennial aquifer is more extensive because there is not time to contract before the next event, but the smaller storms mean transient surface saturation is less likely. These effects can be seen in Figures 4, 5, 8, and S8.

The variable source areas that emerge when σ is small allow for more widespread water erosion to remove regolith from the landscape. This results in lower relief than when σ is large (Figure 8).

The conceptual understanding presented so far does not account for all of the model behavior though, and additional details need to be considered. In our results, there is a transition between channelized and unchannelized topography between Ai = 0.71 and Ai = 1.41 in Figure 1, and the transition is more abrupt for large σ. This can be attributed to the reduced likelihood of recharge when Ai > 1 as captured in the Schenk model of the vadose zone. Recall that ET creates a storage deficit in the vadose zone that must be satisfied before rainfall from an individual storm event can produce recharge at depth. When Ai < 1, the potential ET between storms tends to be smaller than the rainfall that typically falls in each storm. Consequently the vadose zone tends to be wet at depth, and the effects of ET are limited to generating deficits close to the surface. However, when Ai > 1, the storage deficit that can accrue between storms is larger than the depth of rain that typically falls in each storm. Consequently the vadose zone is dry at depth, and recharge will only occur from a storm large enough to fill the profile, or when storms are clustered together. This becomes increasingly unlikely when σ is large, because σ includes the ratio of profile thickness to storm depth: $bn_e/p(\langle t_r\rangle+\langle t_b\rangle)$. Note that the likelihood of recharge *per se* is not related to the drainable porosity n_e but to the plant available water content n_a, and so the relevant dimensionless control on recharge is $\sigma\phi$.

Given less frequent recharge when Ai > 1, larger hillslopes are needed to supply the lateral flow necessary to sustain a perennial aquifer in areas of topographic convergence. This makes areas of permanent or variable saturation less extensive.

6.2 How does hydrogeomorphic coevolution play out in transient landscapes?

So far, we have focused on landscapes at dynamic equilibrium between uplift and erosion. This condition is powerful for studying the emergent behavior of LEMs (e.g., Bonetti et al., 2020; Theodoratos et al., 2018); however, transience is likely the norm in real landscapes (Whipple, 2001). Moreover, transience may offer clues to distinctive features of hydrological function at dynamic equilibrium. As a shorthand, we will use the term "age" to refer to the degree of progression toward a dynamic equilibrium, given an initial near-flat surface at baselevel. However, we recognize that this age is largely conceptual; real landscape evolution rarely follows such a linear progression or has such a clear initial state.

To examine transient evolution, we can select some points in time to examine. Although we could have selected points evenly spaced in time, the model state does not progress linearly. Change in mean elevation $\bar{z}$ for example tends to approach the steady-state value asymptotically (Figure S1). Assuming other features of interest may change in a similar way, we selected quantiles of mean elevation through time and examined topography and hydrological function at the corresponding times. Figure 9 presents the results of a single model run at times when mean elevation $\bar{z}$ is 10, 30, 60, and 90% of the final value. Figure 9M shows the time evolution of mean elevation and the four selected quantiles.

With increasing age, topography changes dramatically, from gentle slopes and high levels of drainage dissection, to steeper, broad hillslopes, and a more sparse drainage network (Figure 9A–D). The size of areas that are always and variably saturated decrease with increasing age (Figure 9E–H), from 7.1 and 54.4% of the modeled area, respectively, in the 10% mean elevation case to 0.6 and 24.1% in the 90% mean elevation case. The baseflow-saturated area relationship also evolved substantially (Figure 9I–L). Earlier in the development, the landscape exhibits greater saturated area, storage, and discharge. Mean saturated area decreases 65.0%, Q^* decreases 57.8%, and mean baseflow Q_b^* declines 27.0% over the course of the simulation presented, resulting in an increase in the baseflow index Q_b^*/Q^* with age. Although baseflow index increases, more developed landscapes experienced much lower discharge and storage at their driest states than the same landscape earlier in its development.

Even in the absence of subsurface hydrology, LEMs with flat initial conditions and uplift show increasing elevations as slopes steepen toward the point at which the denudation rate matches uplift. However, when subsurface hydrology is important, steepening slopes can also increase hydraulic gradients, increasing the capacity of the subsurface to drain water. In the absence of surface water that would form rills or channels, longer hillslopes can be maintained. However, hillslope length is limited by the increased recharge that a longer hillslope will collect and have to transport laterally downslope. Steeper hydraulic gradients also reduce the thickness of the aquifer needed to convey the same flux. Decreasing aquifer thickness affects recharge, which decreases when the water table is deeper, further reducing discharge and baseflow, as shown in Figures 9I–L.

The evolution seen in these results may mimic observations in post-glacial landscapes that evolve fluvial drainage from low relief, regolith mantled 'initial' states. The recently glaciated site shown in Figure 9N is located in northern Wisconsin, USA, and has low relief and abundant wetlands. Here, the water table is close to the surface, and subsurface lateral flow is less important for runoff generation than surface water connectivity. In contrast, the driftless region of Wisconsin was not recently glaciated (Figure

9O) and has greater relief and well-developed fluvial topography. Here springs and groundwater flow are more important for runoff generation. The driftless landscape is well drained, and watersheds may even have intermittent streamflow regimes (Sartz et al., 1977). The contrast between these two sites is consistent with observed decreases in runoff and saturation with age in our simulations. The evolution of post-glacial landscapes has been examined in further detail by Cullen et al. (2022), who found that groundwater flow plays an essential role in concentrating discharge and initiating the formation of fluvial topography in low-relief landscapes. They focused on the erosion of channels into a confined aquifer, rather than emergence of saturated areas from an unconfined aquifer. Further work could be conducted to unify the saturation excess runoff process presented here with the confined aquifer system that Cullen et al. (2022) have examined, which may explain more of the emergent hydrogeomorphic dynamics of post-glacial landscapes when considered together.

Lastly, we return to the question of the applicability of this catchment "age" more broadly. Although Troch et al. (2015) suggested that a hydrologically relevant age could be useful in understanding differences in hydrologic function between sites, in general the hydrologically relevant age of a landscape is not an easily defined quantity. They provided a framework for catchment coevolution in which age does not increase one-to-one with time, but rather increases at different (and potentially nonlinear) rates depending on lithology, climate, and tectonics. For example, the hydrologically relevant age may increase faster in a wetter climate than in a drier one. Applying this concept to our transient results, we see that differences in climate and subsurface properties affect the rate of relief change, which in turn affects the rate hydrological response changes. However, defining an age inevitably encounters the issue of defining an initial condition from which to start the clock. Troch et al. (2015) give the example of applying this framework to volcanic catchments, which have well-defined initial conditions from which the evolution can be measured (Jefferson et al., 2010; Yoshida & Troch, 2016). However, this may be the only case where such a clear initial hydrologic and geomorphic condition can be identified (although the post-glacial scenario we have discussed may be adequate). The direction of hydrologic response change with age is also particularly sensitive to the initial condition. Although we see decreasing saturation with time in our simulations, the trend may be very different if we were to take, for example, a Davisian approach in which the initial condition is a high plain that gradually erodes to baselevel (Davis, 1899). All of this indicates that evolving hydrological function is a complex story that would be best told within a geological context. More work would be needed before we can adequately apply the framework of evolving catchment function to real sites.

6.3 How realistic is the hydrology in DupuitLEM?

As illustrated in the results above, DupuitLEM produces landscapes that not only have the appearance of realistic topography, they function hydrologically as one would expect of a realistic landscape – up to a point. The model results deviate from what we might expect in a real landscape in several ways that are worth highlighting.

In the arid cases, as shown in Figure 2A, almost no runoff is produced by the model, and the resulting landscape is unchannelized. Many real arid landscapes will still produce substantial runoff at an aridity index of 2 (the maximum value we considered) (e.g., Wang & Wu, 2013), and exhibit widespread channelization. However, runoff is rarely produced by the interaction of the water table with the ground surface in those landscapes. In that sense our model is in full agreement. Instead, runoff in arid landscapes is more often generated by a low infiltration capacity relative to rainfall intensity (infiltration excess overland flow) (Wu et al., 2021). This mechanism is not included in the analysis here, but can be easily added through the modular modeling framework of DupuitLEM.

Another deviation from our expectations appears in the water balance when β and σ are small: as Figure 2D shows, deviations from the energy and water bounds are large in the Budyko plot. The increased quickflow fraction shown in Figure 2B (relative to the high β case in 2E) offers a clue as to why this deviation may be occurring. Because quickflow is primarily derived from precipitation on saturated areas, the deviations from energy and water limitations indicate these cases have more extensive saturated areas than their high β counterparts in Figure 2B. We can confirm this by examining spatial patterns of saturation in Figures 4 and 5. Indeed there are large areas of permanent saturation in the low β case. A larger fraction of quickflow is more likely when σ is small because in these cases storms more easily overwhelm available storage and produce additional saturated areas. As more precipitation becomes quickflow, less is available to become evapotranspiration, and the Budyko plot (Figure 2D) deviates from water and energy balance constraints.

The issue is exacerbated by the lack of ET from the saturated zone in our model. In reality ET may be substantial from the large permanently saturated areas shown in Figure 5, but in the model ET from these areas is zero (because ET is only accounted for in the unsaturated zone, and there is no unsaturated zone where the water table reaches the surface). This is an issue that can be explored in future work.

With the parameters we have considered, the other large deviation of $\langle AET\rangle/\langle P\rangle$ from $\langle PET\rangle/\langle P\rangle$ occurs when γ is small. This is somewhat paradoxical; Troch et al. (2013) found that landscapes with the longest drainage timescales tend to have the highest ET relative to precipitation because water that stays in the landscape longer is more likely to become ET. In fact, we can see that this is partially still the case in our results. Figure 2I shows that the baseflow fraction of remaining water is smallest when γ is small, indicating that more water is becoming ET. However, this is not controlling the overall water balance behavior. Instead, quickflow behavior controls the decrease in $\langle AET\rangle/\langle P\rangle$ with decreasing γ, as the proportion of precipitation that becomes quickflow declines precipitously with increasing γ, as shown in Figure 2H. Poorly drained landscapes (with low γ) have water tables closer to the surface, and greater saturated areas to generate quickflow during storms. Increasing this quickflow fraction decreases the water that remains available to become ET. Poorly drained landscapes also would be expected to make more water available for ET, as Troch et al. (2013) showed, but because our model ET cannot access water in the saturated zone, we are not able to reproduce this observation.

The one-way coupling of saturated and unsaturated flow has implications for runoff generation as well as ET. For example, with little or no additional recharge, the water table can rise rapidly into the capillary fringe (e.g., Crosbie et al., 2005; Gillham, 1984; Weeks, 2002). If the capillary fringe extends to the surface, as it may in wetter areas like concave hillslopes and valley bottoms, saturated areas could expand rapidly during storm events. Saturation of the soil profile due to wetting front propagation (e.g., Ogden et al., 2017) also could enhance the rapid emergence of saturated areas. On the other hand, ET from the saturated zone where it is near the surface could substantially reduce saturated areas during interstorm periods. Because we do not capture these features, we may substantially underestimate the variability of saturated areas and, depending on their relative importance, we may overestimate or underestimate runoff generation from saturation excess.

The form of our groundwater model may also affect features that we observe across our parameter space. In order to have tractable solutions for the landscape evolution model, the groundwater flow model we use relies on the Dupuit-Forcheimer approximations, which are valid where the component of flow normal to an impermeable lower boundary is small. This usually occurs when saturated thickness is small relative to hillslope or seepage face length (Bresciani et al., 2014), which may not be valid everywhere in our model parameter space. Even where this assumption is valid, the model focuses on relatively shallow groundwater flow paths. Field studies have shown that deeper flow paths through bedrock are important components of stream runoff, especially during baseflow conditions. Accounting for these deeper flow paths could increase baseflow discharge, changing the L'vovich water balance partitioning shown in Figure 2.

6.4 What processes were left out of DupuitLEM?

In the interest of creating a tractable model, we have left out several key climatic, hydrologic, and geomorphic processes that may affect the coevolution of runoff generation and topography. First, our representation of climate is simplified, as we neglected seasonality of precipitation or potential ET, which are important controls on the water balance and on the extent of saturated areas (Latron & Gallart, 2007; Yokoo et al., 2008). In the previous section we described two missing hydrological processes: infiltration excess overland flow and ET from the saturated zone. We also neglected the two-way coupling between saturated and unsaturated flow, and the presence of reinfiltration from run-on, both of which would require more sophisticated models and computationally-intensive iterative solutions. Deeper groundwater systems, which may make important contributions to baseflow, were also neglected (Hare et al., 2021). Considering only single direction flow routing with no depression storage also limits the development of valley bottoms and wetlands that can be important zones for saturation excess overland flow, although we did observe that valley bottoms can emerge despite model limitations in areas of the parameter space where aquifers are thick relative to topographic relief.

The style of water erosion is also limited in this model, as we consider only detachment-limited fluvial erosion, neglecting fluvial sediment deposition and factors such as groundwater sapping (Abrams et al., 2009; Laity & Malin, 1985) and pore-pressure driven landslides (Montgomery & Dietrich, 1994), which could be the subject of separate studies of coevolution between topography and groundwater systems.

We have also limited our study to understanding the evolution of topography, while the progressive weathering of rock and development of a regolith mantle are simultaneous components of critical zone evolution. Furthermore, we have considered only cases where the subsurface porosity and hydraulic conductivity is constant in a zone that uniformly parallel to topography. This can have unintended consequences. During transient evolution, areas that aggrade due to hillslope diffusion must turn sediment back into bedrock to maintain a constant thickness. Although this issue should not affect results at dynamic equilibrium, more work would be needed to accurately treat the subsurface in LEMs.

Recently, critical zone science has provided insights into the structure and evolution of the subsurface. Critical zone structure varies with depth, but may also vary systematically across landscapes, even mirroring topography in settings experiencing strong tectonic compression (St. Clair et al., 2015). Other hypotheses for subsurface evolution related to geomorphic, geochemical, and ecological processes have been put forth (Anderson et al., 2013, 2019; Brantley, Eissenstat, et al., 2017; Brantley, Lebedeva, et al., 2017; Harman & Cosans, 2019), and would likely result in different surface evolution when considering subsurface-driven runoff generation. Here we have laid the foundation for future modeling that can build toward whole critical zone evolution that considers both surface and subsurface features and processes.

6.5 Does DupuitLEM match field evidence for the relationship between saturated area and baseflow?

As we have shown, saturated area-discharge relationships contain information about runoff generation. However, variation in saturated area through time has not been widely reported in the literature as the measurements are labor intensive and can be sensitive to the judgement of the observer. Latron and Gallart (2007) compiled many published relationships into a single plot (reproduced in Figure 10) that shows a range of forms the relationship can take. We would like to compare our results with those in this plot, but so far we have only presented dimensionless versions. Choosing a set of dimensioned parameters (as is necessary to run the model) allows us to re-project the results into the dimensioned world for comparison. We did this for several results presented in Figure 6. The caveat to this approach is that the position of the results, especially along the x-axis, is subject to the particular dimensioned parameters we have chosen.

In humid climates, our results show strong resemblance to the concave up form observed by Dunne (1978) at Sleepers River, VT, USA. Saturated area and baseflow in this relationship were measured in Sleepers River Watershed W-2, which has gentle topography and relatively low permeability soils (Dunne et al., 1975), consistent with our low σ cases. Dunne et al. (1975) also observed lower variability in baseflow discharge and saturated areas in a steeper watershed with deeper and more permeable soils (Sleepers River Watershed WC-4, not shown), consistent with our high σ cases.

Field relationships by Ambroise (1986), Latron (1990), and Myrabø (1986) shown in Figure 10 have convex forms, where baseflow increases faster than saturated area in log-space. Some of our model results (e.g., Figure 7) also have convex forms for lower baseflow and saturated areas, but these relationships seem to have a different origin. In our case, the low baseflow regime was associated with channel network ephemerality, whereas the field studies are still primarily describing variable source areas in valley bottoms and adjacent hillslopes. In fact, the studies here with the lowest saturated extents appear to have linear or slightly concave relationships. However the linear relationship shown by Latron and Gallart (2007) is from a terraced landscape with fragmented saturated areas, which obscure the link between topography and baseflow. Reasons why observed relationships could be different from our model predictions are numerous. Our model has only considered a limited number of runoff generation and landscape evolution processes, and lacks the heterogeneities and complexities of real watersheds. However, it is encouraging that our results agree with field surveys from Dunne et al. (1975), given that ours are emergent features of coevolution.

6.6 How does DupuitLEM compare to the Dunne Diagram? Role of the hillslope number

Dunne (1978) presented a synthesis of how runoff generation mechanisms are related to topography, subsurface properties, and climate, often called the "Dunne Diagram" (Figure 11A). On the humid half of the diagram, Dunne associated saturation excess overland flow (i.e., Dunne overland flow) with gentle topography, and moderate to poorly drained soils. Subsurface storm flow was considered the opposite end member, and was associated with deeper, more permeable soils and steeper straight to convex topography.

We have mapped this conceptual relationship into a quantitative relationship between hydrological and geomorphic metrics to compare with our results to see whether the relationship applies. We quantified the geomorphic aspect by focusing on the difference between gentle and steep topography. We used topographic variance $\overline{Z}$ to quantify hillslope relief above valley bottoms without channel or hillslope delineation. Because of the domain boundary conditions (zero flux on all but the bottom) elevation increases systematically from the bottom to top boundaries, but not between the side boundaries, so we calculated the variance of topographic elevation for each horizontal slice of the domain, found the mean of the slice variances, and took the square root to obtain $\overline{Z}$ with units of length. We normalized $\overline{Z}$ with the characteristic height scale h_g for consistency with our dimensionless framework. The hydrologic metric is more straightforward. In our model, quickflow is generated primarily by Dunne overland flow, so the fraction of quickflow relative to total flow $\langle Q_f \rangle / \langle Q \rangle$ can quantify the importance of this mechanism.

In our results, the proportion of runoff generated by Dunne overland flow is almost entirely explained by the mean topographic variance of the watershed. Figure 11B shows

$\langle Q_f \rangle / \langle Q \rangle$ versus the mean topographic variance $\overline{Z}/h_g$. A clear mapping is shown between model runs that have gentle topography (low $\overline{Z}$) and those that generate runoff via Dunne overland flow. Figure 11C shows the same results, but colored to show the parameters. All cases are humid (Ai = 0.5), but have a range of values for the other parameters discussed in this paper. The most consistent pattern is that low γ cases tend to produce more quickflow. The storage index σ is a secondary control, with generally gentle topography and more Dunne overland flow produced when σ is small, provided that γ is not too large. Low β cases are the most likely to break expectations, which is expected given their tendency to evolve unique features like non-dendritic drainage networks and wide valley bottoms.

In the Dunne Diagram framework, Dunne overland flow is associated with moderate to poorly drained soils and low relief, gentle topography. In our model, poorly drained soils (relative to climate forcing) *produce* the associated gentle topography through water erosion to maintain the balance discussed in Section 6.1. The same can be said in the reverse direction. Well-drained soils produce steeper (higher mean variance) topography by expanding the zone where overland flow and water erosion do not occur, and therefore they develop a hydrological response dominated by subsurface flow (baseflow) rather than Dunne overland flow.

These results convey some information about the variably saturated area (shown in colors); however, close inspection of Figure 11B shows that the relationship between quickflow fraction and variably saturated area is not monotonically increasing. This is expected, because permanently saturated areas also can generate Dunne overland flow. However, variably saturated areas are distinct as an expression of the transition zone between areas of recharge and discharge, between diffusive transport and perennial water erosion. Could there be unique controls on variably saturated extent that are not captured in Figure 11?

The answer to this question may lie in connection to the hillslope number. In Section 4, we discussed how Litwin et al. (2021) called $\beta = h_g/h_a$ the hillslope number, which is defined as hillslope relief divided by the aquifer thickness. However the relief and mean aquifer thickness are emergent products of our coevolving system that we cannot specify ahead of time. We found that the actual emergent hillslope number has some bearing on the extent of variably saturated areas.

Before plotting the hillslope number, we first plotted the proportion of the domain classified as variably saturated against the dimensionless mean topographic variance (Figure 12A). The pattern is similar to that shown in Figure 11B, but with more scatter. The scatter shows greater difference in topographic variance between model runs that have the same variably saturated area but different σ (among other factors).

Dividing mean topographic variance by the actual mean aquifer thickness $\langle h \rangle$ rather than the characteristic height scale h_g gives an estimate of the emergent hillslope number, $\bar{Z}/\langle h \rangle$, on the y-axis. Figure 12B shows that this produces three tight relationships, separated by differences in aquifer relief index β. The hillslope numbers that we observe for the high β case are within the range described by Lyon and Troch (2007), who calculated hillslope numbers in the range of 18–96 for several real sites, although this will be sensitive to exactly how the relief is defined.

The importance of β in Figure 12B is expected given its role as a type of characteristic hillslope number based on model parameters. By normalizing the hillslope number with β we obtain a relationship (Figure 12C) that is tighter than the original between variably saturated are and topographic variance (Figure 12A). This indicates that there is a trade-off between the hillslope number and the proportion that is variably saturated: larger normalized hillslope numbers, which are associated with thin aquifers relative to relief, emerge with smaller variably saturated areas; thicker aquifers relative to relief emerge with greater variably saturated areas. The hillslope number has proved to be a useful concept to understand hydrologic response (Lyon & Troch, 2007), and here reveals a connection with emergent landscape features that to our knowledge, has not been shown before. We will not attempt to explain why this relationship exists here, but it certainly demonstrates that there are rich and largely unexplored avenues of research in emergent hydrogeomorphic dynamics.

6.7 Does coevolution explain Freeze's observation about the prevalence of Dunne overland flow?

Freeze (1980) observed a "delicate hydrologic balance on a hillslope" where only narrow combinations of parameters produced Dunne overland flow, despite the prevalence of Dunne overland flow in nature and the wide plausible ranges of parameter values. This led Freeze to hypothesize that there is a "very close relationship between climate, hydraulic conductivity, and the development of geomorphic landforms," in nature that tends to produce runoff as Dunne overland flow. We have also suggested that there is delicate balance in landscapes. However, within the scope of the processes in DupuitLEM, we did not see a tendency toward Dunne overland flow. Instead at geomorphic dynamic equilibrium water is partitioned to maintain balance between the size of recharge and discharge areas (Section 6.1). Consequently, coevolution reinforces the associations described by the Dunne diagram: places with thick, highly permeable soils evolve steep topography and subsurface-dominated runoff generation, whereas places with thinner less permeable soils evolve gentler topography and more Dunne overland flow (Section 6.6).

However, this does not indicate that these results represent conclusive evidence against Freeze's hypothesis. Although we explored the role of coevolving topography ("geomorphic landforms"), we selected climate and subsurface properties as parameters. The potential coevolution of these parameters is not accounted for. The transmissivity is a notable example of this. Li et al. (2014) broadened the exploration begun by Freeze (1980) and found evidence that indicates coevolution *between* subsurface properties and climate is important. They conducted a comprehensive study of the prevalence of Hortonian overland flow, Dunne overland flow, and subsurface stormflow using a suite of synthetic watersheds where climate, subsurface parameters, and topographic relief were varied independently. Runoff behavior varied widely with model parameters, and many runs did not conform to the Dunne diagram (e.g., arid climate with predominantly Dunne overland flow). Considering only model runs where the partitioning between ET and discharge was close to the empirical Budyko curve provided a behavioral constraint on the water balance that eliminated many, but not all, of the model runs that did not conform to the Dunne diagram. Although the tendency of watersheds to fall close to the Budyko curve is not fully understood, it has been associated with coevolution between soil, vegetation, and climate (Troch et al., 2013).

Our study indicates that hydrogeomorphic constraints could complement the Budyko water balance constraint. When Li et al. (2014) varied topography in their synthetic watersheds, they stretched the vertical dimension of a digital elevation model, effectively decoupling catchment morphology from other attributes, as they intended. Although the Budyko constraint eliminated some of the unrealistic runoff behavior by invoking the coevolution of climate, subsurface properties, and vegetation, Li et al. (2014) did not have an equivalent way to remove unrealistic behavior due to the relationship between climate, subsurface properties, and topography. Perhaps something like Equation (24) that relates transmissivity and climate to source area size and convergence, or the relationship between relief and quickflow fraction in Figure 11 could be used to provide a hydrogeomorphic behavioral constraint, and eliminate even more model runs that deviated from the Dunne diagram in Li et al. (2014). Such a constraint would need to be grounded in field evidence, but could use relationships derived from our simulations as plausible hypotheses. Although this is interesting in a theoretical sense, it could also be useful for constraining parameters in large-scale predictive models, where the appropriate values of subsurface parameters are unknown and difficult to measure.

7 Conclusions

Landscape evolution models are powerful tools for understanding the surface processes, acting as testing grounds for theories about how tectonics, climate, and lithology affect geomorphic features we observe today. Hydrology is often the glue that links these forcings and features together, as water is a powerful and ubiquitous agent for transporting solid and dissolved material from headwaters to depocenters. Here we have shown that LEMs have the potential to provide insights into the emergence of hydrological processes as well, provided the mechanisms underlying those processes are resolved in sufficient detail.

We have shown just one potential avenue for using an LEM to answer hydrological questions, in which runoff from shallow groundwater and precipitation on saturated areas provides the shear stress for detachment-limited erosion. Within this scope, we have revealed complex interactions between topography, aquifer properties, and hydrologic function, including water balance partitioning, patterns of recharge and saturated areas, and the emergence of variable source area runoff generation. Most importantly, we found that:

1. Drainage dissection increases not only with decreasing drainage capacity, as shown by (Litwin et al., 2021), but also with hydroclimatic properties including the subsurface storage capacity relative to storm depth and the aridity index.
2. When aquifers are thick relative to relief, it is possible to generate topographic features that are uncharacteristic of the streampower-diffusion LEM, including wide valley bottoms and nondendritic drainage networks.
3. In emergent landscapes, the relationship between saturated area and baseflow has a distinct bend: saturated area increases gradually with baseflow until the channel network is saturated, at which point saturated area increases rapidly across unchannelized areas with baseflow.
4. During evolution from a flat initial condition toward dynamic equilibrium, hydraulic gradients increase, which reduces the saturated area and flashiness of discharge.
5. At dynamic equilibrium, the size of the diffusion-dominated uplands that saturate very infrequently and supply recharge balances with the size of the lowlands that remain saturated and experience persistent water erosion.
6. The relationships between hydrology and geomorphology on the humid side of the Dunne Diagram, in which landscapes with deep soil and steep topography are associated with subsurface stormflow, and gentle topography and poorly drained soils are associated with saturation excess overland flow, can emerge as a result of coevolution.

This study lays the foundations for future work in which LEMs can be used to ask hydrological questions, and dynamic hydrological processes are given more consideration in spatially resolved landscape evolution models.

8 Notation

Variable definitions are below, with dimensions length L, time T, and mass M. Prime always indicates the dimensionless equivalent, where dimensionless equivalents are defined in the text.

variable	name	dimension
x, y	horizontal coordinates	[L]
t	time	[T]
$z(x, y, t)$	topographic elevation	[L]
$d(x, y)$	depth below surface	[L]
$h(x, y, t)$	aquifer thickness	[L]
$S_d(d, t)$	unsaturated storage below depth d	[L]
$A(x, y, t)$	area upslope	[L^2]
$a(x, y, t)$	area upslope per unit contour width	[L]
$\theta(x, y, t)$	aquifer base slope angle	[rad]
h_g	characteristic geomorphic height scale	[L]
ℓ_g	characteristic geomorphic length scale	[L]
t_g	characteristic geomorphic time scale	[T]
h_a	characteristic aquifer thickness	[L]
t_d	characteristic time to drain aquifer storage	[T]
l	domain side length	[L]
α	characteristic gradient	[-]
β	aquifer relief scale	[-]
γ	drainage capacity	[-]
δ	timescale factor	[-]
λ	domain scale factor	[-]
σ	water storage index	[-]
ρ	precipitation steadiness index	[-]
Ai	aridity index	[-]
ϕ	moisture content index	[-]
E_f	fluvial incision rate	[L/T]
E_h	hillslope diffusion rate	[L/T]
E_0	streampower threshold	[L/T]
S_c	critical slope	[-]
U	uplift rate	[L/T]
K	streampower incision coefficient	[1/T]
v_0	characteristic contour width	[L]
b	permeable thickness	[L]
q_h	hillslope sediment transport rate	[L^2/T]
D	hillslope diffusivity	[L^2/T]
k_{sf}	timestep scaling factor	[-]
$R_d(d, t)$	recharge for water table at depth d	[L]
$r(x, y, t)$	recharge rate	[L/T]
$q(x, y, t)$	groundwater specific-discharge	[L^2/T]
$q_s(x, y, t)$	local surface runoff	[L/T]
$Q(x, y, t)$	discharge	[L^3/T]
$Q^*(x, y, t)$	dimensionless discharge	[-]
p	average precipitation rate	[L/T]
pet	interstorm potential evapotranspiration rate	[L/T]
d_s	storm depth	[L]
t_r	storm duration	[T]
t_b	interstorm duration	[T]
i	precipitation intensity	[L/T]
k_s	hydraulic conductivity	[L/T]
n_e	drainable porosity	[-]
n_a	plant-available water content	[-]
$\mathcal{G}$	step function	
$\mathcal{R}$	ramp function	

cont.

variable	name	dimension
$\langle PET \rangle$	long-term average potential evapotranspiration rate	[L^3/T]
$\langle AET \rangle$	long-term average actual evapotranspiration rate	[L^3/T]
$\langle P \rangle$	long-term average precipitation rate	[L^3/T]
$\langle R \rangle$	long-term average recharge rate	[L^3/T]
$\langle Q_b \rangle$	long-term average baseflow discharge	[L^3/T]
$\langle Q_f \rangle$	long-term average quickflow discharge	[L^3/T]
$Q_b(t)$	baseflow discharge for model domain	[L^3/T]
$Q_b^*(t)$	dimensionless baseflow discharge for model domain	[-]
$S(t)$	model domain saturated storage	[L^3]
$S^*(t)$	dimensionless model domain saturated storage	[$-$]
A_{tot}	model domain area	[L^2]
$A_{sat}(t)$	area saturated	[L^2]
$A^*_{sat}(t)$	dimensionless area saturated	[-]

Appendices

A Nondimensionalization of landscape evolution with nonlinear diffusion

Litwin et al. (2021) nondimensionalized the landscape evolution equation using the concept of symmetry groups. Here we modify that nondimensionalization to include nonlinear hillslope diffusion (Equation (4)) rather than linear diffusion. We begin by replacing the dimensioned model parameters with equivalent combinations of the characteristic scales:

$$\frac{\partial z}{\partial t} = -\frac{\sqrt{v_0}}{t_g}\langle Q^* \rangle \sqrt{a}|\nabla z| + \frac{\ell_g^2}{t_g}\nabla \cdot \left(\nabla z \left(1 + (|\nabla z|/S_c)^2\right)\right) + \frac{h_g}{t_g} \tag{A1}$$

$$-\nabla \cdot \left(a \frac{\nabla z}{|\nabla z|}\right) = 1 \tag{A2}$$

The hydrological equations are:

$$\frac{\partial h}{\partial t} = \frac{h_a}{t_d}\left(\frac{r}{p} - \frac{\nabla \cdot q}{p} - \frac{q_s}{p}\right) \tag{A3}$$

$$\frac{q}{p} = -h\cos^2(\arctan|\nabla z|)\frac{\ell_g^2}{h_g h_a}\left(\nabla h + \nabla z\right) \tag{A4}$$

$$\frac{q_s}{p} = \mathcal{G}\left(\frac{h}{b}\right)\mathcal{R}\left(\frac{r}{p} - \frac{\nabla \cdot q}{p}\right) \tag{A5}$$

$$Q^* = \frac{1}{Ap}\int_A q_s dA_c \tag{A6}$$

We now seek to identify sets of parameters that can be scaled by a constant factor 'c' while leaving the equations unchanged. See Litwin et al. (2021) for a detailed explanation of this approach. We find that the same two groups of parameters used previously for the DupuitLEM model can again be used:

$$\begin{aligned} &\{t \to ct, t_g \to ct_g, t_d \to ct_d\} \\ &\{x \to cx, y \to cy, a \to ca, A \to c^2 A, l_g \to cl_g, \\ &\quad q \to cq, z \to cz, h \to ch, h_g \to ch_g, h_a \to ch_a, b \to cb\} \end{aligned} \tag{A7}$$

B Nondimensionalization of Schenk Vadose Model

For simplicity of notation, we begin by rewriting governing equation of Schenk (2008) (equation (11)) with the following simplifications: $S(d,t) \to S_d$, $S(d,t{+}\Delta t){-}S(d,t) \to \Delta S_d$, $i(t)\Delta t \to I$, and $e(t)\Delta t \to PET$.

$$\Delta S_d = \min\left(dn_a - S_d, I\right) - \min\left(S_d, PET\right) \tag{A8}$$

Now we introduce the dimensionless variables:

$$\begin{aligned} d &= d'b && \text{(A9)}\\ S_d &= S_d' p(\langle t_r\rangle + \langle t_r\rangle) && \text{(A10)}\\ \Delta S_d &= \Delta S_d' p(\langle t_r\rangle + \langle t_r\rangle) && \text{(A11)}\\ I &= I' p(\langle t_r\rangle + \langle t_r\rangle) && \text{(A12)}\\ PET &= PET' pet\langle t_r\rangle && \text{(A13)} \end{aligned}$$

where the prime indicates a dimensionless equivalent quantity. Substitution yields the following:

$$\Delta S_d' = \min\left(\frac{d'bn_a}{p(\langle t_r\rangle + \langle t_r\rangle)} - S_d', I'\right) - \min\left(S_d', PET'\frac{pet\langle t_r\rangle}{p(\langle t_r\rangle + \langle t_r\rangle)}\right). \tag{A14}$$

We rewrite this as:

$$\Delta S_d' = \min\left(d'\sigma\phi - S_d', I'\right) - \min\left(S_d', PET'\mathrm{Ai}\right) \tag{A15}$$

where:

$$\begin{aligned} \sigma &= \frac{bn_e}{p\left(\langle t_r\rangle + \langle t_b\rangle\right)} && \text{Water storage index} && \text{(A16)}\\ \mathrm{Ai} &= \frac{pet\langle t_b\rangle}{p\left(\langle t_r\rangle + \langle t_b\rangle\right)} && \text{Aridity index} && \text{(A17)}\\ \phi &= n_a/n_e && \text{Moisture content index} && \text{(A18)} \end{aligned}$$

In order to uniquely determine the mean storm duration and interstorm duration (Equations (8) and (9)), we introduce one final parameter:

$$\rho = \frac{\langle t_r\rangle}{\langle t_r\rangle + \langle t_b\rangle} \qquad \text{Precipitation steadiness index} \tag{A19}$$

Likewise, the simplified expression for storm recharge R (equation (12)) is:

$$R_d = I - \min\left(dn_a - S_d, I\right) \tag{A20}$$

and the equivalent dimensionless form is:

$$R_d' = I' - \min\left(\frac{d'bn_a}{p(\langle t_r\rangle + \langle t_r\rangle)} - S_d', I'\right) \tag{A21}$$

where $R_d = R_d' p(\langle t_r\rangle + \langle t_r\rangle)$. When the dimensionless parameter definitions are substituted, this becomes:

$$R_d' = I' - \min\left(d'\sigma\phi - S_d', I'\right). \tag{A22}$$

9 Open Research

No original data are presented in this paper. The Python package DupuitLEM v1.1 (Litwin et al., 2023a) contains the models and scripts used to generate and post-process the model output. All model output are archived on Zenodo (Litwin et al., 2023b). Landlab v2.0 (Barnhart et al., 2020) is a core dependency of DupuitLEM. The complete list of input parameter values can be found in Table S1 of Supporting Information S1, and in the model output archive.

Acknowledgments

This work was supported by National Science Foundation grants EAR-2012264, EAR-1654194, ACI-1450409, EAR-1725774, and EAR-1831623. Model simulations were carried out at the Advanced Research Computing at Hopkins (ARCH) core facility (rockfish.jhu.edu), which is supported by the National Science Foundation (NSF) grant number OAC-1920103. Any use of trade, firm, or product names is for descriptive purposes only and does not imply endorsement by the U.S. Government.

References

Abrams, D. M., Lobkovsky, A. E., Petroff, A. P., Straub, K. M., McElroy, B., Mohrig, D. C., … Rothman, D. H. (2009). Growth laws for channel networks incised by groundwater flow. *Nature Geoscience*, *2*(3), 193–196. doi: 10.1038/ngeo432

Ambroise, B. (1986). Rôle hydrologique des surfaces saturées en eau dans le bassin de Ringelbach à Soultzeren (Hautes Vosges, France). In *Colloque scientifique des Universités du Rhin supérieur «Recherches sur l'environnement dans la région». 1* (pp. 619–630).

Anand, S. K., Bonetti, S., Camporeale, C., Hooshyar, M., & Porporato, A. (2022). Comment on "Groundwater affects the geomorphic and hydrologic properties of coevolved landscapes" by Litwin et al. *Journal of Geophysical Research: Earth Surface*, *127*(10), e2022JF006669. doi: https://doi.org/10.1029/2022JF006669

Anderson, R. S., Anderson, S. P., & Tucker, G. E. (2013). Rock damage and regolith transport by frost: An example of climate modulation of the geomorphology of the critical zone. *Earth Surface Processes and Landforms*, *38*(3), 299–316. doi: 10.1002/esp.3330

Anderson, R. S., Rajaram, H., & Anderson, S. P. (2019). Climate driven coevolution of weathering profiles and hillslope topography generates dramatic differences in critical zone architecture. *Hydrological Processes*, *33*(1), 4–19. doi: 10.1002/hyp.13307

Andrews, D. J., & Bucknam, R. C. (1987). Fitting degradation of shoreline scarps by a nonlinear diffusion model. *Journal of Geophysical Research*, *92*(B12), 12857–12867.

Barenblatt, G. I. (1996). *Scaling, self-similarity, and intermediate asymptotics* (No. 14). Cambridge; New York: Cambridge University Press.

Barnhart, K. R., Glade, R. C., Shobe, C. M., & Tucker, G. E. (2018). Terrainbento 1.0: A Python package for multi-model analysis in long-term drainage basin evolution. *Geoscientific Model Development Discussions*(October), 1–57. doi: 10.5194/gmd-2018-204

Barnhart, K. R., Hutton, E. W. H., Tucker, G. E., Gasparini, N. M., Istanbulluoglu, E., Hobley, D. E. J., … Bandaragoda, C. (2020). Short communication: Landlab v2.0: A software package for Earth surface dynamics. *Earth Surface Dynamics*, *8*(2), 379–397. doi: 10.5194/esurf-8-379-2020

Bishop, P. (2007). Long-term landscape evolution: Linking tectonics and surface processes. *Earth Surface Processes and Landforms*, *32*(3), 329–365. doi: 10.1002/esp.1493

Bonetti, S., Bragg, A. D., & Porporato, A. (2018). On the theory of drainage area for regular and non-regular points. *Proceedings of the Royal Society A:*

Mathematical, Physical and Engineering Sciences, *474*(2211), 20170693. doi: 10.1098/rspa.2017.0693

Bonetti, S., Hooshyar, M., Camporeale, C., & Porporato, A. (2020). Channelization cascade in landscape evolution. *Proceedings of the National Academy of Sciences*, *117*(3), 1375–1382. doi: 10.1073/pnas.1911817117

Botter, G., Porporato, A., Rodriguez-Iturbe, I., & Rinaldo, A. (2007). Basin-scale soil moisture dynamics and the probabilistic characterization of carrier hydrologic flows: Slow, leaching-prone components of the hydrologic response. *Water Resources Research*, *43*(2), 1–14. doi: 10.1029/2006WR005043

Brantley, S. L., Eissenstat, D. M., Marshall, J. A., Godsey, S. E., Balogh-Brunstad, Z., Karwan, D. L., ... Weathers, K. C. (2017). Reviews and syntheses: On the roles trees play in building and plumbing the critical zone. *Biogeosciences*, *14*(22), 5115–5142. doi: 10.5194/bg-14-5115-2017

Brantley, S. L., Lebedeva, M. I., Balashov, V. N., Singha, K., Sullivan, P. L., & Stinchcomb, G. (2017). Toward a conceptual model relating chemical reaction fronts to water flow paths in hills. *Geomorphology*, *277*, 100–117. doi: 10.1016/j.geomorph.2016.09.027

Braun, J., & Willett, S. D. (2013). A very efficient O(n), implicit and parallel method to solve the stream power equation governing fluvial incision and landscape evolution. *Geomorphology*, *180–181*, 170–179. doi: 10.1016/j.geomorph.2012.10.008

Bresciani, E., Davy, P., & de Dreuzy, J. R. (2014). Is the Dupuit assumption suitable for predicting the groundwater seepage area in hillslopes? *Water Resources Research*, *50*(3), 2394–2406. doi: 10.1002/2013WR014284

Brutsaert, W. (2005). *Hydrology: An introduction.* Cambridge; New York: Cambridge University Press.

Budyko, M. I. (1974). *Climate and life* (No. 18). New York: Academic Press.

Callahan, R. P., Ferrier, K. L., Dixon, J., Dosseto, A., Hahm, W. J., Jessup, B. S., ... Riebe, C. S. (2019). Arrested development: Erosional equilibrium in the southern Sierra Nevada, California, maintained by feedbacks between channel incision and hillslope sediment production. *GSA Bulletin*, *131*(7-8), 1179–1202. doi: 10.1130/B35006.1

Campbell Grant, E. H., Lowe, W. H., & Fagan, W. F. (2007). Living in the branches: Population dynamics and ecological processes in dendritic networks. *Ecology Letters*, *10*(2), 165–175. doi: 10.1111/j.1461-0248.2006.01007.x

Chen, A., Darbon, J., & Morel, J.-M. (2014). Landscape evolution models: A review of their fundamental equations. *Geomorphology*, *219*, 68–86. doi: 10.1016/j.geomorph.2014.04.037

Childs, E. C. (1971). Drainage of groundwater resting on a sloping bed. *Water Resources Research*, *7*(5), 1256–1263. doi: 10.1029/WR007i005p01256

Crosbie, R. S., Binning, P., & Kalma, J. D. (2005). A time series approach to inferring groundwater recharge using the water table fluctuation method. *Water Resources Research*, *41*(1). doi: 10.1029/2004WR003077

Cullen, C., Anders, A. M., Lai, J., & Druhan, J. L. (2022). Numerical modeling of groundwater-driven stream network evolution in low-relief post-glacial landscapes. *Earth Surface Processes and Landforms*, *47*(2), 658–671. doi: 10.1002/esp.5278

Davis, W. M. (1899). The geographical cycle. *The Geographical Journal*, *14*(5), 481–504. doi: 10.2307/1774538

Deal, E., Braun, J., & Botter, G. (2018). Understanding the role of rainfall and hydrology in determining fluvial erosion efficiency. *Journal of Geophysical Research: Earth Surface*, *123*(4), 744–778. doi: 10.1002/2017JF004393

Dietrich, W. E., Bellugi, D. G., Sklar, L. S., Stock, J. D., Heimsath, A. M., & Roering, J. J. (2003). Geomorphic transport laws for predicting landscape form and dynamics. In P. R. Wilcock & R. M. Iverson (Eds.), *Geophysical Monograph*

Series (pp. 103–132). Washington, D.C.: American Geophysical Union. doi: 10.1029/135GM09

Doane, T. H., Furbish, D. J., Roering, J. J., Schumer, R., & Morgan, D. J. (2018). Nonlocal sediment transport on steep lateral moraines, eastern Sierra Nevada, California, USA. *Journal of Geophysical Research: Earth Surface*, *123*(1), 187–208. doi: 10.1002/2017JF004325

Dunne, T. (1978). Field studies of hillslope flow processes. In M. J. Kirkby (Ed.), *Hillslope hydrology.* Chichester; New York: Wiley.

Dunne, T., & Black, R. D. (1970). Partial area contributions to storm runoff in a small New England watershed. *Water Resources Research*, *6*(5), 1296–1311. doi: 10.1029/WR006i005p01296

Dunne, T., Moore, T., & Taylor, C. H. (1975). Recognition and prediction of runoff-producing zones in humid regions. *Hydrol. Sci. Bull*, *20*(3), 305–327.

Eagleson, P. (1978). Introduction to water balance dynamics. *Water Resources Research*, *14*(5), 705–712. doi: 10.1016/j.compchemeng.2012.11.011

Freeze, R. A. (1980). A stochastic-conceptual analysis of rainfall-runoff processes on a hillslope. *Water Resources Research*, *16*(2), 391–408. doi: 10.1029/WR016i002p00391

Gabet, E. J. (2003). Sediment transport by dry ravel. *Journal of Geophysical Research: Solid Earth*, *108*(B1). doi: 10.1029/2001JB001686

Ganti, V., Passalacqua, P., & Foufoula-Georgiou, E. (2012). A sub-grid scale closure for nonlinear hillslope sediment transport models. *Journal of Geophysical Research: Earth Surface*, *117*(F2). doi: 10.1029/2011JF002181

Gillham, R. W. (1984). The capillary fringe and its effect on water-table response. *Journal of Hydrology*, *67*(1), 307–324. doi: 10.1016/0022-1694(84)90248-8

Godard, V., & Tucker, G. E. (2021). Influence of climate-forcing frequency on hillslope response. *Geophysical Research Letters*, *48*(18), e2021GL094305. doi: 10.1029/2021GL094305

Haitjema, H. M., & Mitchell-Bruker, S. (2005). Are water tables a subdued replica of the topography? *Groundwater*, *43*(6), 781–786. doi: 10.1111/j.1745-6584.2005.00090.x

Hare, D. K., Helton, A. M., Johnson, Z. C., Lane, J. W., & Briggs, M. A. (2021). Continental-scale analysis of shallow and deep groundwater contributions to streams. *Nature Communications*, *12*(1), 1450. doi: 10.1038/s41467-021-21651-0

Harman, C. J., & Cosans, C. L. (2019). A low-dimensional model of bedrock weathering and lateral flow coevolution in hillslopes: 2. Controls on weathering and permeability profiles, drainage hydraulics, and solute export pathways. *Hydrological Processes*(December 2018), 1168–1190. doi: 10.1002/hyp.13385

Harman, C. J., & Troch, P. A. (2014). What makes Darwinian hydrology "Darwinian"? Asking a different kind of question about landscapes. *Hydrology and Earth System Sciences*, *18*(2), 417–433. doi: 10.5194/hess-18-417-2014

Hewlett, J. D., & Hibbert, A. R. (1967). Factors affecting the response of small watersheds to precipitation in humid areas. In *Int. Symp. Forest Hydrology.* doi: 10.1177/0309133309338118

Hobley, D. E. J., Adams, J. M., Nudurupati, S. S., Hutton, E. W. H., Gasparini, N. M., Istanbulluoglu, E., & Tucker, G. E. (2017). Creative computing with Landlab: An open-source toolkit for building, coupling, and exploring two-dimensional numerical models of Earth-surface dynamics. *Earth Surface Dynamics*, *5*(1), 21–46. doi: 10.5194/esurf-5-21-2017

Horton, R. E. (1933). The role of infiltration in the hydrologic cycle. *Eos, Transactions American Geophysical Union*. doi: 10.1029/TR014i001p00446

Huang, X., & Niemann, J. D. (2006). Modelling the potential impacts of groundwater hydrology on long-term drainage basin evolution. *Earth Surface Processes and Landforms*. doi: 10.1002/esp.1369

Huang, X., & Niemann, J. D. (2008). How do streamflow generation mechanisms affect watershed hypsometry? *Earth Surface Processes and Landforms*. doi: 10.1002/esp.1573

Ijjász-Vásquez, E. J., Bras, R. L., & Moglen, G. E. (1992). Sensitivity of a basin evolution model to the nature of runoff production and to initial conditions. *Water Resources Research*. doi: 10.1029/92WR01561

Jefferson, A., Grant, G. E., Lewis, S. L., & Lancaster, S. T. (2010). Coevolution of hydrology and topography on a basalt landscape in the Oregon Cascade Range, USA. *Earth Surface Processes and Landforms*, *35*(7), 803–816. doi: 10.1002/esp.1976

Jensen, C. K., McGuire, K. J., & Prince, P. S. (2017). Headwater stream length dynamics across four physiographic provinces of the Appalachian Highlands. *Hydrological Processes*, *31*(19), 3350–3363. doi: 10.1002/hyp.11259

Lague, D., Hovius, N., & Davy, P. (2005). Discharge, discharge variability, and the bedrock channel profile. *Journal of Geophysical Research: Earth Surface*, *110*(F4). doi: 10.1029/2004JF000259

Laity, J. E., & Malin, M. C. (1985). Sapping processes and the development of theater-headed valley networks on the Colorado Plateau. *Geological Society of America Bulletin*, *96*, 203–217.

Langston, A. L., & Tucker, G. E. (2018). Developing and exploring a theory for the lateral erosion of bedrock channels for use in landscape evolution models. *Earth Surface Dynamics*, *6*(1), 1–27. doi: 10.5194/esurf-6-1-2018

Lapides, D. A., David, C., Sytsma, A., Dralle, D., & Thompson, S. (2020). Analytical solutions to runoff on hillslopes with curvature: Numerical and laboratory verification. *Hydrological Processes*, hyp.13879. doi: 10.1002/hyp.13879

Latron, J. (1990). Caractérisation géomorphologique et hydrologique du bassin versant versant du Strengbach (Aubure). *Université Louis Pasteur, Strasbourg I*.

Latron, J., & Gallart, F. (2007). Seasonal dynamics of runoff-contributing areas in a small mediterranean research catchment (Vallcebre, Eastern Pyrenees). *Journal of Hydrology*, *335*(1), 194–206. doi: 10.1016/j.jhydrol.2006.11.012

Li, H. Y., Sivapalan, M., Tian, F., & Harman, C. J. (2014). Functional approach to exploring climatic and landscape controls of runoff generation: 1. Behavioral constraints on runoff volume. *Water Resources Research*. doi: 10.1002/2014WR016307

Litwin, D. G., Barnhart, K. R., Tucker, G. E., & Harman, C. J. (2023a). *DupuitLEM: groundwater landscape evolution with landlab.* Zenodo. doi: 10.5281/zenodo.7620978

Litwin, D. G., Barnhart, K. R., Tucker, G. E., & Harman, C. J. (2023b). *Model output for "Catchment coevolution and the geomorphic origins of variable source area hydrology".* Zenodo. doi: 10.5281/zenodo.7621354

Litwin, D. G., Tucker, G., Barnhart, K., & Harman, C. J. (2020). GroundwaterDupuitPercolator: A Landlab component for groundwater flow. *Journal of Open Source Software*, *5*(46), 1935. doi: 10.21105/joss.01935

Litwin, D. G., Tucker, G. E., Barnhart, K. R., & Harman, C. J. (2021). Groundwater affects the geomorphic and hydrologic properties of coevolved landscapes. *Journal of Geophysical Research: Earth Surface*, *127*, e2021JF006239. doi: 10.1029/2021JF006239

Litwin, D. G., Tucker, G. E., Barnhart, K. R., & Harman, C. J. (2022). Reply to comment by Anand et al. on "Groundwater affects the geomorphic and hydrologic properties of coevolved landscapes". *Journal of Geophysical Research: Earth Surface*, *127*(10), e2022JF006722. doi: 10.1029/2022JF006722

Luijendijk, E. (2022). Transmissivity and groundwater flow exert a strong influence on drainage density. *Earth Surface Dynamics*, *10*(1), 1–22. doi: 10.5194/esurf-10-1-2022

L'vovich. (1979). *World Water Resources and their Future* (First ed.). American

Geophysical Union (AGU). doi: 10.1029/SP013

Lyon, S. W., & Troch, P. A. (2007). Hillslope subsurface flow similarity: Real-world tests of the hillslope Péclet number. *Water Resources Research*, *43*(7). doi: 10.1029/2006WR005323

Marçais, J., de Dreuzy, J. R., & Erhel, J. (2017). Dynamic coupling of subsurface and seepage flows solved within a regularized partition formulation. *Advances in Water Resources*, *109*, 94–105. doi: 10.1016/j.advwatres.2017.09.008

McMillan, H. (2020). Linking hydrologic signatures to hydrologic processes: A review. *Hydrological Processes*, *34*(6), 1393–1409. doi: 10.1002/hyp.13632

Montgomery, D. R., & Dietrich, W. E. (1994). A physically based model for the topographic control on shallow landsliding. *Water Resources Research*, *30*(4), 1153–1171. doi: 10.1029/93WR02979

Myrabø, S. (1986). Runoff studies in a small catchment: Paper presented at the Nordic Hydrological Conference (Reykjavik, Iceland, August – 1986). *Hydrology Research*, *17*(4-5), 335–346. doi: 10.2166/nh.1986.0025

Ogden, F. L., Allen, M. B., Lai, W., Zhu, J., Seo, M., Douglas, C. C., & Talbot, C. A. (2017). The soil moisture velocity equation. *Journal of Advances in Modeling Earth Systems*, *9*(2), 1473–1487. doi: 10.1002/2017MS000931

O'Loughlin, E. M. (1981). Saturation regions in catchments and their relations to soil and topographic properties. *Journal of Hydrology*, *53*(3-4), 229–246. doi: 10.1016/0022-1694(81)90003-2

Pelletier, J. D. (2013). 2.3 Fundamental principles and techniques of landscape evolution modeling. In J. F. Shroder (Ed.), *Treatise on Geomorphology* (pp. 29–43). San Diego: Academic Press. doi: 10.1016/B978-0-12-374739-6.00025-7

Prancevic, J. P., & Kirchner, J. W. (2019). Topographic controls on the extension and retraction of flowing streams. *Geophysical Research Letters*, *46*, 2084–2092. doi: 10.1029/2018GL081799

Riebe, C. S., Hahm, W. J., & Brantley, S. L. (2017). Controls on deep critical zone architecture: A historical review and four testable hypotheses. *Earth Surface Processes and Landforms*, *42*(1), 128–156. doi: 10.1002/esp.4052

Rodriguez-Iturbe, I., Porporato, A., Ridolfi, L., Isham, V., Coxi, D. R., Society, T. R., & Sciences, E. (1999). Probabilistic modelling of water balance at a point: The role of climate, soil and vegetation. *Proceedings of the Royal Society of London.Series A: Mathematical, Physical and Engineering Sciences*, *455*(1990), 3789–3805. doi: 10.1098/rspa.1999.0477

Roering, J. J., Kirchner, J. W., & Dietrich, W. E. (1999). Evidence for nonlinear, diffusive sediment transport on hillslopes and implications for landscape morphology. *Water Resources Research*, *35*(3), 853–870. doi: 10.1029/1998WR900090

Roering, J. J., Kirchner, J. W., & Dietrich, W. E. (2001). Hillslope evolution by nonlinear, slope-dependent transport: Steady state morphology and equilibrium adjustment timescales. *Journal of Geophysical Research: Solid Earth*, *106*(B8), 16499–16513. doi: 10.1029/2001jb000323

Rosenbloom, N. A., & Anderson, R. S. (1994). Hillslope and channel evolution in a marine terraced landscape, Santa Cruz, California. *Journal of Geophysical Research: Solid Earth*, *99*(B7), 14013–14029. doi: 10.1029/94JB00048@10.1002/(ISSN)2169-9356.TECTOP1

Rossi, M. W., Whipple, K. X., & Vivoni, E. R. (2016). Precipitation and evapotranspiration controls on daily runoff variability in the contiguous United States and Puerto Rico. *Journal of Geophysical Research: Earth Surface*, *121*(1), 128–145. doi: 10.1002/2015JF003446

Sartz, R. S., Curtis, W. R., & Tolsted, D. N. (1977). Hydrology of small watersheds in Wisconsin's driftless area. *Water Resources Research*, *13*(3), 524–530. doi: 10.1029/WR013i003p00524

Schenk, H. J. (2008). The shallowest possible water extraction profile: A null model for global root distributions. *Vadose Zone Journal*, *7*(3), 1119–1124. doi: 10.2136/vzj2007.0119

Singha, K., & Navarre-Sitchler, A. (2022). The importance of groundwater in critical zone science. *Groundwater*, *60*(1), 27–34. doi: 10.1111/gwat.13143

St. Clair, J., Moon, S., Holbrook, W. S., Perron, J. T., Riebe, C. S., Martel, S. J., ... De Richter, D. B. (2015). Geophysical imaging reveals topographic stress control of bedrock weathering. *Science*, *350*(6260), 534–538. doi: 10.1126/science.aab2210

Theodoratos, N., Seybold, H., & Kirchner, J. W. (2018). Scaling and similarity of a stream-power incision and linear diffusion landscape evolution model. *Earth Surface Dynamics*, *6*(3), 779–808. doi: 10.5194/esurf-6-779-2018

Troch, P. A., Carrillo, G., Sivapalan, M., Wagener, T., & Sawicz, K. (2013). Climate-vegetation-soil interactions and long-term hydrologic partitioning: Signatures of catchment co-evolution. *Hydrology and Earth System Sciences*, *17*(6), 2209–2217. doi: 10.5194/hess-17-2209-2013

Troch, P. A., Lahmers, T., Meira, A., Mukherjee, R., Pedersen, J. W., Roy, T., & Valdes-Pineda, R. (2015). Catchment coevolution: A useful framework for improving predictions of hydrological change? *Water Resources Research*, *51*(7), 4903–4922. doi: 10.1002/2015WR017032

Troch, P. A., Paniconi, C., & Van Loon, E. E. (2003). Hillslope-storage Boussinesq model for subsurface flow and variable source areas along complex hillslopes: 1. Formulation and characteristic response. *Water Resources Research*, *39*(11). doi: 10.1029/2002WR001728

Tucker, G. E. (2004). Drainage basin sensitivity to tectonic and climatic forcing: Implications of a stochastic model for the role of entrainment and erosion thresholds. *Earth Surface Processes and Landforms*, *29*(2), 185–205. doi: 10.1002/esp.1020

Tucker, G. E., & Bradley, D. N. (2010). Trouble with diffusion: Reassessing hillslope erosion laws with a particle-based model. *Journal of Geophysical Research: Earth Surface*, *115*(F1). doi: 10.1029/2009JF001264

Tucker, G. E., & Bras, R. L. (1998). Hillslope processes, drainage density, and landscape morphology. *Water Resources Research*, *34*(10), 2751–2764. doi: 10.1029/98WR01474

Tucker, G. E., & Bras, R. L. (2000). A stochastic approach to modeling the role of rainfall variability in drainage basin evolution. *Water Resources Research*, *36*(7), 1953–1964. doi: 10.1029/2000WR900065

Tucker, G. E., & Hancock, G. R. (2010). Modelling landscape evolution. *Earth Surface Processes and Landforms*, *35*(1), 28–50. doi: 10.1002/esp.1952

Tucker, G. E., & Slingerland, R. (1997). Drainage basin responses to climate change. *Water Resources Research*, *33*(8), 2031–2047. doi: 10.1029/97WR00409

Valters, D. (2016). Modelling geomorphic systems: Landscape evolution. In *Geomorphological Techniques.* United Kingdom: British Society for Geomorphology. doi: 10.13140/RG.2.1.1970.9047

Wagener, T., Sivapalan, M., Troch, P., & Woods, R. (2007). Catchment classification and hydrologic similarity. *Geography Compass*, *1*(4), 901–931. doi: 10.1111/j.1749-8198.2007.00039.x

Wang, D., & Wu, L. (2013). Similarity of climate control on base flow and perennial stream density in the Budyko framework. *Hydrology and Earth System Sciences*, *17*(1), 315–324. doi: 10.5194/hess-17-315-2013

Warix, S. R., Godsey, S. E., Lohse, K. A., & Hale, R. L. (2021). Influence of groundwater and topography on stream drying in semi-arid headwater streams. *Hydrological Processes*, *35*(5), e14185. doi: 10.1002/hyp.14185

Weeks, E. P. (2002). The Lisse Effect revisited. *Groundwater*, *40*(6), 652–656. doi: 10.1111/j.1745-6584.2002.tb02552.x

Whipple, K. X. (2001). Fluvial landscape response time: How plausible is steady-state denudation? *American Journal of Science*, *301*(4-5), 313–325. doi: 10.2475/ajs.301.4-5.313

Willgoose, G. (2005). Mathematical modeling of whole landscape evolution. *Annual Review of Earth and Planetary Sciences*, *33*, 443–459.

Wu, S., Zhao, J., Wang, H., & Sivapalan, M. (2021). Regional patterns and physical controls of streamflow generation across the conterminous United States. *Water Resources Research*, *57*(6), e2020WR028086. doi: 10.1029/2020WR028086

Yokoo, Y., Sivapalan, M., & Oki, T. (2008). Investigating the roles of climate seasonality and landscape characteristics on mean annual and monthly water balances. *Journal of Hydrology*, *357*(3), 255–269. doi: 10.1016/j.jhydrol.2008.05.010

Yoshida, T., & Troch, P. A. (2016). Coevolution of volcanic catchments in Japan. *Hydrology and Earth System Sciences*, *20*(3), 1133–1150. doi: 10.5194/hess-20-1133-2016

Zhang, Y., Slingerland, R., & Duffy, C. (2016). Fully-coupled hydrologic processes for modeling landscape evolution. *Environmental Modelling and Software*, *82*, 89–107. doi: 10.1016/j.envsoft.2016.04.014

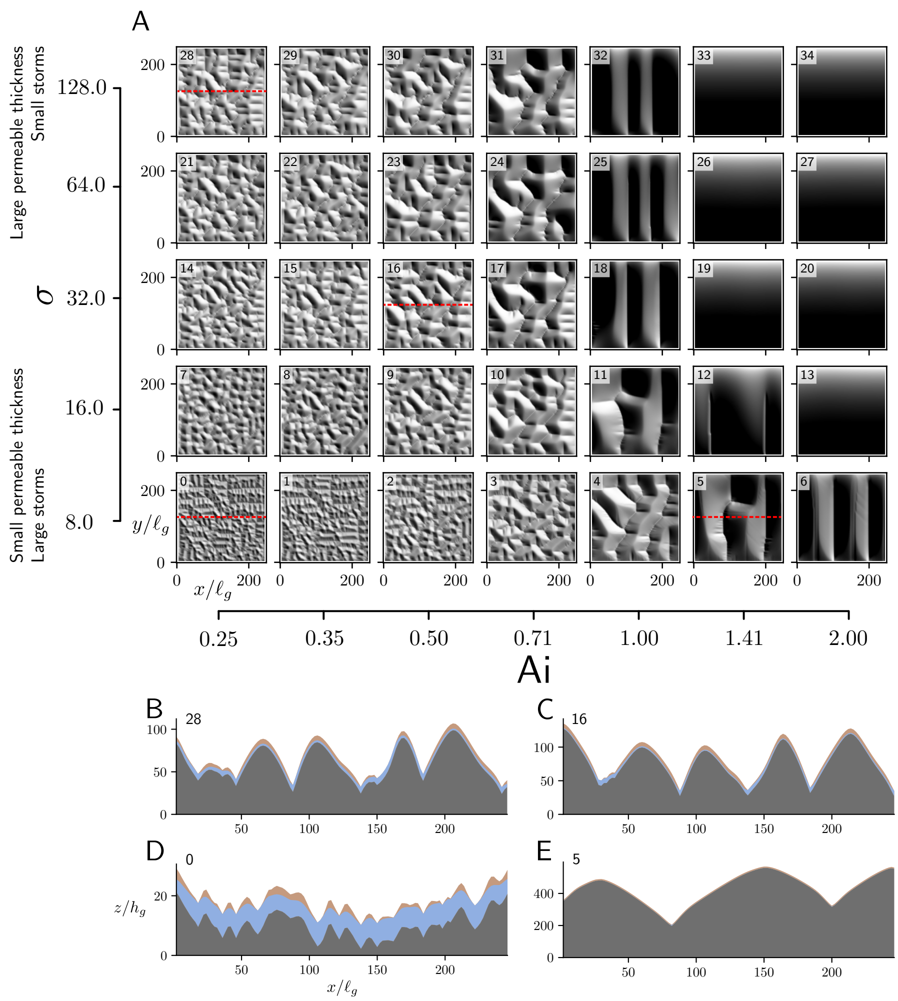

Figure 1. (A) Hillshades of modeled topography with varying aridity index Ai and water storage index σ, showing strong declines in dissection with increasing aridity, and a weaker positive relationship between dissection and σ. Here $\gamma = 4.0$, $\beta = 0.5$, $\rho = 0.03$, $\phi = 1.5$, $\alpha = 0.15$, $S_c = 0.5$, $\lambda = 250$, and $\delta = 2.0e-5$. The simulation numbers are in the upper left hand corner. Lower subplots (B–E) are lateral transects through topography along the red dashed lines for model runs corresponding to the small numbers on subplots in (A). Gray areas are impermeable bedrock, and brown areas are regolith, which is shown behind the mean aquifer thickness in light blue. Note differences in the vertical scale in B–E.

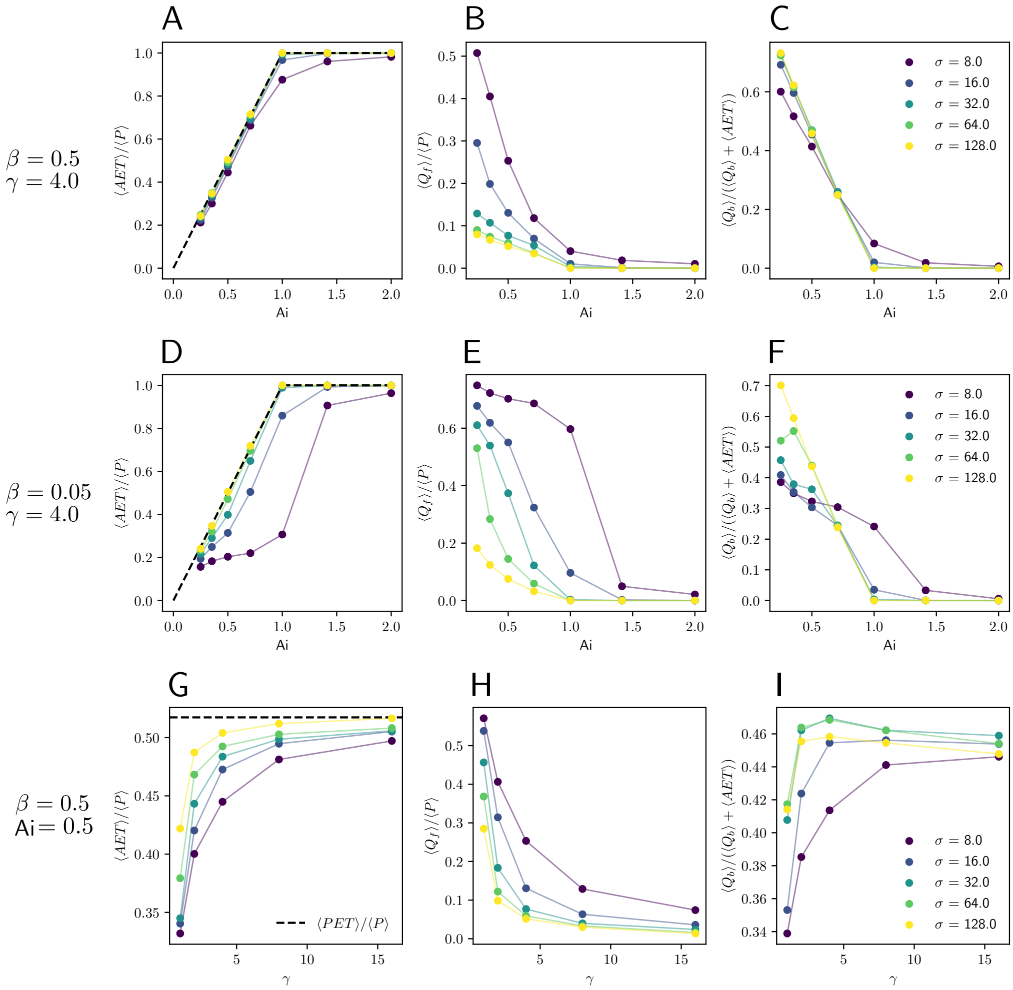

Figure 2. Water balance partitioning showing (A) Budyko-type plot, (B) the quickflow fraction of precipitation $\langle Q_f \rangle / \langle P \rangle$, and the baseflow fraction of storage, $\langle Q_b \rangle / (\langle Q_b \rangle + \langle AET \rangle)$ for the same simulations as in Figure 1. Storage is the amount of precipitation that does not become quickflow. (D–F) show the same partitioning as (A–C) above but for the model set with reduced aquifer relief scale $\beta = 0.05$ ($\gamma = 4.0$, $\rho = 0.03$, $\phi = 1.5$, $\alpha = 0.15$, $S_c = 0.5$, $\lambda = 250$, and $\delta = 2\text{e} - 4$). (G–I) show the same partitioning when the drainage capacity γ is varied while holding the aridity index constant at Ai $= 0.5$ ($\beta = 0.5$, $\rho = 0.03$, $\phi = 1.5$, $\alpha = 0.15$, $S_c = 0.5$, $\lambda = 250$, and $\delta = 2\text{e} - 5$). The dashed line in A–G shows the maximum ET fraction based on the energy or water limited condition. Subplot G is slightly different than (A) and (D) because all model runs have the same aridity, so the maximum value of $\langle PET \rangle / \langle P \rangle$ is a constant value.

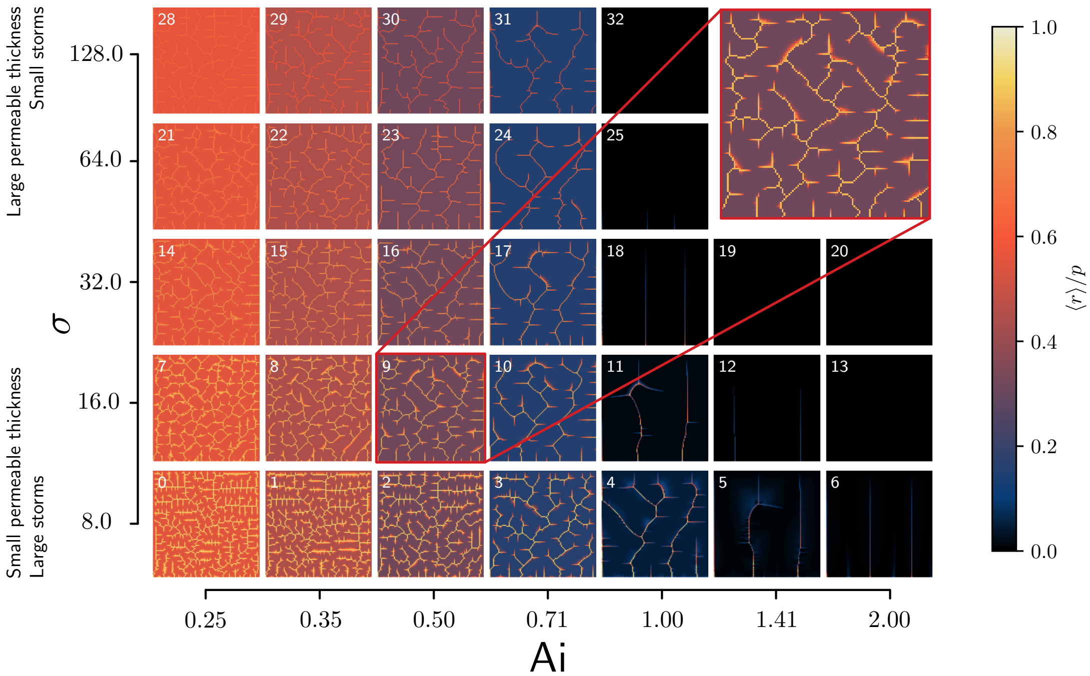

Figure 3. Average storm recharge rate $\langle r \rangle$ relative to the mean precipitation rate p for the same model runs that appear in Figure 1. Black areas indicate the absence of recharge. Hidden model runs (26, 27, 33, 34) did not produce any recharge. Results show expected decrease in recharge relative to precipitation with increasing aridity, although this effect is dampened when σ is small. The inset plot highlights that recharge is greatest in valley bottoms and convergent areas, revealing sensitivity to water table depth.

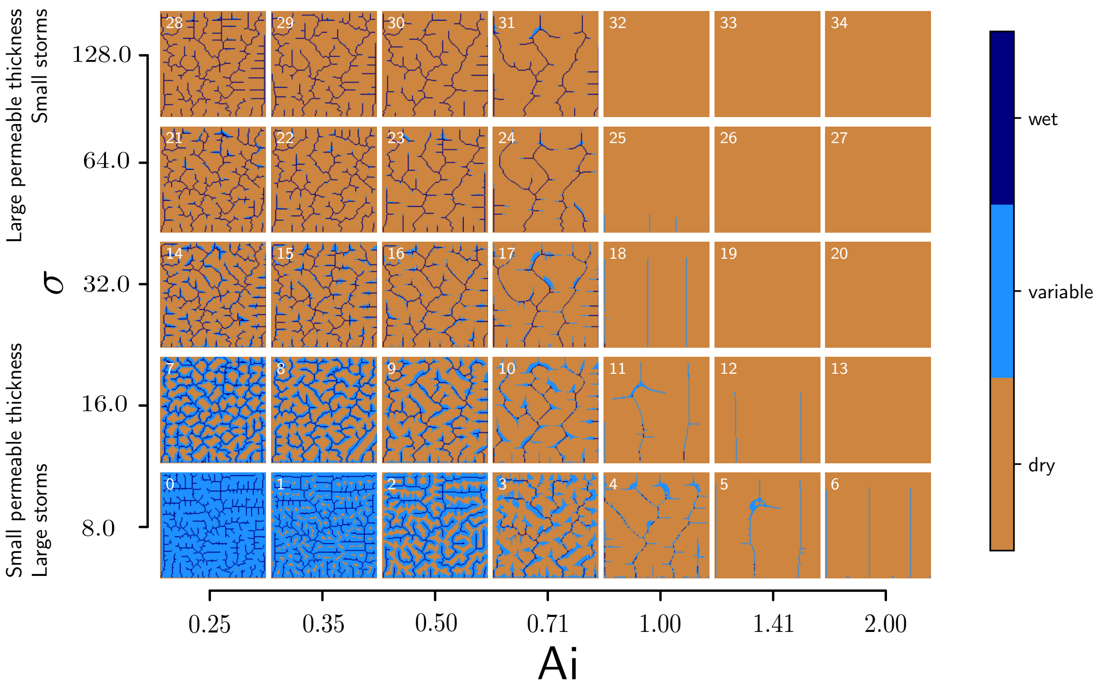

Figure 4. Classification of surface saturation for the same model set presented in Figure 1. Surface saturation is determined on the basis of time-variable water table proximity to the surface. Locations are classified as dry if they experience surface saturation at $<$ 5% of the ends of storms and interstorms, and are classified as wet if they are saturated at the end of $>$ 95% of storms and interstorms. Variably saturated areas are everywhere that does not meet either of these criteria. The results show the extent of variably saturated areas is greatest when σ is small. Non-permanent streams emerge in some cases as aridity increases, including cases like simulation 5, in which there are discontinuous zones of that are always wet.

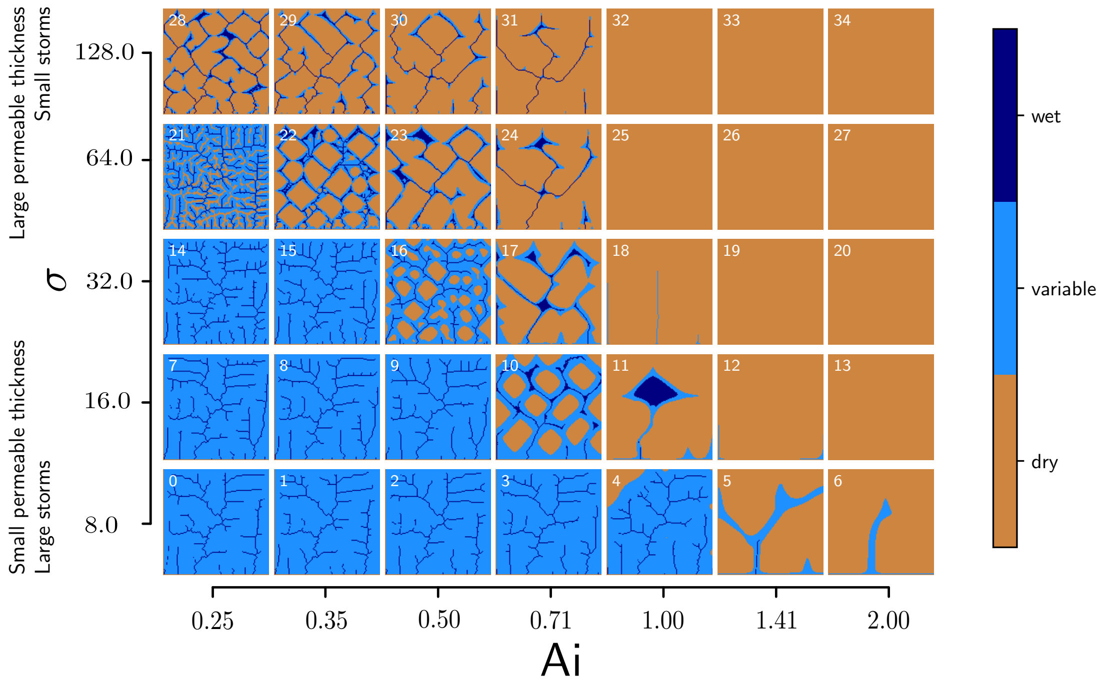

Figure 5. Classification of surface saturation for the model runs that appear in Supplemental Figure S5 and Figure 2(D–F), with $\beta = 0.05$. The classes are the same as in Figure 4. In contrast to the higher β case, here we see variably saturated areas from valleys to ridges in much of this parameter space. In the transition zone between widespread variable saturation and the zone without any channels, we see unusual channel forms, including nondendritic drainages (10, 16, 22, 23, 28), and extensive valley bottom wetland zones (11, 17, 23, 24, 28).

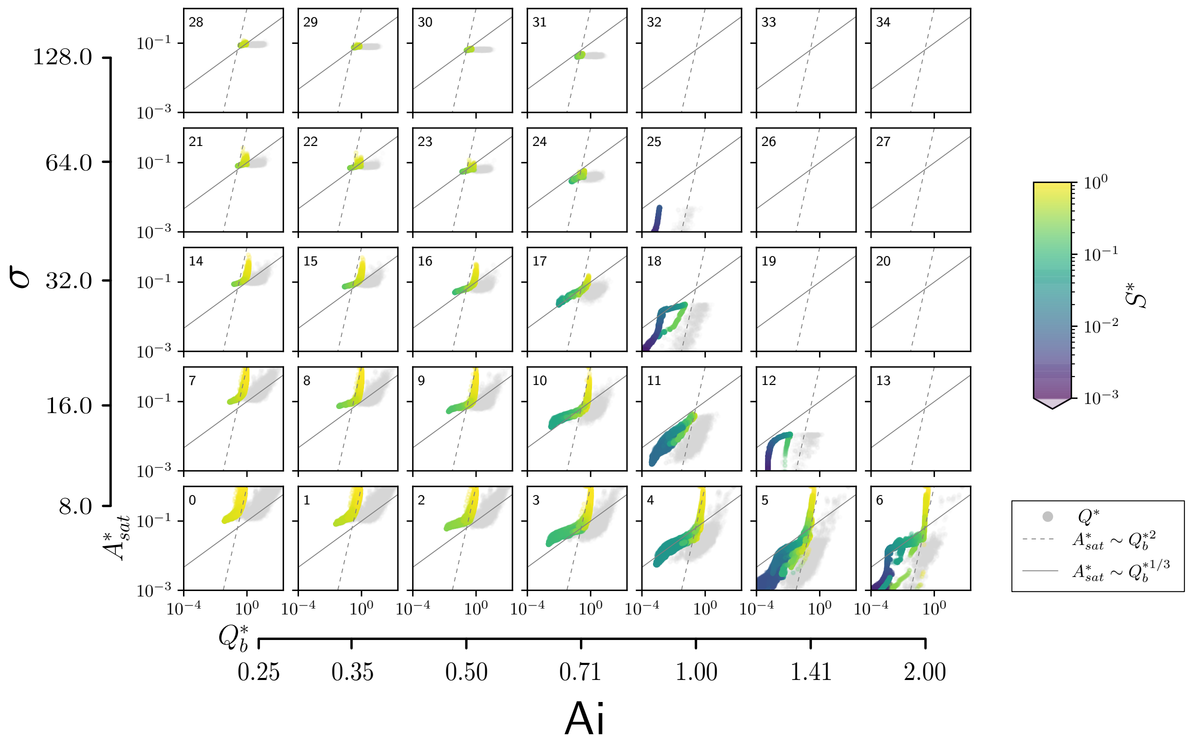

Figure 6. Dimensionless discharge Q^* and baseflow Q^*_b versus dimensionless saturated area A^*_{sat} for the same model runs that appear in Figure 1. A^*_{sat} is calculated using the same saturation criteria as all other figures, and has a maximum value of 1 when all cells are saturated. Each point depicts a model timestep, recorded at intervals corresponding to 1% of maximum timestep for groundwater model stability. Dimensionless discharge Q^* is depicted in gray. Dimensionless baseflow Q^*_b is colored by the dimensionless storage S^*, which varies from 1 when aquifer thickness is 0 everywhere to 1 when aquifer thickness is equal to permeable thickness everywhere. All quantities are totals of the model domain, and normalized by total area. We have left off subscripts for simplicity of notation. Dashed lines indicate the baseflow discharge equal to exfiltration at the mean recharge rate from the given saturated area. Data are absent for runs 19, 20, 26, 27, 33, and 34 because surface runoff was not produced.

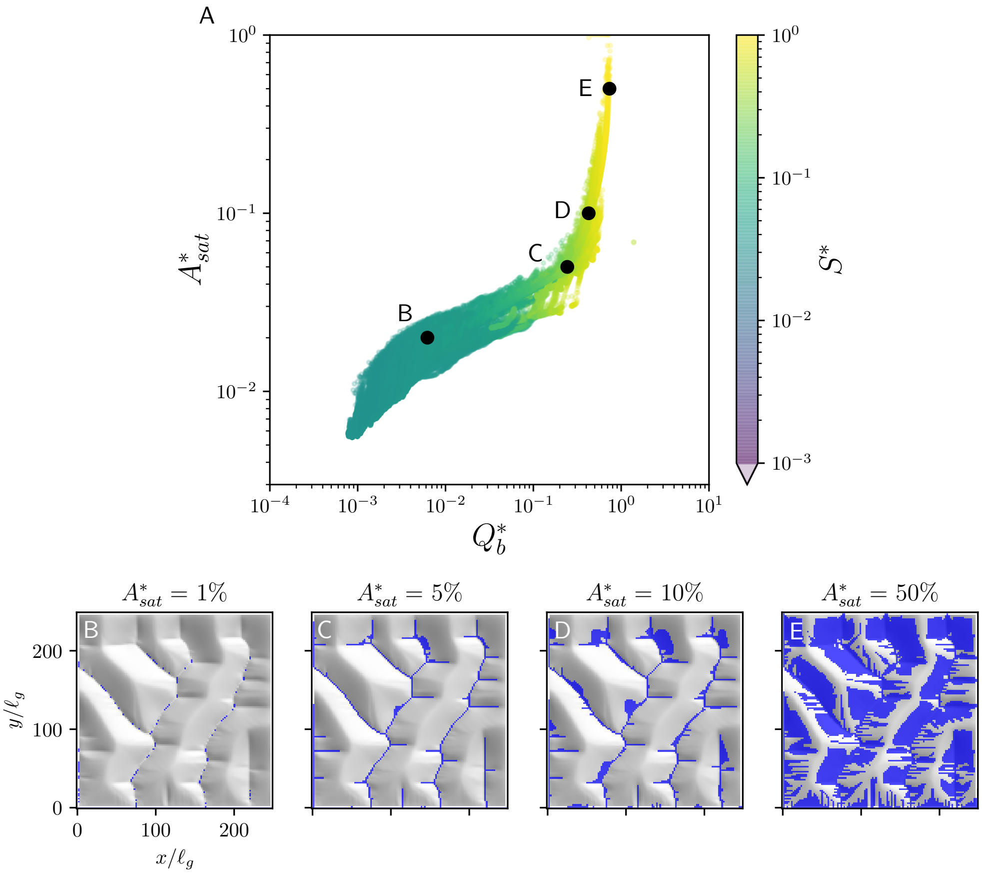

Figure 7. Detailed view of the dimensionless baseflow versus saturated area plot presented in Figure 6-4. Subplots (B–E) show the spatial distribution of saturation (in blue) at model timesteps corresponding to the locations (B–E) in panel (A). (B) shows saturation in second order channels. (C) sits right at the inflection point of the saturation-baseflow relationship, and corresponds to saturation just beginning to extend beyond the 1st order channel network. (D) shows more extensive saturation in unchanneled concave areas, while (E) shows widespread saturation on concave and planar slopes.

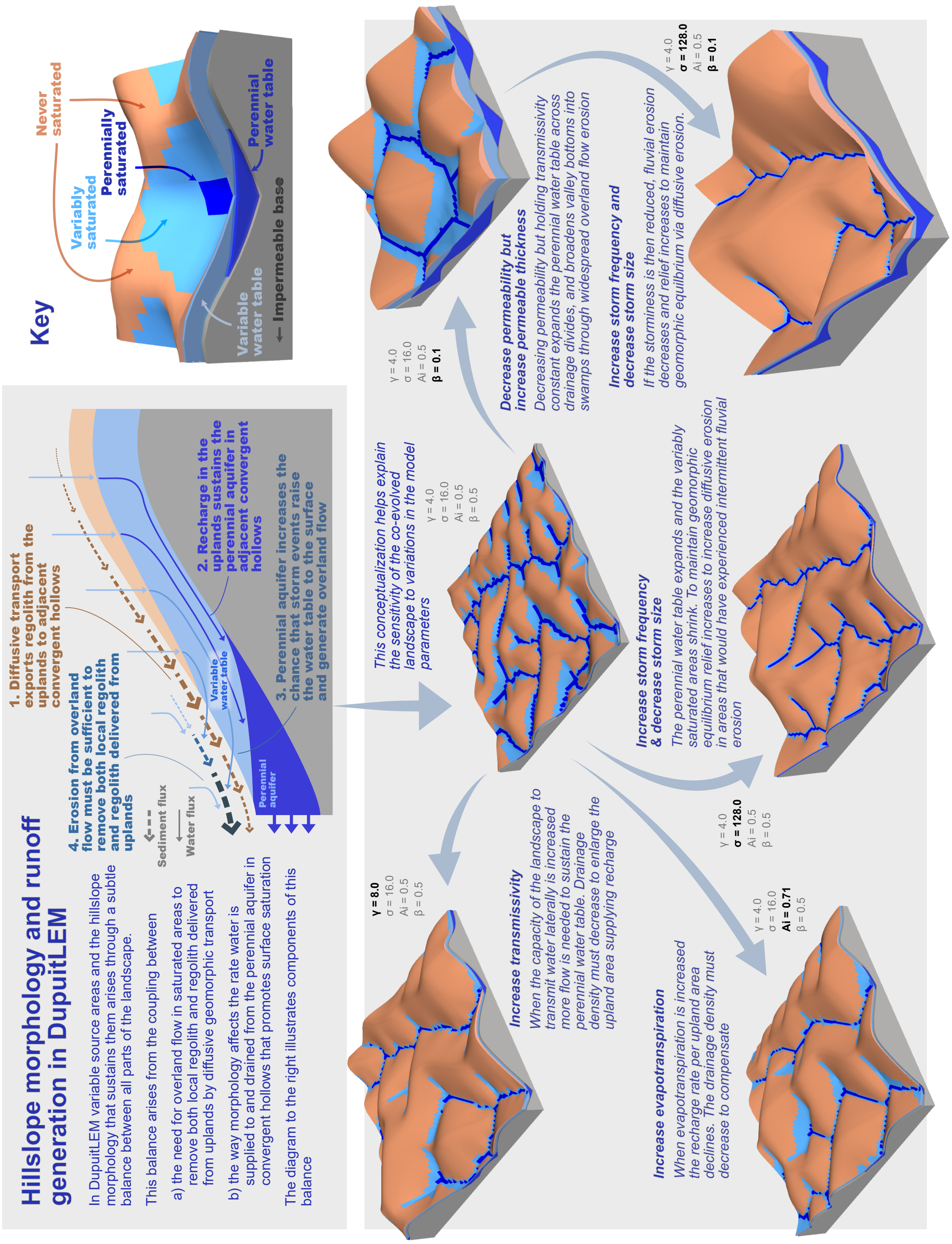

Figure 8. Conceptual figure illustrating how hillslope morphology and hydrology interact in DupuitLEM. This concept helps explain why varying the model parameters results in variations in drainage density and variable source area extent.

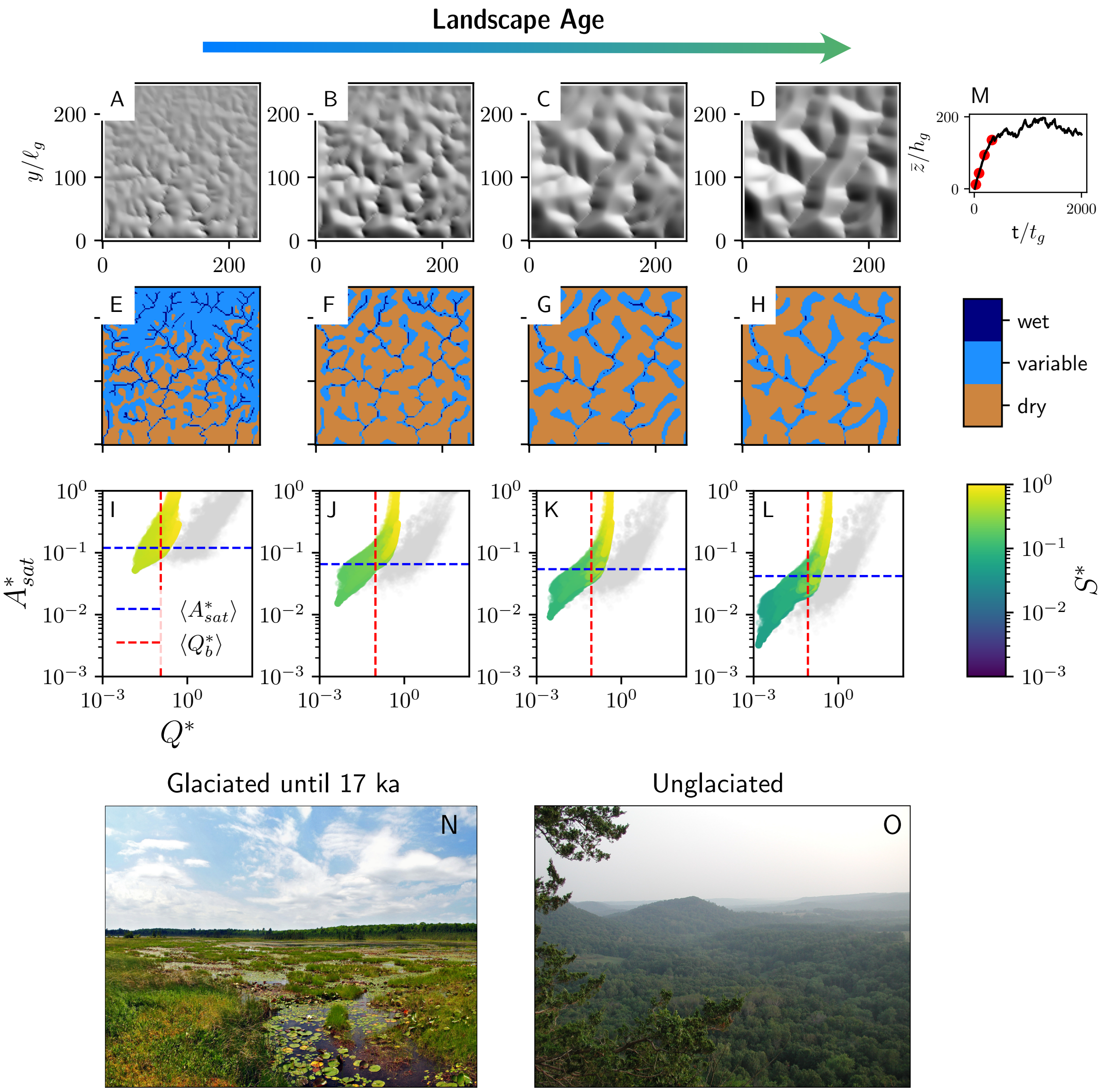

Figure 9. Comparison between results with increasing modelled age, as defined in the text above. (A–D) Hillshades of topography from a model run when mean elevation is 10, 30, 60, and 90% of the final value respectively (mean elevation is shown in (M)), showing decrease in dissection and steepening of slopes. (E–H) corresponding saturation classes showing transition from extensive wet drainage network and intermittently saturated zones to sparser drainage network with variably saturated channel adjacent zones. (I–L) corresponding dimensionless saturation baseflow plots, showing decrease in mean baseflow and mean saturated area, especially associated with decrease in frequency of the highest flows and highest saturated areas, and decreases in the lowest flows and saturated areas. (N) Recently glaciated Grandma Lake Wetlands in northern Wisconsin, USA, showing low relief and widespread saturation. CC-BY-SA Aarongunnar via WikiMedia Commons. (O) Unglaciated site in the Driftless Area of Wisconsin at Wildcat Mountain State Park showing forest cover and greater relief. CC-BY-SA Dandog77 via WikiMedia Commons

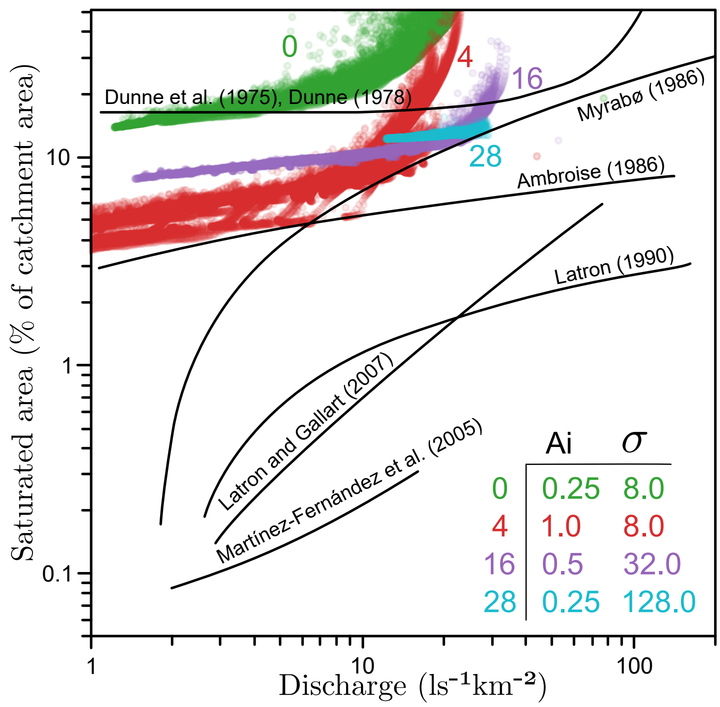

Figure 10. The relationship between saturated area and baseflow discharge for a several well-studied sites, reproduced from Latron and Gallart (2007), along with several of our model runs, 0, 4, 16, and 28, from Figure 6, which have been re-dimensionalized for the sake of obtaining baseflow discharge in the appropriate units. Parameters that vary are listed in the inset table. Our results are clipped to the extent originally presented in Latron and Gallart (2007).

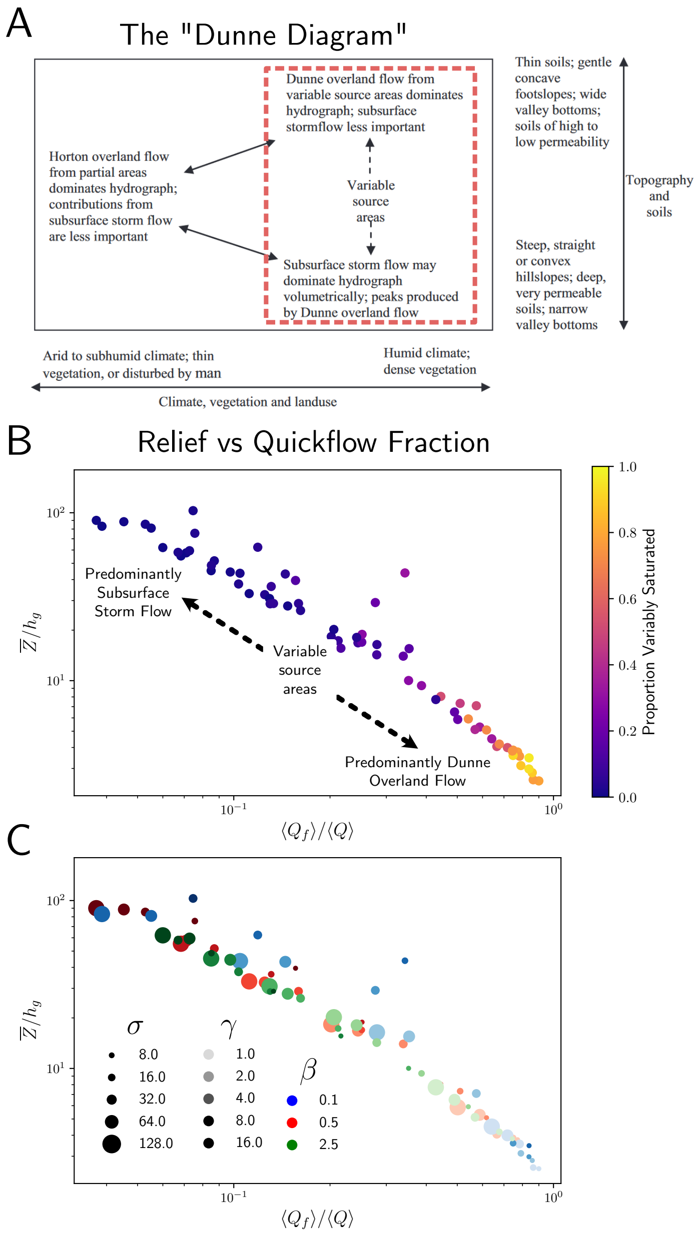

Figure 11. (A) The Dunne Diagram, reproduced from Li et al. (2014), highlighting the humid environments (red dashed box). (B) The relationship between the quickflow fraction and the mean relief, normalized by the characteristic height scale h_g for three sets of parameters, varying σ, γ, and β. All model runs are for humid climates (Ai $=$ 0.5). Other parameters are the same as those used previously ($\rho = 0.03$, $\phi = 1.5$, $\alpha = 0.15$, $\lambda = 250$, $S_c = 0.5$, δ varies from $1e-4$ to $4e-6$ with β). Colors indicate the fraction of the landscape classified as variably saturated under the definition used in previous sections. (C) The same plot as (B), but colored to show the particular combination of the three parameters varied. Dot size scales with σ, color lightness with γ, and base color with β.

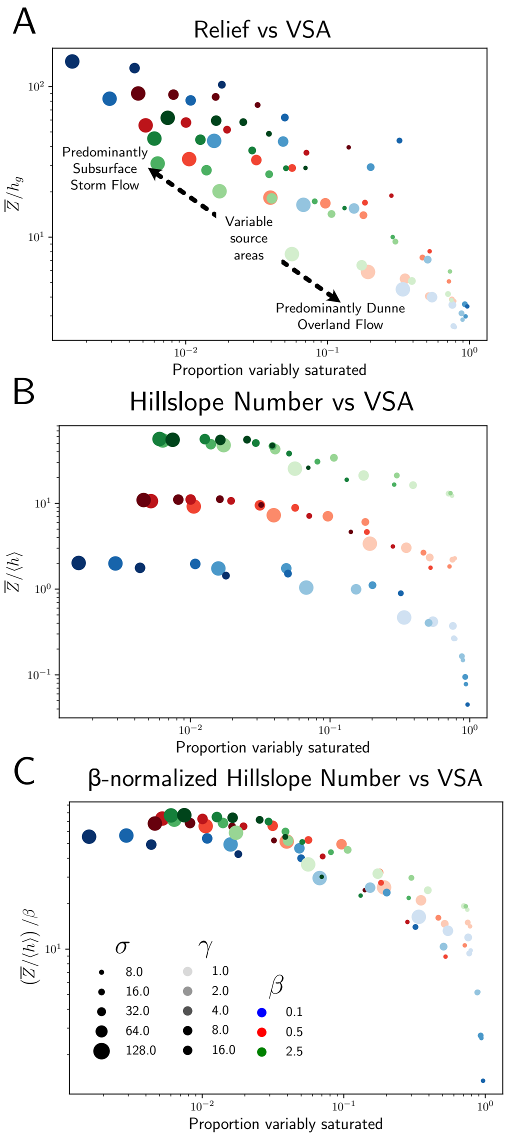

Figure 12. (A) variation in dimensionless relief $\overline{Z}/h_g$ versus the variably saturated area (VSA) as a fraction of the total area based on the definition introduced in Section 5.3 using the same model runs shown in Figure 11, showing substantially more scatter than Figure 11A. (B) The hillslope number $\overline{Z}/\langle h \rangle$ plotted against the proportion variably saturated, showing parallel but distinct relationships for each value of β. (C) Normalizing the vertical axis in (B) by β collapses all the relationships, and shows that the β-normalized hillslope number is maximized when the fraction of the watershed that is variably saturated is small, and minimized when the variably saturated fraction is large.

Supporting Information for "Evolving Hydrological Landscapes"

David G. Litwin[1], Gregory E. Tucker[2,3], Katherine R. Barnhart[4], Ciaran J. Harman[1,5]

[1]Department of Environmental Health and Engineering, Johns Hopkins University, Baltimore, MD, USA

[2]Cooperative Institute for Research in Environmental Sciences (CIRES), University of Colorado, Boulder, CO, USA

[3]Department of Geological Sciences, University of Colorado, Boulder, CO, USA

[4]U.S. Geological Survey, Geologic Hazards Science Center, Golden, CO, USA

[5]Department of Earth and Planetary Science, Johns Hopkins University, Baltimore, MD, USA

Contents of this file

1. Figures S1 to S12

Additional Supporting Information (Files uploaded separately)

1. Caption for large Table S1

Introduction The supplemental material here consists of figures that complement those presented in the main text and a table that lists parameters for the model runs used throughout the manuscript. Figure S1 shows the change in relief with time for all model runs. Figure S3 shows a sample timeseries with the baseflow separation applied, while Figure S4 shows the sensitivity of classified saturated areas to the thresholds used for each

Corresponding author: C. J. Harman, Department of Environmental Health and Engineering, Johns Hopkins University, Baltimore, MD USA. (charman1@jhu.edu)

class. Figures S5-S11 show equivalent figures to many of those presented in the text for varying aridity index Ai and water storage index σ when aquifer relief scale β is small, and for varying drainage capacity γ and σ. Figure S12 shows the detailed mapping between saturated area and baseflow discharge corresponding to the results in Figure 6, simulation 14.

Table S1. Full model parameters used to generate model output. This table and descriptions of all parameters in the table are also in the model output archive (https://doi.org/10.5281/zenodo.7621354)

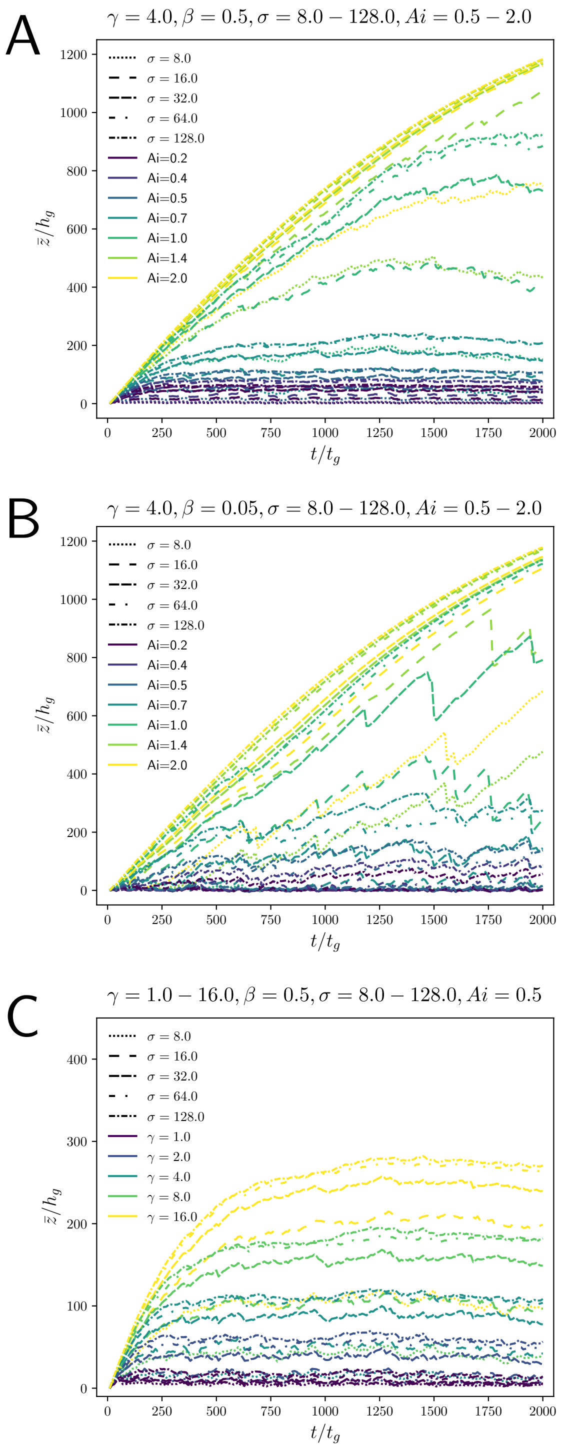

Figure S1. (Caption next page.)

Figure S1. Change in mean elevation with time for model runs in Figures 1, S5, and S6 in subplots A, B, and C respectively. (A) and (B) show that cases with the highest aridity and σ still have increasing mean elevation at the end of the simulation, while low aridity cases no longer have increasing relief at this point. (B) shows that when β is small, abrupt changes in mean elevation are still possible even well into simulations. This reflects the ongoing reorganization that these simulations undergo. (C) shows that humid cases with large β and a range of σ and γ reach dynamic equilibrium over the course of the simulations we conduct.

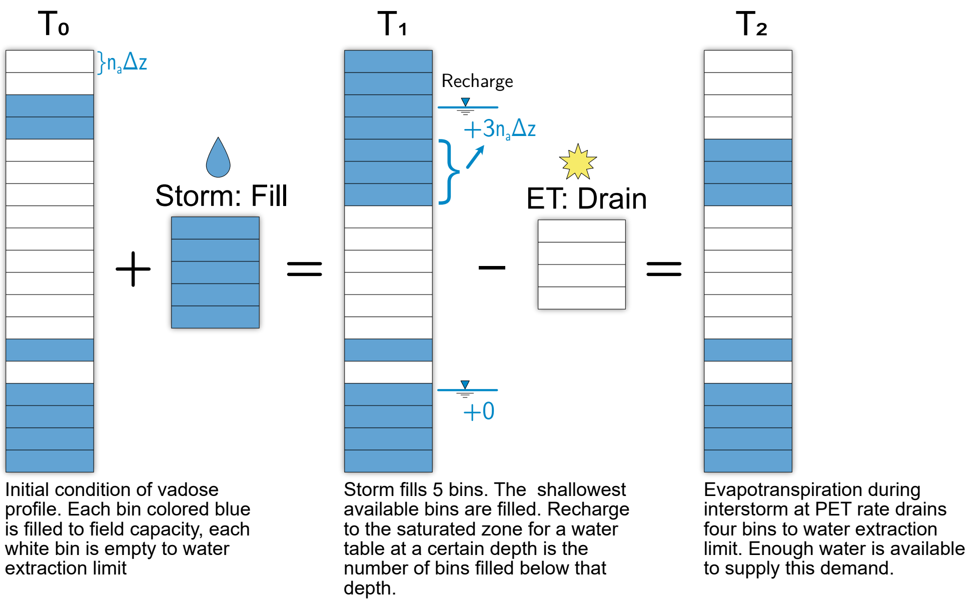

Figure S2. Sample calculations of vadose state and recharge using the Schenk model. The profile is divided into discrete bins that have storage capacity $\Delta z n_a$. Here we show three timesteps representing a storm-interstorm pair where neither water storage nor evapotranspiration are limited by available storage in the profile.

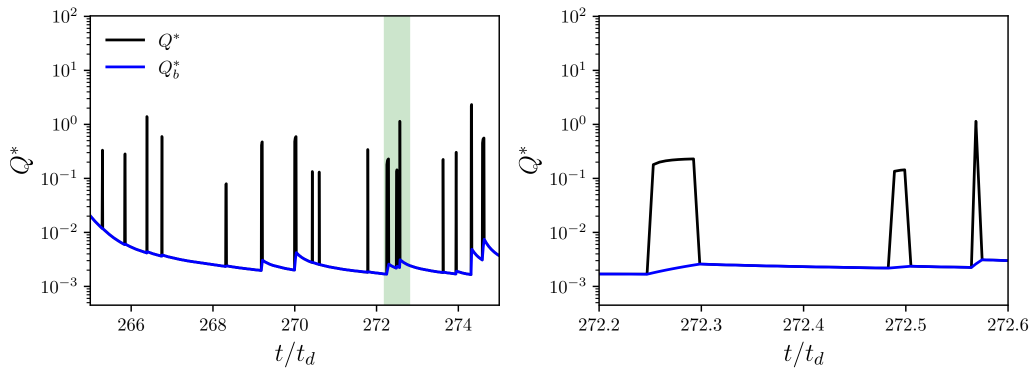

Figure S3. Sample of timeseries and baseflow separation. Baseflow during storm events changes linearly from pre-event to post-event discharge. Area highlighted in green is expanded in the right panel.

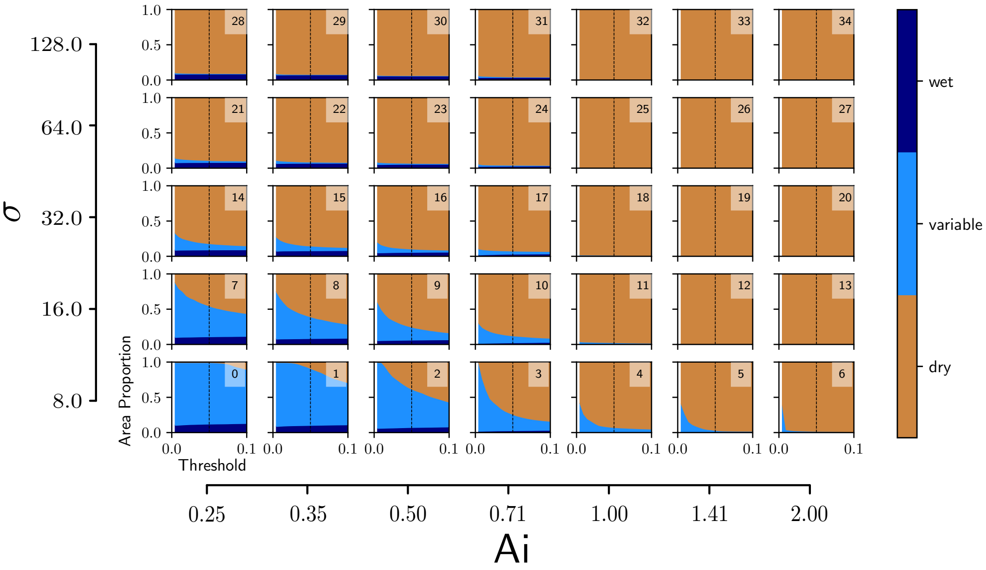

Figure S4. Subplots for the model runs in Figure 1, each showing the proportion of the domain assigned to each class (dry, variably saturated, and wet), as the threshold is varied. For example, at a threshold of 0.01, dry places are those that are saturated at the end of $< 1\%$ of storms and interstorms, while wet areas are those that are saturated at the end of $> 99\%$ of storms and interstorms. Dotted line shows the threshold used for the figures in the main text. Sensitivity to threshold is low for permanently saturated areas. Sensitivity of the variably saturated zone is highest for low values of σ.

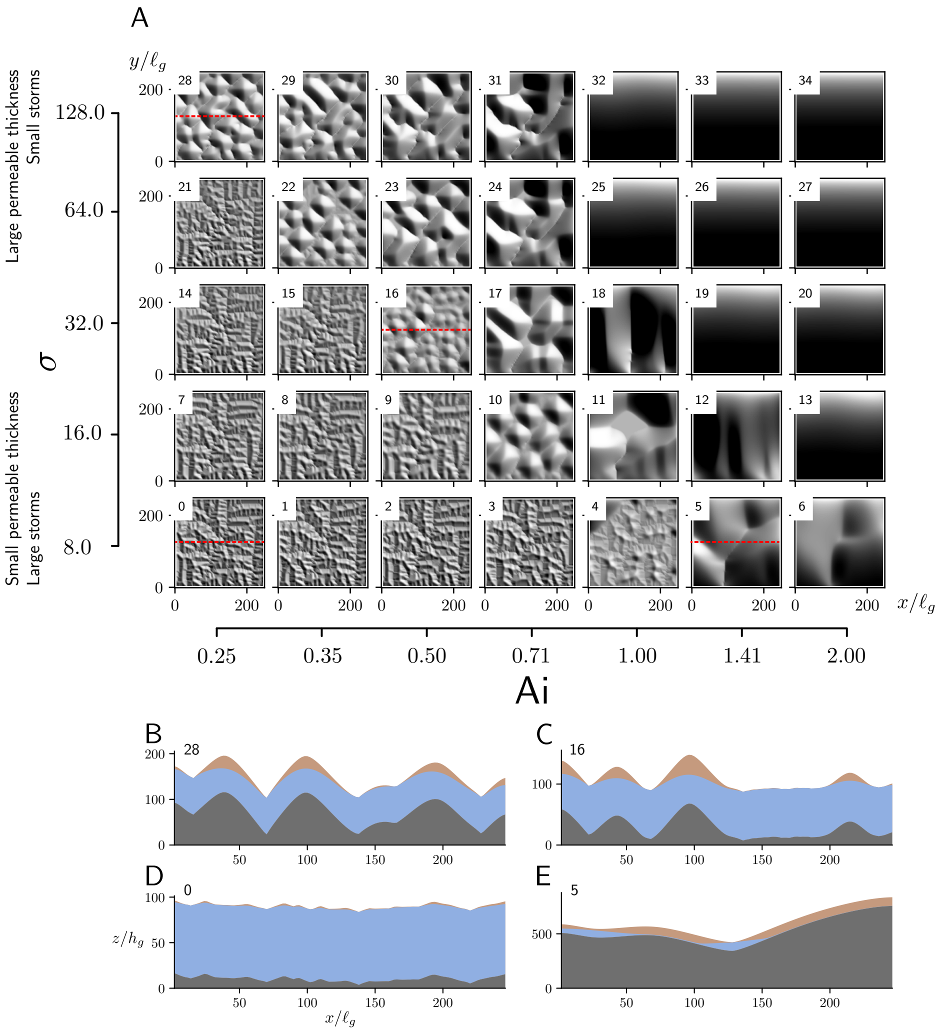

Figure S5. Hillshades (A) of modeled topography with varying aridity Ai and water storage index σ, for $\beta = 0.05$, an order of magnitude lower than those in Figure 1 in the main text). All models have been run for 2000 t_g timesteps. Here $\gamma = 4.0$, $\rho = 0.03$, $\phi = 1.5$, $\alpha = 0.15$, $S_c = 0.5$, $\lambda = 250$, and δ =2e − 4. Lower subplots (B–E) are lateral transects through topography for the corresponding numbered model runs located at the red dashed lines. Gray areas are impermeable bedrock, brown areas are regolith, which is shown behind the mean aquifer thickness in light blue. Note differences in the vertical scale in the cross section subplots.

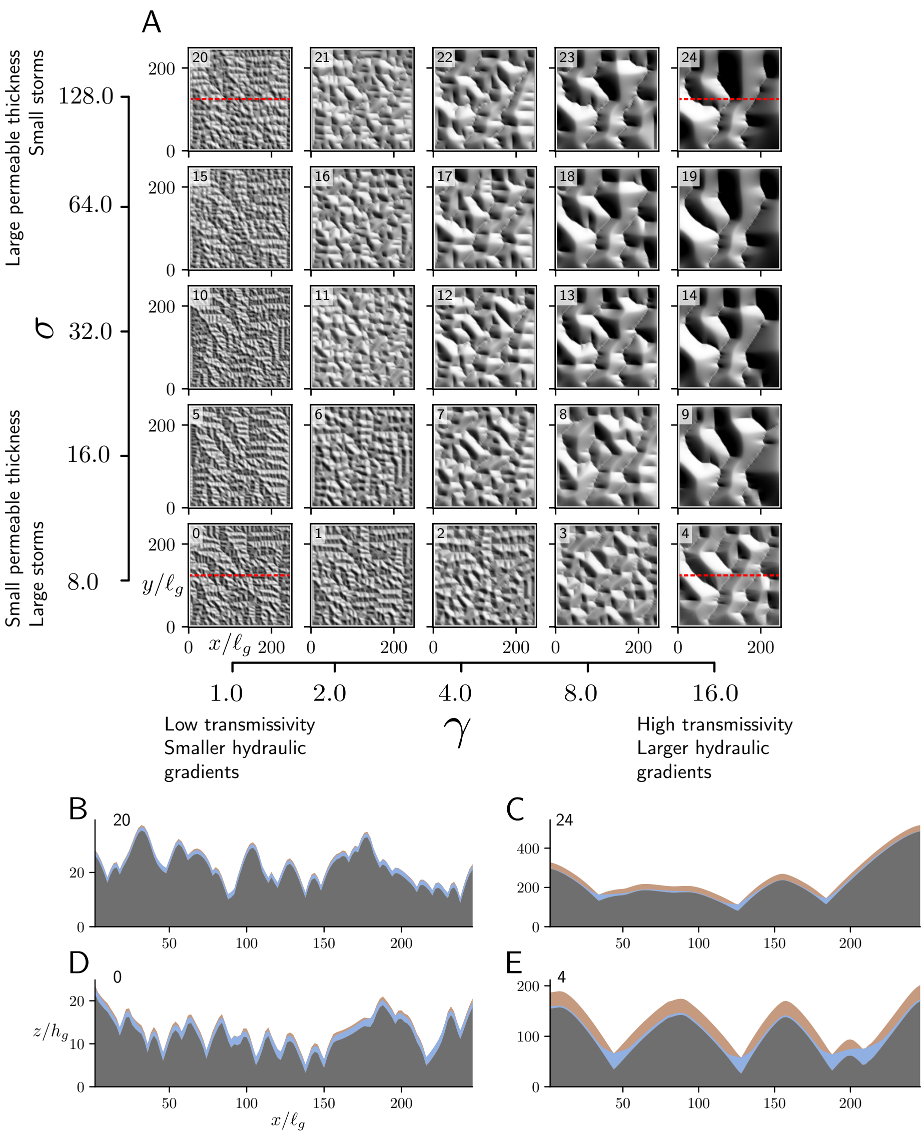

Figure S6. Hillshades of modeled topography with varying drainage capacity index γ and water storage index σ, showing decreased dissection with increasing drainage capacity. All models have been run for 2000 t_g timesteps. Here Ai = 0.5, $\beta = 0.5$, $\rho = 0.03$, $\phi = 1.5$, $\alpha = 0.15$, $S_c = 0.5$, $\lambda = 250$, and δ =2e $-$ 5. Lower subplots (B–E) are lateral transects through topography for the corresponding numbered model runs located at the red dashed lines. Gray areas are impermeable bedrock, and brown areas are regolith, which is shown behind the mean aquifer thickness in light blue. Note differences in the vertical scale in the cross section subplots.

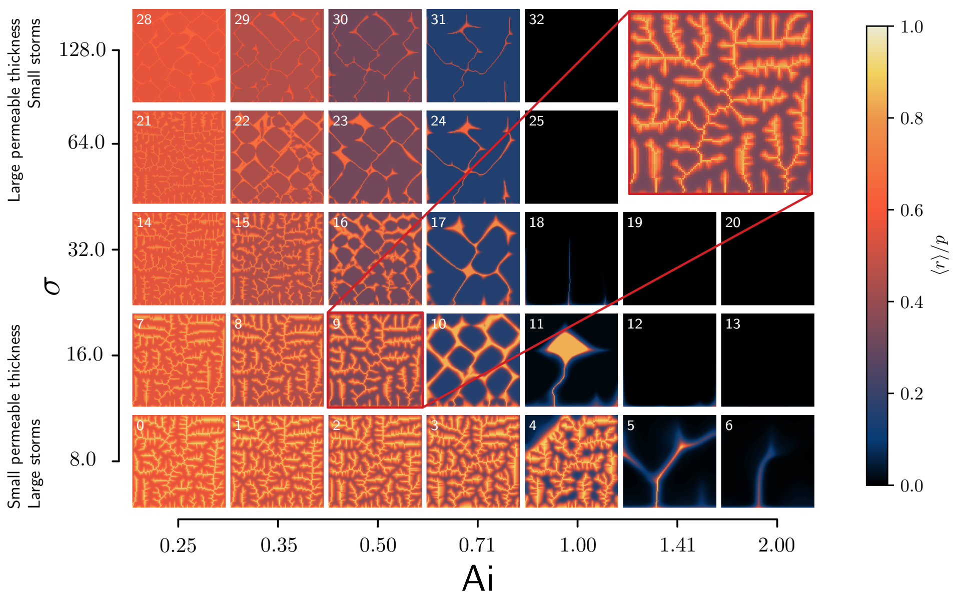

Figure S7. Average storm recharge rate $\langle r \rangle$ relative to the mean precipitation rate p for the same model runs that appear in Figure S5. Black areas indicate the absence of recharge. Hidden model runs (26, 27, 33, 34) did not produce any recharge. Results show expected decrease in recharge relative to precipitation with increasing aridity, and the complex quasi-nondentritic drainage patterns that emerge for certain combinations of Ai and σ. The inset plot highlights that recharge expands beyond one-pixel wide channels to include a wider valley bottom.

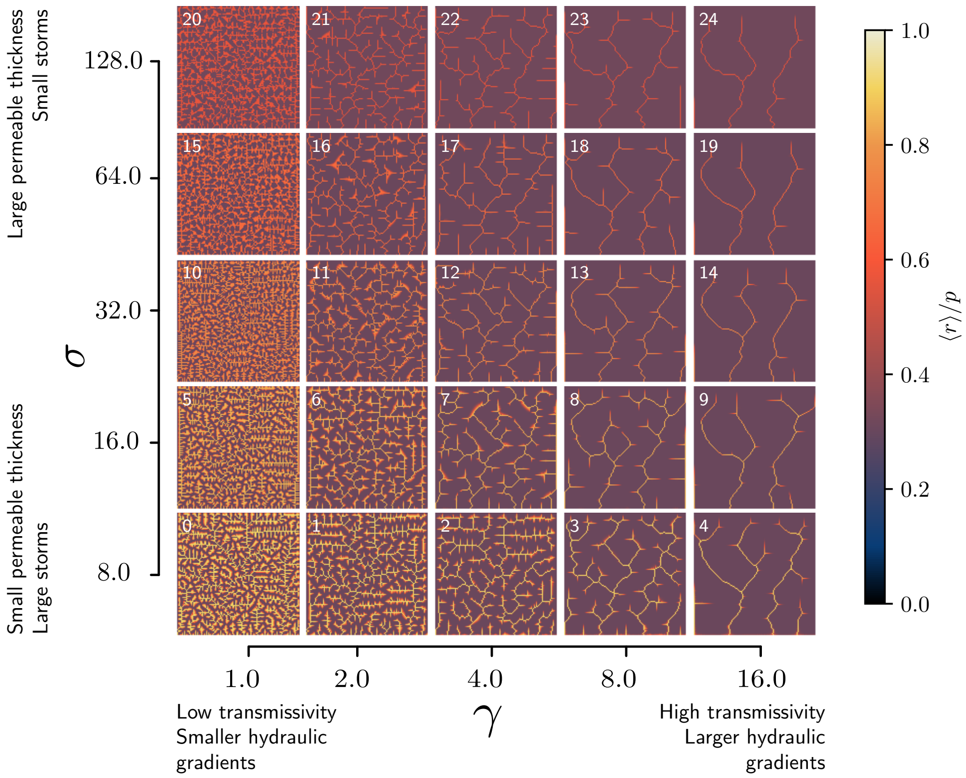

Figure S8. Average storm recharge rate $\langle r \rangle$ relative to the mean precipitation rate p for the same model runs that appear in Figure S6, varying drainage capacity index γ and water storage index σ. Results show that at constant aridity, the hillslope recharge rate is more or less invariant, but the σ and γ play important roles in controlling where recharge occurs. Recharge rates in valley bottoms decline with increasing σ.

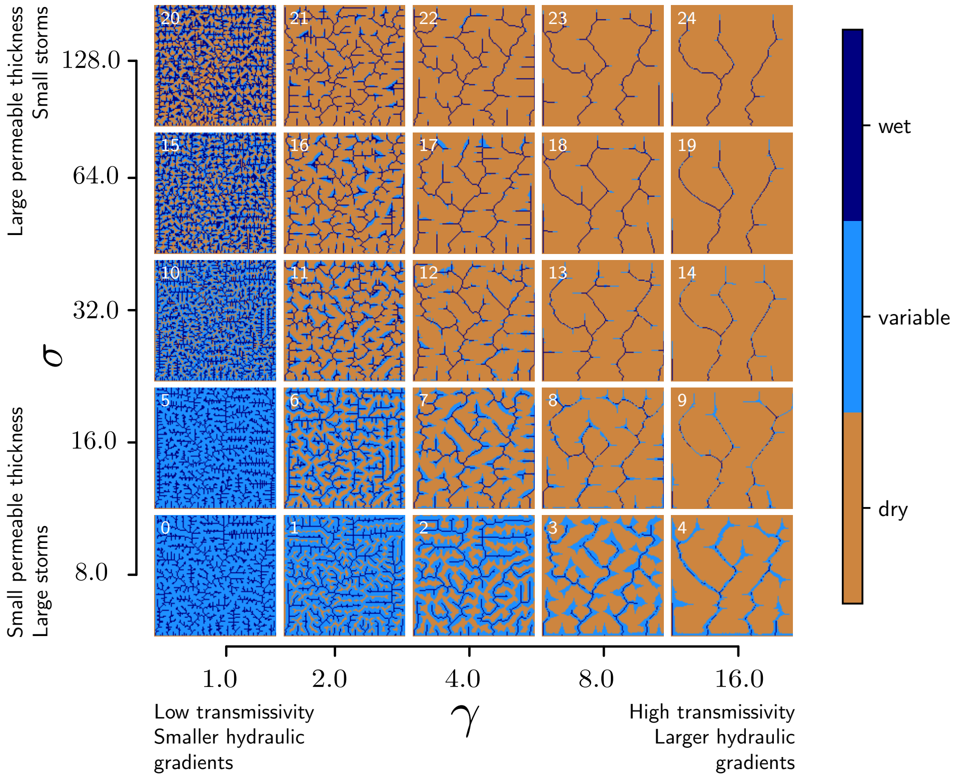

Figure S9. Classification of surface saturation for the same model runs that appear in Figure S6. Surface saturation is determined on the basis of water table proximity to the surface. Locations are classified as dry if they experience surface saturation at $< 5\%$ of the ends of storms and interstorms, and are classified as wet if they are saturated at the end of $> 95\%$ of storms and interstorms. Variably saturated areas are everywhere that does not meet either of these criteria. The results show the extent of variably saturated areas when σ and γ are small, and near-fixed saturated areas when σ and γ are large.

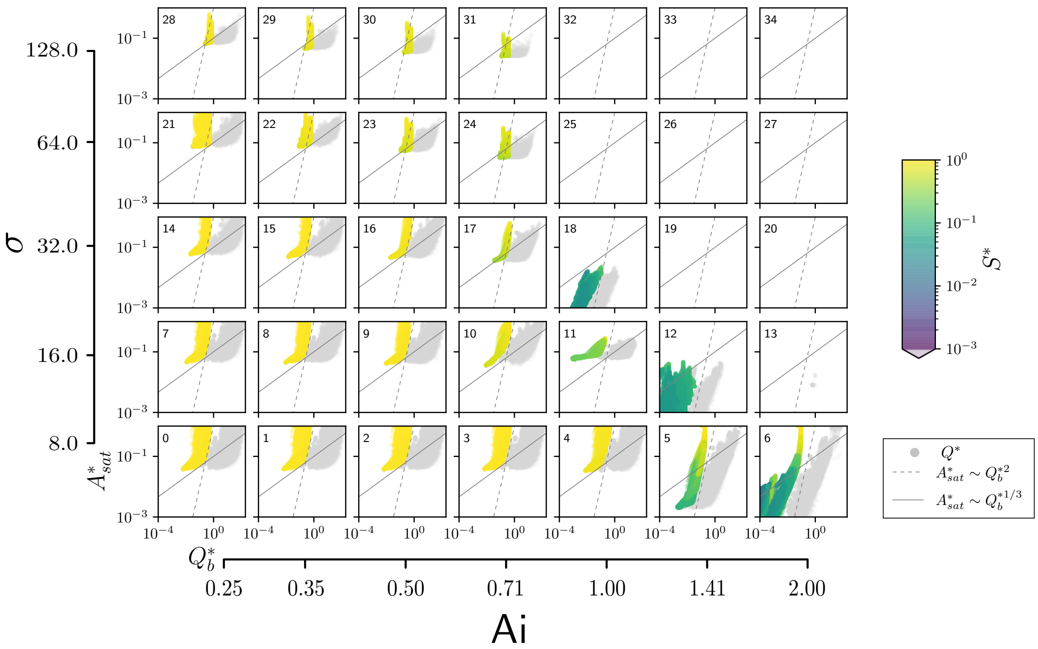

Figure S10. Dimensionless discharge Q^* versus dimensionless saturated area A^*_{sat} for the same model runs that appear in Figure S5 (varying σ and Ai, with low β). Dashed lines are provided for visual comparison with the modeled relationships. Results show less variability in baseflow than the high β equivalents. In cases where aridity is less than 1, the dimensionless storage remains high regardless of saturated area.

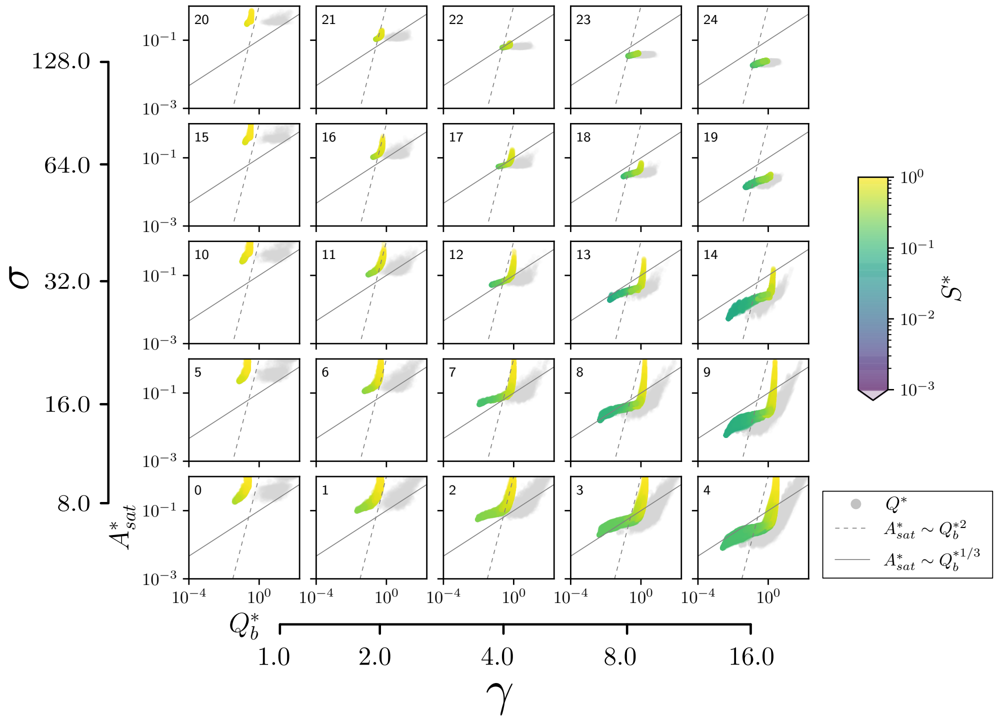

Figure S11. Dimensionless discharge Q^* versus dimensionless saturated area A^*_{sat} for the same model runs that appear in Figure S6. Increasing the drainage capacity γ is associated with declining saturated areas, and generally increasing (log) range in saturated area and discharge, and sharpening of the transition between the middle and upper ‘limbs’ of the sigmoid form. See for example the difference between (1) and (4), or between (11) and (14).

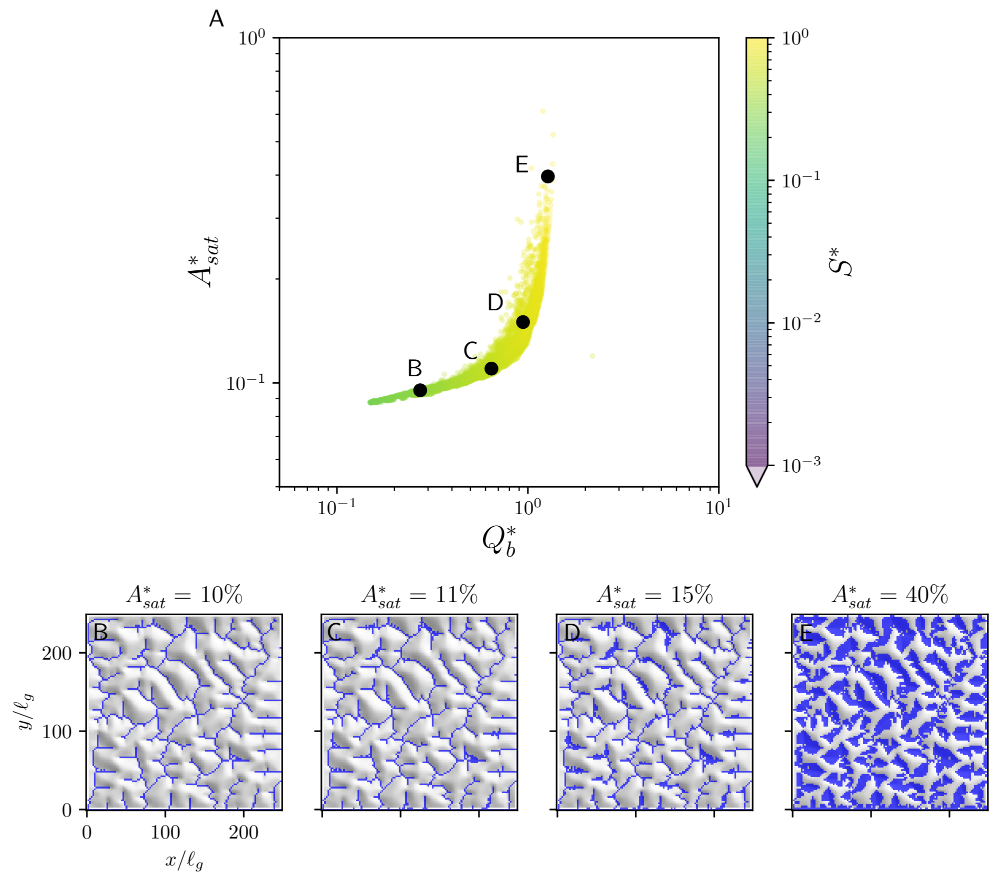

Figure S12. Detailed view of the dimensionless baseflow saturated area presented in Figure 6 simulation 14. Subplots (B–E) show the spatial distribution of saturation (in blue) at model timesteps corresponding to the locations (B–E) in panel (A). (B) shows saturation in first order channels. (C) sits just below the point where saturated area begins to increase rapidly with baseflow, and shows some saturation adjacent to channels and in channel heads. (D) shows more extensive saturation in unchanneled concave areas, while (E) shows widespread saturation on concave and planar slopes.